Universität Rostock Traditio et Innovatio

End Effects and Ground Linking of Wake Vortices of a Generic Landing Aircraft

Fakultät fü Maschinenbau und Schiffstechnik
an der Universität Rostock
zur
Erlangung des Grades eines Doktor-Ingenieurs (Dr.-Ing.)
eingereichte

D i s s e r t a t i o n

vorgelegt von

M.Sc. Gustavo Castaneda Fuentes

aus Tepic, Nay. Mexiko

https://doi.org/10.18453/rosdok_id00004665

Gutachter:

Prof. Dr.-Ing. habil. Sven Grundmann
Universität Rostock, Lehrstuhl Strömungsmechanik

Prof. Dr.-Ing. habil. Nikolai Kornev
Universität Rostock, Lehrstuhl für Modellierung und Simulation

Jahr der Einreichung: 2023

Jahr der Verteidigung: 2023

Hiermit versichere ich, die vorliegende Doktorarbeit unter der Betreuung von Prof. Dr.-Ing. habil. Sven Grundmann nur mit den angegebenen Hilfsmitteln selbständig angefertigt zu haben.

Rostock, den 17.07.2023

To my beloved Janine Mayer

Abstract

A potential danger for airplanes is the wake vortices produced by preceding aircraft, particularly in the terminal area of an airport where takeoffs and landings occur. The first part of this research work investigates experimentally in a towing tank the so-called end effects of wake vortices produced by a decelerating wing without ground interaction. The second part delves into the complex ground interaction when an aircraft's wing lands, particularly the phenomenon so-called ground-linking that happens when vortices connect with the ground after the wing comes to rest.

End-effects, the implications of the deceleration process on wake vortices, can be observed without ground interaction. The first part of the experimental investigation analyzes two vortex disturbances due to these end-effects and their impact on tangential and axial velocities in the wake vortices through Particle Image Velocimetry (PIV) measurements.

It is shown that the vortex core initially exhibits wake-like axial flow before transitioning to jet-like axial flow with the first disturbance, which increases in magnitude until the second disturbance with a helical-like topology occurs. The first disturbance is caused by a traveling pressure wave (vortex bursting) shortly after deceleration, while the second disturbance occurs shortly after the wing comes to rest. The disturbances affect the axial and tangential velocity profiles but do not trigger vortex breakdown or directly influence vortex decay. Nevertheless, these disturbances impair and degrade the vortices.

In the second part of the experimental investigation, a towed model is used to recreate a simplified landing trajectory that can adjust the angle of attack while decreasing the distance above the ground. Experimental evidence of ground-linking is provided by analyzing various measurement planes and discussing the three-dimensional vortex topology. The height above the ground where the wing comes to rest is systematically increased from one chord length to six chord lengths. The data analysis shows that the vortices take a longer time to link to the ground as the distance above the ground increases, and the vortices display different characteristics.

Lastly, an investigation of wake vortex ground-linking for low and high-speed approaches is carried out. The low-speed approach exhibits late vortex ground connection and low circulation values, whereas the high-speed approach shows an immediate connection to the ground and high circulation values. The vortices remain stationary in the low-speed approach and drift considerably in the fast approach.

These findings highlight the importance of understanding the vortex system's characteristics, which depend on the approach speed and terminal height above ground. Unique patterns emerge in each situation, and comprehending these patterns is critical to ensure airport safety and create effective strategies to reduce aircraft spacing.

Zusammenfassung

Eine potenzielle Gefahr für Flugzeuge sind Wirbelschleppen, die von vorausfliegenden Flugzeugen erzeugt werden, insbesondere im Terminalbereich eines Flughafens, wo Starts und Landungen stattfinden. Der erste Teil dieser Forschungsarbeit untersucht experimentell in einem Schleppkanal die sogenannten Endeffekte (end-effects) von Wirbelschleppen, die durch einen abbremsenden Flügel ohne Bodeninteraktion erzeugt werden. Der zweite Teil befasst sich mit der komplexen Bodeninteraktion bei der Landung eines Flugzeugflügels, vorwiegend mit dem sogenannten Phänomen "Ground-linking", das auftritt, wenn sich Wirbel mit dem Boden verbinden, nachdem der Flügel zur Ruhe gekommen ist.

Endeffekte, also die Auswirkungen des Verzögerungsprozesses auf Wirbelschleppen, können ohne Bodeninteraktion beobachtet werden. Im ersten Teil der experimentellen Untersuchung werden zwei durch diese Endeffekte verursachten Wirbelstörungen und deren Einfluss auf die Tangential- und Axialgeschwindigkeiten in den Wirbelschleppen mittels Particle Image Velocimetry (PIV) Messungen analysiert.

Es wird gezeigt, dass der Wirbelkern zunächst eine nachlaufartige axiale Strömung aufweist, bevor er mit der ersten Störung in eine strahlartige axiale Strömung übergeht, deren Stärke zunimmt, bis die zweite Störung mit einer helikalen Topologie auftritt. Die erste Störung wird durch eine wandernde Druckwelle (bursting) kurz nach dem Abbremsen verursacht, während die zweite Störung kurz nach dem Stillstand des Flügels auftritt. Die Störungen wirken sich auf die axialen und tangentialen Geschwindigkeitsprofile aus, lösen jedoch keinen Wirbelzusammenbruch (break down) aus und haben auch keinen direkten Einfluss auf den Wirbelzerfall. Dennoch beeinträchtigen und schwächen diese Störungen die Wirbel.

Im zweiten Teil der experimentellen Untersuchung wird ein Schleppmodell verwendet, um eine vereinfachte Landebahn nachzubilden, die den Anstellwinkel anpassen und gleichzeitig den Abstand über dem Boden verringern kann. Der experimentelle Nachweis der Bodenanbindung (ground-linking) erfolgt durch die Analyse verschiedener Messebenen und die Diskussion der dreidimensionalen Wirbeltopologie.

Die Höhe über dem Boden, in der der Flügel anhält, wird systematisch von einer Sehnenlänge auf sechs Sehnenlängen erhöht. Die Datenanalyse zeigt, dass die Verbindung der Wirbel mit dem Boden mit zunehmender Entfernung über dem Boden länger dauert und die Wirbel unterschiedliche Eigenschaften aufweisen. Abschließend wird eine Untersuchung der Wirbelschleppen-Bodenkopplung für Anflüge mit niedriger und hoher Geschwindigkeit durchgeführt. Der Ansatz mit niedriger Geschwindigkeit zeigt eine späte Wirbel-Bodenverbindung und niedrige Zirkulationswerte, wohingegen der Ansatz mit hoher Geschwindigkeit eine unmittelbare Verbindung zum Boden und hohe Zirkulationswerte zeigt. Die Wirbel bleiben beim langsamen Anflug stationär und driften beim schnellen Anflug erheblich ab.

Diese Ergebnisse unterstreichen, wie wichtig es ist, die Eigenschaften des Wirbelsystems zu verstehen, die von der Annäherungsgeschwindigkeit und der Endhöhe über dem Boden abhängen. In jeder Situation treten einzigartige Muster auf, und das Verständnis dieser Muster ist von entscheidender Bedeutung, um die Flughafensicherheit zu gewährleisten und wirksame Strategien zur Reduzierung der Flugzeugabstände zu entwickeln.

Contents

1 Introduction

1.1 Motivation

The terminal area of a takeoff and landing runway is the bottleneck that limits airport capacity increase. Therefore, the need for a reduction in the spacing between a leading aircraft and the following demands an accurate and highly reliable prediction of the leading aircraft's wake vortex behavior and decay. Wake vortices are an inherent consequence of lift production. Hence vortices strength scales with the weight of an aircraft. When the aircraft lands, the strong vortices detach from the wingtips and linger at the terminal area. These remaining vortices pose a severe threat to the following landing aircraft due to the strongly induced rolling moments and the limited height above ground for the pilot to react and stabilize the aircraft. Therefore, towing tank experiments are conducted to understand the vortices' behavior. Towing tank facilities are beneficial because the test area is long enough to recreate a scaled wake vortex. Additionally, towing tanks are further suited for vortex ground interaction experiments because of the lack of relative movement of the fluid (water) and the ground. Here is where the motivation of the present thesis lies, i.e., recreate a representative wake vortex in a towing tank facility and provide insight into two cases. The first case is devoted to end-effects, and the second to ground linking.

1.2 State of the art Research

1.2.1 Wake vortices in ground proximity

Out of ground effect, the behavior of wake vortices from roll-up until decay is well understood. The shed vorticity roll-up's specific characteristics that lead to the formation of concentrated vortices are dictated by the aircraft and especially the wing-induced flow field [1]. The subsequent behavior of the rolled-up wake vortices, in terms of motion and decay, is dominantly influenced by atmospheric characteristics such as crosswind, turbulence, and the development of Crow instabilities [2].

Additionally, a certain degree of nonlinear behavior makes the wake vortex evolution sensitive to slight variations introduced by the generating aircraft or the atmosphere in an unpredicted manner resulting in minor deviations that make each vortex system unique [3]. Relatively well understood is the interaction of concentrated and longitudinal uniform wake vortices with the ground. According to Robins et al. [4], this interaction can be categorized into three regions characterized by the dominance of either inviscid or viscous phenomena. These are the previously mentioned out-of-ground effect (OGE) for $h_{AG} > 3 \cdot b$ (with height above ground labeled h_{AG} and the wingspan as b), the near-ground effect (NGE) from $b < h_{AG} < 3 \cdot b$, and the in-ground effect (IGE) from $h_{AG} < b$ region. In the NGE region, the primary vortices' sink rate decreases due to inviscid interaction with the ground and is commonly modeled by introducing image vortices. In the IGE region, there is strong viscous interaction with the ground; the primary vortices induce a vorticity layer that ultimately detaches as secondary vortices. Such interaction decouples the primary vortices from their image and hinders the progression of their lateral inviscid trajectory [5].

First fundamental research in the two-dimensional characteristics of the vortex ground interaction was carried out in the past. Lamb [6] found analytically for inviscid point vortices approaching a slip boundary that they move following a hyperbolic trajectory. A constant distance to the ground of half the initial vortex spacing is maintained in their parallel movement to the ground. Harvey and Perry [7] accomplished the first investigation considering viscosity in the vortex ground interaction in a wind tunnel with a moving ground. Additionally, they performed field measurements. They recognize the characteristic formation of a vorticity layer at the ground and the adverse pressure gradient that leads to secondary vortex detachment. They also found that the primary and secondary vortices have mutual interaction resulting in an upward-directed motion known as vortex rebound, ensuing in primary vortices' deviation from their inviscid hyperbolic trajectories.

Investigation of the three-dimensional characteristics of wake vortices and ground interaction is predominantly carried out numerically and evolves alongside computing performance. Two methods are present: direct numerical simulation (DNS) and large eddy simulation (LES), and both are limited to low Reynolds numbers to fulfill resolution requirements. On this behalf, a distinction can be made between the study of longitudinaly uniform vortices, termed time developing, and nonuniform vortices, termed space developing.

However, the numerical complexity and computational cost of space development approaches are high, and the methods are in an early development stage; therefore, investigations of this kind are limited [8]. Several time-developing LES studies were carried out in the past, focusing on the vortex sensitivity to selected atmospheric conditions such as crosswind and turbulence. One of these studies was carried out by Hamilton and Proctor [9]. They conducted time-developing LES simulations focusing on wake vortex transport and ground interaction for a range of initial vortex strengths and spacings representative of small, medium, and large aircraft along crosswind and shear gradients. They found that lateral transport for vortices IGE is shown to be more pronounced in high crosswind situations than it is compared to the OGE case and is more severe on the downwind vortex. Simultaneously, high crosswind shear gradient reduces the vortex descent rates, and both situations seem independent of the aircraft type. In a different LES study, Proctor et al. [10] found that a small amount of turbulence is needed to enhance the decay for vortices IGE. Nevertheless, the decay rates are insensitive to the magnitude of turbulence. Vertical oscillations are damped due to the weakening of secondary vortices by enhanced dissipation due to ambient turbulence. Field measurements partially corroborate these findings [11].

Puel et al. [12] described rebound as one stage of interaction between the primary and secondary vortex. Specifically, when the secondary vortex detaches from the ground (separated boundary layer), the opposite sign vorticity increases rapidly, moving up the primary vortex. Furthermore, Holzäpfel and Steen [11] show that crosswind has a significant impact on the vortex rebound characteristics. At the upwind vortex location, the formation of the induced secondary vortex at the ground is hindered, whereas it is enhanced at the downwind vortex location. This uneven interplay leads to vortex tilting, asymmetric decay, and rebound due to unequal vortex strength interaction. Additionally, they show that the rapid decay phase for vortices IGE is longer than OGE and suggest it as a possible reason for the less severe interaction between primary and secondary vortices at the ground compared to the only primary vortex interaction due to Crow instability. The most critical crosswind velocity magnitude was close to the initial vortex descend speed based on Lidar measurements, numerical investigations, and vortex encounter records [3].

Experimental investigations in research facilities focusing on vortex-ground interaction are few. They mainly aim to describe the vortex behavior in the ground proximity generated by a model at a constant speed and distance to the ground. These experiments are carried out in towing tanks for either complete aircraft configurations or isolated generic wings. Towing tanks enable long-range wake flow measurements and are particularly suited for ground interaction investigations [13]. For complete configurations, Ciffone and Pedley [14] investigated scaled long-range aircraft at a representative distance to the ground and the derived vortex interaction. They found changes in the inviscid vortex trajectory due to the viscous effects. However, no significant modifications were found in the overall merging and interaction of the vortices shed by the wingtip and high-lift devices. Furthermore, they found changes in the tangential vertical velocity profiles at the nearby region of the primary and secondary vortex interaction but without a change in the magnitude of the maximum tangential velocities.

For only wing configurations, Konrath et al. [15] conducted towing tank experiments focusing on the vortex ground interaction for chord based Reynolds number $Re_c = 74.25 \cdot 10^3$ and heights above ground of $h_{AG} = 0.5 \cdot b$, $0.25 \cdot b$, and $0.125 \cdot b$. They observed the development of a vorticity layer at the ground but without forming a secondary vortex. Furthermore, they observed an increase in the lateral vortex velocity, a decrease in the vertical velocity, and an increased tendency to maintain distance to the ground when they reduced the height above the ground. Cottin et al. [16] carried out a qualitative investigation on the vortex ground interaction at the same heights above ground and $Re_c = 40 \cdot 10^3$ by Laser-induced fluorescence (LIF) measurement technique. They observed an acceleration in developing a turbulent boundary layer at the ground that detaches and orbits around the primary vortices when the height decreases from $h_{AG} = 0.5 \cdot b$ to $h_{AG} = 0.25 \cdot b$. They also observed an ultimate loss of coherence of the primary vortices and increased turbulence due to advanced mutual interaction.

Furthermore, they recognized for $h_{AG} = 0.125 \cdot b$ laminar flow behavior of the detached flow. They suggested that transition to turbulence in the induced boundary layer does not occur during the fast separation due to proximity to the ground. For all the cases they investigated, secondary vortex formation was not found. In an early investigation by Zheng et al. [17], a comparison of Computational fluid dynamics (CFD) results to field measurements was conducted. They show that secondary vortex formation only takes place for high Re-numbers.

Consequently, increasing Reynolds numbers increase secondary vortex strength and a more complex and severe primary and secondary vortex interaction. Conversely, secondary vortices are prone to rapid viscous dissipation for decreasing Re-numbers, and the interaction with the primary vortices is weak. These findings corroborate the results of Konrath et al. [15] and Cottin et al. [16].

In order to achieve a more refined understanding of the vortex ground interaction for real aircraft, the flow field complexity should be addressed and considered. In-flight practice, the landing of an aircraft consists of four phases. First, the final approach, flare, touch down, and roll-out.Throughout these landing phases, the flow field around the aircraft contains several complex interacting vortex structures with different length scales. The cause is mainly due to the unsteady aerodynamics characterized by the changing angle of attack, flight speed, lift coefficient of the wing in ground effect, and wake vortices increasingly interacting with the ground.

Analytic approaches aiming to estimate the increase in lift coefficient for a wing in-ground effect were carried out by Wisselberger [18] and Prandtl [19] for a two-dimensional aerodynamic profile and Widnall et al. [20] for a three-dimensional wing. The validity of their results is limited to a significantly small ratio of height above ground to the chord length. Furthermore, their potential-flow-based approaches do not consider unsteady aerodynamic parameters and their nonlinear interaction. Therefore, the limitation of the analytical approaches leads to a significant underestimation of the lift coefficient, as shown by Anton et al. [21]. They showed that the presence of the ground results in an increase in pressure below the wing, a reduction of the sink rate, an increase in lift, and a reduction of the induced drag.

Kornev's [22] explanation of the wing effect highlights some important facts. Changes in pressure distribution can sometimes reduce lift, especially with the Venturi effect or extreme ground effect with high lift configurations. When the wing is close to the ground, the pressure increases on the pressure side and slightly decreases on the suction side, which can significantly increase lift without flaps and at small angles of attack. However, if there are strong flap deflections at high angles of attack, the pressure under the wing cannot exceed the stagnation pressure, resulting in a decrease in lift.

Since the lift force compensates for the aircraft's weight force, a reduction in the velocity translates into an increase in the spanwise circulation. The outcome is an increase in the root circulation and, consequently, vortex strength when uniform wing loading is assumed. Independent of the landing phases, the vortices' evolution can be divided into three phases: roll-up, vortex-phase, and decay phase [23]. Until recently, the three-dimensional and nonuniform nature of the wake vortex ground interaction of a real landing aircraft was studied numerically. Daenick et al. [24] investigated with LES simulations the time development of a uniform vortex pair and its interaction with the ground and compared it to the space-developing nonuniform case. In the former case, they found omega-shape-like secondary vortices induced by the primary vortex ground interaction and, ultimately, the development of a turbulent state. In the latter case, three-dimensional deformations resulted in the secondary vortices being stronger with complex structure and interaction, and the observed transition to turbulent occurred faster. Specifically, in the nonuniform case, they forced an axial velocity deficit resulting from the spiral-like roll-up of the vorticity sheet. The result was an axial flow capable of sustaining additional instabilities. Additionally, pronounced meandering of the primary and secondary vortex was displayed in the nonuniform case. Simultaneously, mutual interaction was observed, followed by partial reconnection and vortex bursting that led to breaking down into small-scale turbulent structures.

1.2.2 Ground linking

A step forward was achieved with the recent development of hybrid RANS-LES simulations. Stephan et al., [21] carried out a ground-braking investigation of this kind, where the wake vortices in the LES domain were initialized by the RANS flow field of a real aircraft during landing until touch down. The simulation results show the well-known formation of secondary vortices due to the induced shear layer at the ground by the primary vortices. Successively the secondary vortices tend to detach from the ground and rotate around the primary vortices while interacting. After the touchdown and the cessation of lift production, the vortex system connected by the short-living bound vortex detaches from the wing. The two free vortex ends reconnect with their image vortices at the ground while diverging in the outward direction, as depicted in Fig. 1.1(a) and Fig. 1.1(b).

The ground reconnection phenomenon is known as Ground Linking, which is not frequently observed in field measurements but reproduced in numerical simulations [10]. Furthermore, Stephan et al. show that vortex rebound is more severe at the touchdown zone due to the proximity of primary to induced secondary vortices. Afterward, so-called end-effects are observed, such as the propagation of pressure waves along the vortex axis with strong axial velocities and helical-type instabilities, as shown in Fig. 1.1(b). Independently primary and secondary vortices interaction proceeds while developing omega-shape-like structures with propagation speeds not much related to the end-effects. Successively while the vortices degrade more severely near the touchdown location, spiral deformation proceeded against the flight direction in a contraction-like manner. In the touchdown zone, where the leading vortex ground linking occurs, multiple vortex decomposition follows where each fragment links to the ground linking while divergence is present. Overall, an increase in decay rate due to end-effects and ground interaction is shown compared to the decay for vortices OGE.

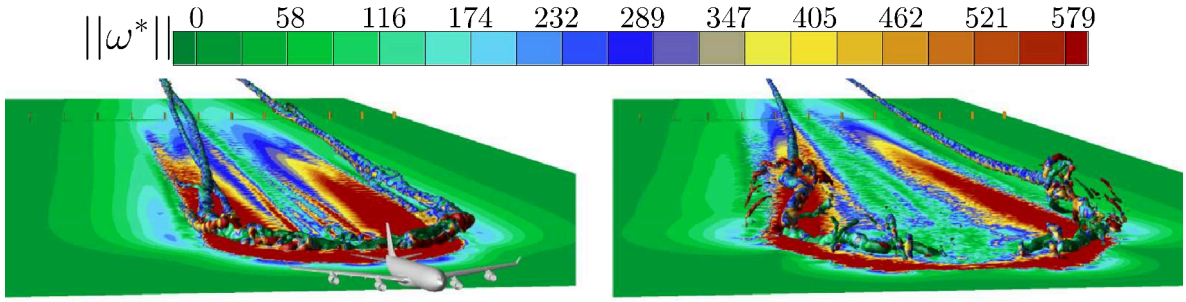

(a) $t^* = 0.04,\ ||w^*|| = 344$ (b) $t^* = 0.11,\ ||w^*|| = 344$

Figure 1.1: Figure from Stephan et al., [21] showing the vortex evolution after ground linking. $t^* = t/t_0$, where t_0 is the time the vortex system needs to descend one initial vortex spacing b_0 and $t_0 = 0$ corresponds to the touchdown. The isosurfaces are at $\omega^* = 344$ and ground colored by vorticity magnitude. Vorticity is normalized by $\omega_0 = 1/t_0$.

Vechtel et al. [25] carried out a similar investigation of this kind. Complementing the findings of Stephan et al., [21] Fig. 1.2 is presented. They describe in Fig. 1.2a) that the detachment of the induced vorticity layer at the ground occurs rapidly due to the close distance to the surface. The newly formed secondary vortex wraps around the primary vortex.

Due to the downwash between the main vortices, the turbulence in the aircraft's wake is propelled to the ground. This turbulence disturbs the grounds' vorticity layer. Consequently, omega shape like structures are created, as seen in Fig. 1.2a). Corroborating the findings of Stephan et al., [21] they report a rapid vortex divergence where the separation reaches a distance of five times the initial vortex spacing at the age of $t_{age} = 19.2s$. Additionally, they mention that the vortices divergence reduces the speed with increasing ground distance. After the touchdown and the deployment of the spoiler devices, the detaching wingtip vortices get disturbed. Due to the pressure difference between the free ends and the less disturbed decaying vortex in the mid-wake region, the vortex experiences end-effects, which cause axial flow along with pressure waves. They report a disturbance propagation velocity of 35 m/s (pressure and simultaneously helical disturbance). They cite Helmholtz's second vortex theorem as the underlying mechanism for the vortex ground linking. The theorem states that free vortex ends can not exist and strive for rapid ground connection. At the linking location, the vortices align up vertically (at a right angle to the ground), as seen in Fig. 1.2b).

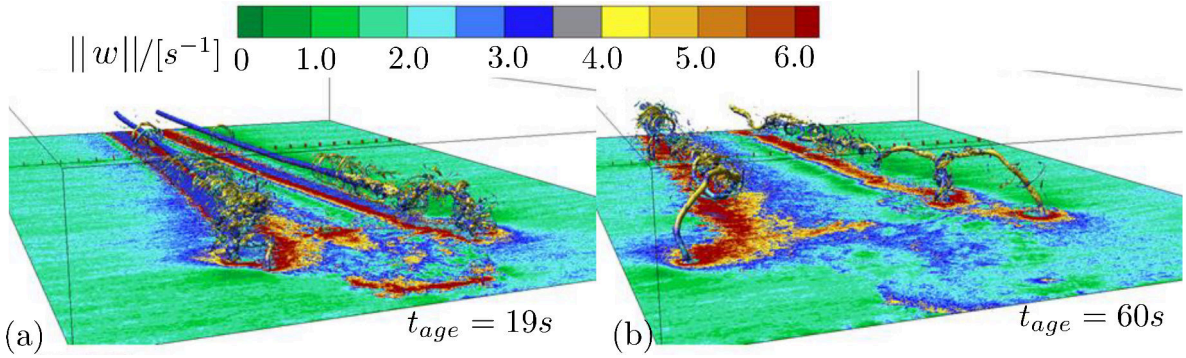

Figure 1.2: Figure from Vechtel et al., [25] showing ground linking end ensuing deformation. $t_{age} = 0$ corresponds to the touchdown time point. The isosurfaces are at $\omega = 3.3[s^{-1}]$ and the ground by vorticity magnitude.

Using solely LES, Proctor et al. [10] investigated the influence on ground linking of relevant vortex initialization parameters such as circulation, initial vortex separation, and generation height together with ambient turbulence. They found that ground linking occurs only for moderate to high ambient turbulence values and that it is insensitive to the rest of the investigated parameters.

1.2.3 End-effects

For real landing aircraft, wake vortex encounters (by the following aircraft) are less frequent than expected. As a possible reason for this, end-effects-related instabilities are suspected [21]. However, end-effects' characteristics in axial pressure and velocity changes that lead to the onset of instabilities still need to be clarified, especially in ground proximity. Furthermore, the relation between axial instabilities and instabilities due to the primary and secondary vortices interaction needs to be explored. Finally, the understanding of vortex stability is less mature than it is for boundary layers; despite that, progress has been made [26].

The stability theory of vortices has evolved into two branches. One deals with instabilities due to the induction of vortex filaments or vortex pairs, as developed by Crow [2]. The second is based on classical normal mode analysis for isolated vortices with the description of the core structure. The study of end-effects belongs to the second branch and grounds an inviscid analysis that reveals the existence of axisymmetric and helical modes [26].

Kornev et al. [27] have proposed various scenarios regarding the evolution of wake vortices and instabilities in the far field considering the ground. The vortex instabilities, which are inviscid, are triggered by lift fluctuations or atmospheric turbulence. They report that these disturbances give rise to growing perturbations into waves at $h_{AG} > 0.575 \cdot b$, evolving at confined tilted planes to the ground. Ultimately these instabilities decompose the vortex system into rings. In the range $0.438 \cdot b < h_{AG} < 0.575 \cdot b$, the vortices deformed to a helix, whereas for $h_{AG} < 0.438 \cdot b$, the instabilities are planar and Crow-like. In this last scenario, the primary and secondary vortex interaction ultimately dominates the vortex stability.

For the specific case of rotating flow without axial and radial velocity components, Rayleigh [28] deduced from the conservation of angular momentum that stability was ensured regarding axisymmetric modes when the circulation increases with radial distance; this is known as the Rayleigh stability criterium. Furthermore, Rayleigh [29] provided an inflection point theorem and stated that a sign-change in the mean vorticity gradient in a confined radial extension leads to instability. Based on the work of Rayleigh, Leibovich, and Stewartson [30] generalized the stability criterium to include the axial velocity component; nevertheless, the condition for instability is sufficient but not necessary.

In order to study the stability of trailing line vortices, models are used, such as the Batchelor [31]. It should be noted that a universal vortex model describing the tangential velocity profile is nonexistent. Several models are in use that best describe the vortex at a particular phase [3]. For the Batchelor vortex model, Lessen et al. [32] show that the most amplified modes are non-axisymmetric. Furthermore, they show that viscosity dampens fluctuations, and possible viscous oscillation modes are not dominant.

Experimental evidence on symmetric and helical type modes for wake vortices is limited mainly because the vortices are extremely sensitive to intrusive measurement techniques. Additionally, vortex meandering precludes their use [26]. Despite that, Singh et al. [33] conducted an experimental investigation in a wind tunnel using hot-wire measurements and naturally occurring turbulence. They measured the wake vortex generated with a wing of a high lift-to-drag ratio. They interpreted their results as evidence of the existence of two instability modes, with the most energy reach(amplitude and magnitude) of the helical type. They suggest that the observed instability characteristics are linked to the axial velocity deficit at the vortex core compared to the outer potential flow and that the onset of instability is due to turbulent fluctuations at a specific frequency range. They did not observe vortex breakdown as the ultimate outcome of the instability development. Later Ash and Khorrami [26] disproved their claims with the argument that upstream disturbances were not controlled and the unsteadiness of the flow field was not considered.

In a more recent numerical study, Moet et al. [34] investigated an isolated vortex and its stability characteristics when subjected to substantial axial pressure variations. They described that decreasing the vortex core diameter along the axial direction decreases the pressure minimum. Therefore, an adverse pressure gradient leads to a pressure wave that increases axial flow from large to small core size. The collision of such waves might lead to vortex bursting. They carried out DNS and LES simulations with vortices subjected to these pressure waves. Unstable helical modes appeared after the passage of the wave. Large helical structures were prominent in DES, with small structures damped due to the higher viscosity, whereas for LES, simulations at realistic Re-numbers finer structures were observed. They also found that the helical instability leads to the amplification of radial velocity modes and velocity in the vortex's outward radial direction.

Note that a distinction should be made between vortex bursting and breakdown and that the relation between the two remains unclear [35]. Vortex bursting is described as the propagation of concentrated flow unsteadiness through the vortex core that redistributes vorticity without destroying the vortex [36]. Vortex breakdown features a rapid and global three-dimensional unsteadiness of the vortex flow with a dramatic increase in the vortex core that breaks down to turbulent flow [37]. Furthermore, motivated by the work of Moet et al. [34], Nybelen and Boussuge [38], carried out on the same verge with a focus on vortex bursting. They found that the severity of bursting in the vortex structure is a direct consequence of the magnitude of the axial wave.

Likewise, the axial wave is in direct relation to the change in the vortex core radius. In both numerical investigations by Moet et al. [34], Nybelen and Boussuge [38], the waves are induced by a change in vortex core radius (note that in CFD experiments, the controlled parameter is the vortex core radius change).

On the one hand, they show that wave magnitude is the relevant parameter on the onset of helical instabilities. Wave magnitudes corresponding to less than 40% of the core radius change result in weak distortion of the vortex structure. On the other hand, when the magnitude of the waves corresponds to a change in core radius in the range of 40% to 50%, severe changes in the vortex structure are locally observed and ultimately lead to the onset of helical instabilities, as depicted in Fig 3. Note that these two numerical experiments only analyze a specific controlled volume of the vortex flow. This piece of the vortex is capable of sustaining stabilities. Finally, increasing complexity, Lonfils et al., [39] investigate the vortex stability numerically when the vortex generator is a decelerating wing. They proved the existence of two instabilities after vortex reconnection, as shown in Fig. 1.4. One is symmetric in the main axis. This axial disturbance is directly related to a pressure surge at the vortex core. The second instability is directly a succession of the first, given that it is strong enough. The second instability assumes a helical shape and is viscous in nature.

The accuracy of CFD in predicting tip vortices can be challenging, as Kornev and Abbas [40] have noted this in their research. However, a possible solution is to combine grid-based and grid-free methods. Birch and Lee's [41] experiments support the findings of Kornev and Abbas.

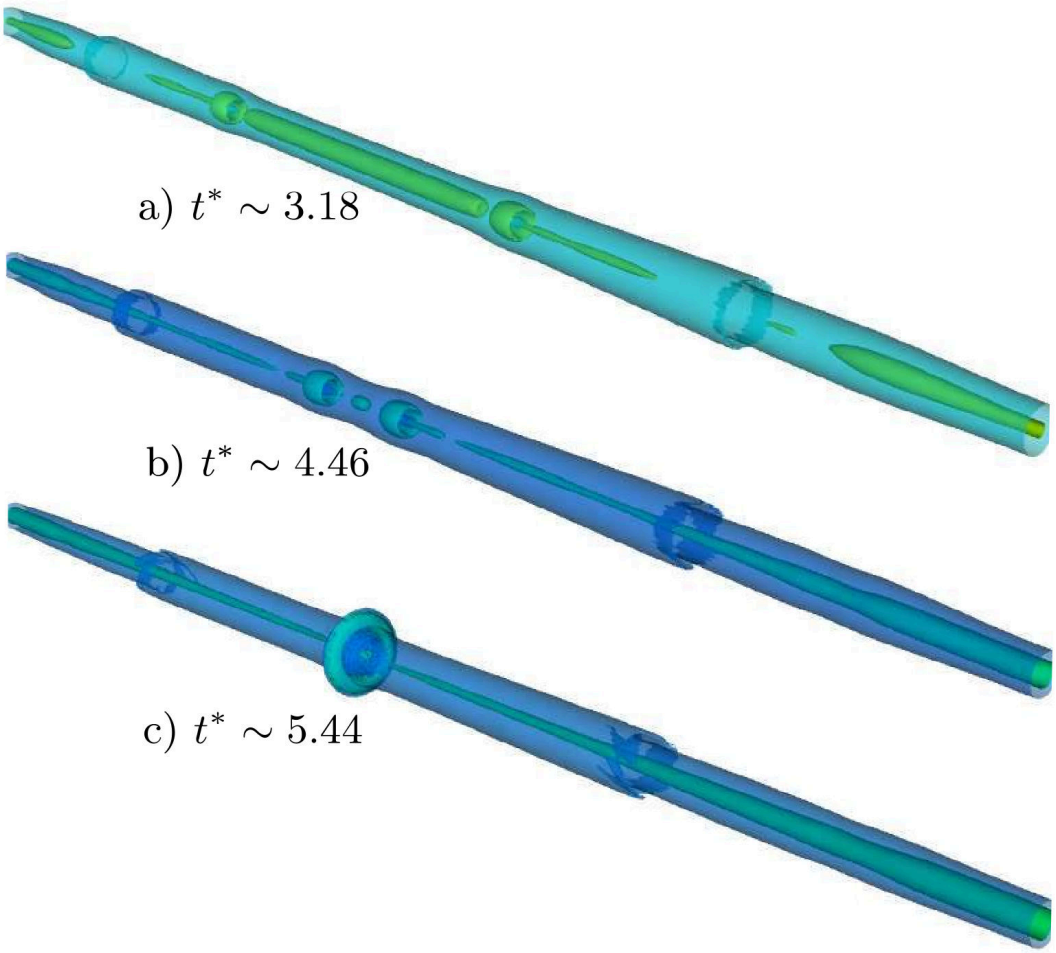

Figure 1.3: Image from Nybelen and Boussuge [38] showing flow disturbances evolving in the vortex core and bursting. Depicted are two vorticity magnitude isosurfaces at three different times. The turnover period of the vortex is used for normalization. $t^* = t/T$ where $T = 2\pi r c_1 / v_{\theta max}$.

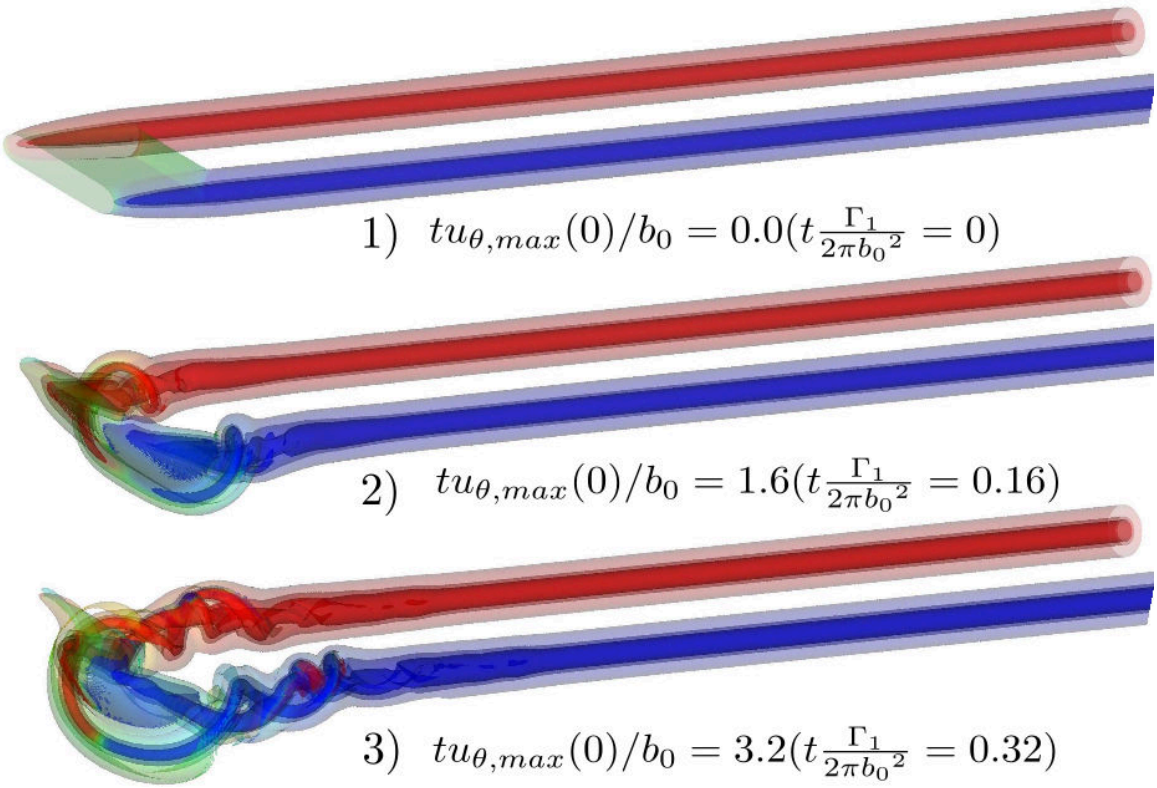

Figure 1.4: Figure taken from Lonfils et al., [39] exhibiting vortex reconnection after the halt of a decelerating wing. The time is normalized by the maximum initial tangential velocity $v_{\theta max}(0)$ and initial vortex spacing b_0. Alternative, the time is normalized by the total circulation $\Gamma_1(0)$ and b_0 (values in parenthesis).

In this context, another study by Feder et al. [42] employed the Computational Vortex Method (CVM) and OpenFOAM simulations to accurately anticipate the behavior of tip vortices in the far field. Their simulations were carefully compared to wind tunnel experiments conducted by Devenport et al. [43], their results agree with the experimental data and showcase the potential of the CVM methods in investigating wake vortices. The combination of these methodologies with hybrid RANS-LES simulation can offer valuable complementary findings to the experimental towing tank investigation presented in this study.

1.3 Layout of the Thesis

In the first stage, the present work focuses only on end-effects. The procedure followed is, therefore, to investigate the deceleration process separately out of ground effect for a constant angle of attack only wing configuration. The most relevant findings of this investigation are published in Castaneda Fuentes et al. [44] In the second stage, presented in the next chapter, the more involved case (landing of an aircraft) is investigated where deceleration is implied in trajectory with horizontal and vertical movement components. The measurements are carried out using particle image velocimetry PIV, mainly in 2D-setup.

The thesis's second chapter describes the experimental setups and all relevant methodologies. The thesis's third chapter deals with a preliminary validation investigation. For the end-effects (first case), an experimental setup that captures the axial flow disturbances was devised, as shown in Figure 1.5, which summarizes the whole range of phenomena under investigation presented in Chapter 4.

In Chapter 5, the ground linking was investigated with an experimental setup depicted in Figure 1.6. Both experimental setups are carefully designed accordingly to the characteristics under investigation. The final chapter 6 of this thesis serves as the concluding section, summarizing the essential findings and insights gathered throughout the research process. This chapter aims to provide a comprehensive understanding of the research topic and its implications and offer recommendations for future studies and practical applications of the research outcomes.

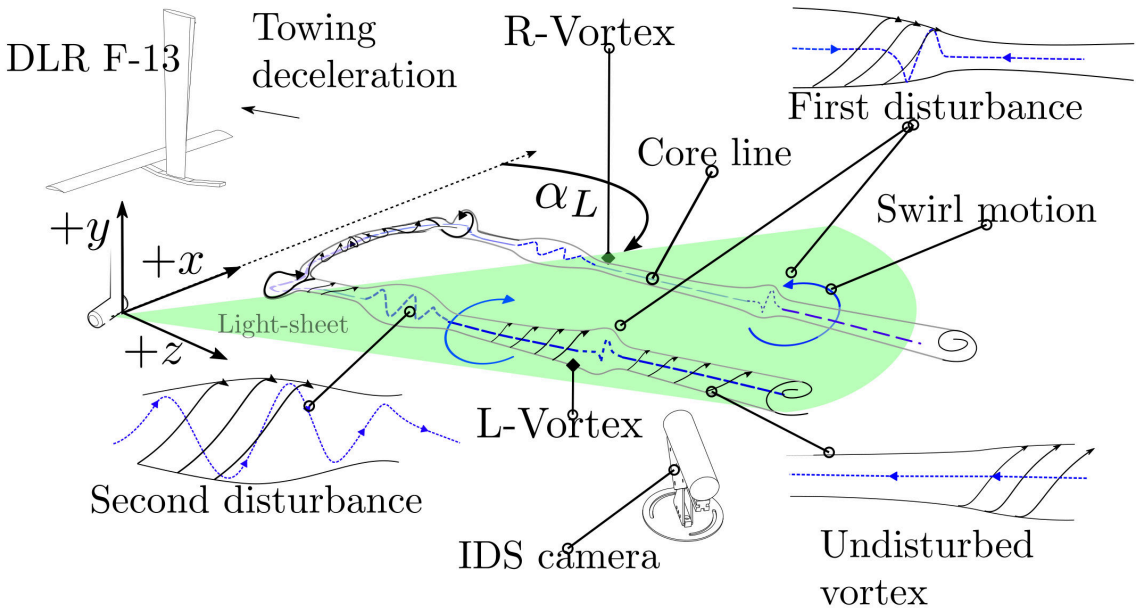

Figure 1.5: Wingtip vortices in the wake of the DLR-F13, with the investigated axial disturbances. α_L corresponds to the Laser-sheet tilt angle. Left (L) and right (R)-vortexes have different ages at the FOV. The depicted topology is based on references [34], [36], [39],and [45] as well as the findings of the present experiments.

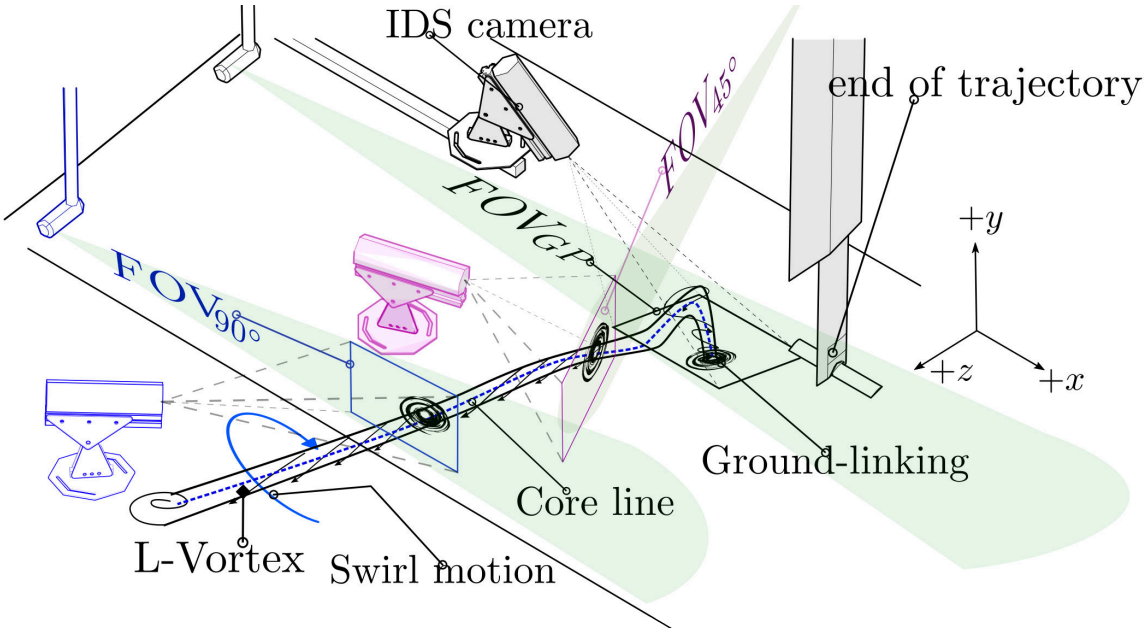

Figure 1.6: Persisting wake vortex displaying ground linking and essential characteristics. Based on the simulation results from Vechtel et al., [25] and Stephan et al., [21], [46], and the observations carried out in the present work. Note that the color coding of the cameras represents a different measurement position (different measurement sequences with the same camera used).

2 Experimental setup

2.1 Experimental hardware and measurement equipment

2.1.1 Towing tank facility

The primary piece of hardware of the towing tank facility is the wagon and its components. It runs on computer numerical control (CNC) and enables model trajectories in three degrees of freedom: two for translatory movement and one for rotational. The main axis is in the longitudinal tank direction and corresponds to the towing direction (horizontal flight). The second translatory axis is perpendicular to the ground, enabling the experimental model to approach the ground (landing). Finally, the rotation axis changes the angle of attack (AOA) during a landing simulation.

In the present work, we use for the end-effects investigation only the translation axis in the longitudinal direction (horizontal flight with deceleration). However, we use all three axes (longitudinal, perpendicular, and rotation) for the ground-linking experiments. The towing wagon can reach velocities of 9 m/s in the main longitudinal direction with an acceleration of 8 m/s^2.

2.1.2 Vortex generator DLR-F13 fixed-wing

The vortex generator's main component is the wing. The wings profile is a Wortmann FX 63-137B-PT designed for high lift at low Reynolds numbers [47]. The airfoil remains the same for the fixed wing and pitching wing models, along with the spanwise length ($b = 300mm$) and chord ($c = 50mm$). In the fixed wing model, the wing is fixed on a narrow fuselage at an AOA of 10°, connected to the towing wagon traverse via a low drag profiled (strut) piercing body as depicted in Fig. 2.1a and Fig. 2.1b. The profiled strut is connected to a piercing body (1700 mm long) with a double wedge hollow section profile (strut), which is joined to the traverse by two stainless steel plates 2.4.

Due to its aerodynamic performance, the DLR-F13 is suited for wake vortex experiments in towing tanks, as described by Carmer et al. [48]. In addition, the model was used in investigations concerning ground interaction [49], [15] and vortex development and decay OGE [50].

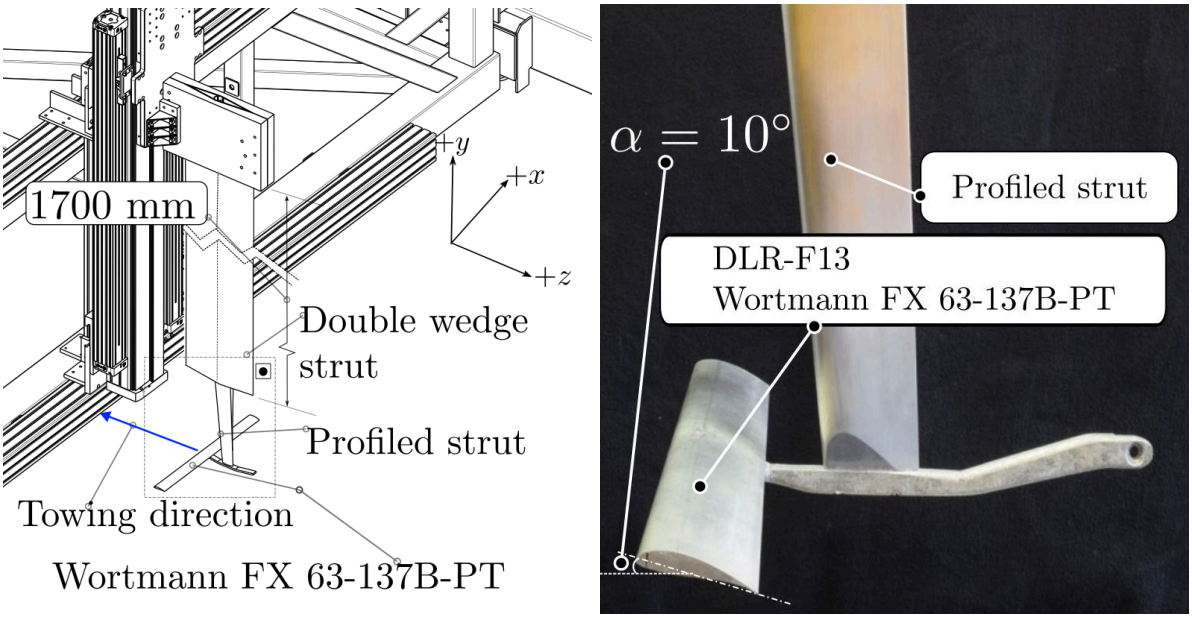

(a) Model mounted on the towing wagon traverse. One translational degree of freedom realized (towing direction).

(b) Foto of the DLR-F13.

Figure 2.1: Fixed wing model DLR-F13.

2.1.3 Vortex generator DLR-F13 pitching-wing

Achieving a dynamic change in the wing's AOA is essential to simulate the landing. Therefore one of the main demands in the early model design was a fast pitching down of the wing at a controlled rate, triggered at a specific location of the measurement trajectory. One of the most important concerns in designing the model was the flow being studied. Specifically, it was crucial that the wake flow of the piercing body and other components did not significantly disturb the vortices. Several restrictions were put in place to ensure this. Consequently, the wing's pitching mechanism is housed inside the profiled (NACA0012) strut and miniaturized as much as possible. The strut is manufactured in stainless steel, and the wing in aluminum. The resulting construction is depicted in Fig. 2.2a and Fig. 2.2b.

The mechanism that drives the dynamic pitching of the wing is initially driven by a servo motor (CHA-58A-160-H-M512-B-R) manufactured by Harmonic Drive SE. The servo motor is embedded in the CNC programming (rotational degree of movement) and actuates together with the longitudinal and traverse axes. The rotation of the motor shaft is converted into a translation movement via a couple of drive rods (upper and lower drive rods) system. The upper rod has a circular hollow section profile, and the lower has a full section profile. The rod system pivots at three positions: the motor shaft crankpin, strut crankpin, and wing crankpin, as depicted in Fig. 2.3.

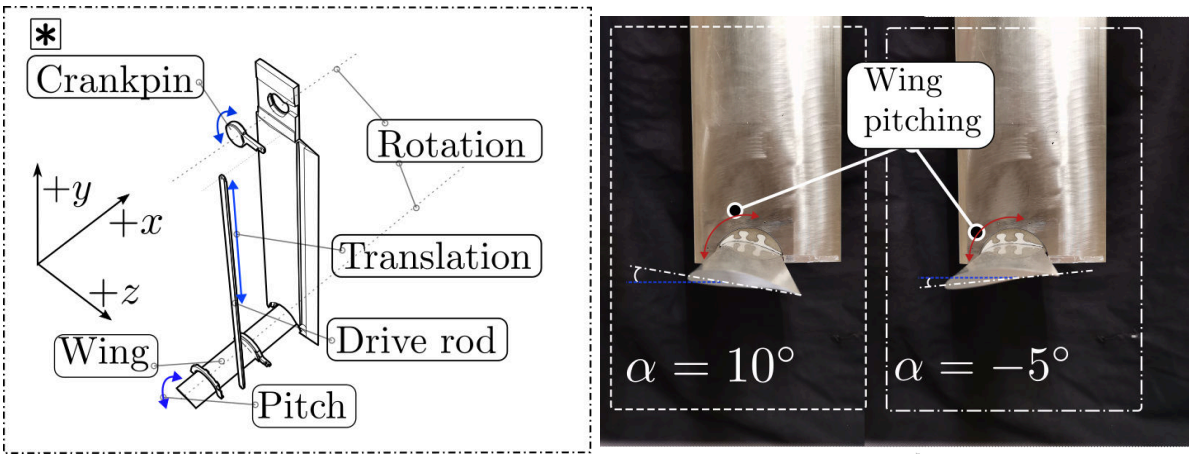

(a) Exploded-view drawing of the wing pitching mechanism and components.

(b) Pictures of the model on the left AOA of 10° for the vortex generation in steady flow regime and right of -5° (not used in the experiments but tested).

Figure 2.2: Pitching wing model and dynamic AOA mechanism.

2.1.4 2D2C PIV measurement system

In the present work, Particle Image Velocimetry (PIV) is the only measurement technique used. The hardware components of the 2-dimensional, 2-component (2D2C) PIV system are selected based on two requirements. The first requirement is the feasibility of appropriate repetition rates of the pulsed laser and camera acquisition (double-frame). The second requirement is the achievable independent arrangement of laser light sheet and camera positioning.

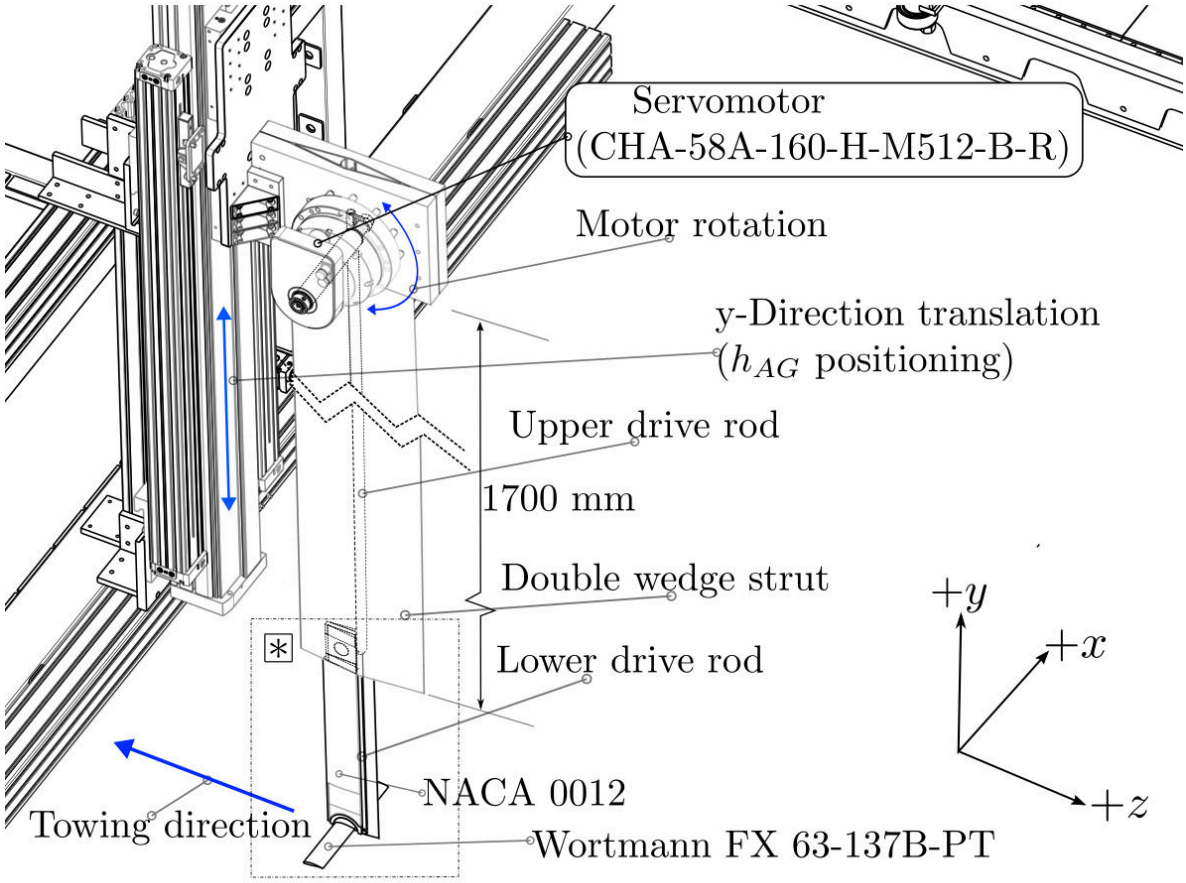

Figure 2.3: Pitching wing model mounted on the height positioning traverse, placed at the rear of the towing wagon. Two translational degrees of freedom can be realized (towing direction and height above ground) as well as one rotational (motor wing coupling by the driving rods)

The former requirement is due to the inherent fast-changing vortex dynamics and the latter to the pronounced three-dimensional vortex structure (setup of perpendicular and tilted 2D planes is required). For these reasons, the laser used is a dual cavity Litron LPY704-100 run at 45 Hz (double frame PIV images) at an output energy of 100 mJ with a wavelength of 532 nm. The laser is placed close to the measurement location parallel to the towing tank. The light beam is first guided to the tank by a Light Guide Arm (2 m) manufactured by Dantec. Then, the guided laser light beam is directed to the water surface with a dual 90° mirror device from LaVision with an Achromatic Galilean Beam Expander (Thorlabs) in between to adjust the beam diameter.

Afterward, the directed laser beam goes through an underwater sheet optics fabricated by LaVision, where the light beam is spread to a sheet. This setup (2D-PIV) uses an IDS camera with a liquid-focusing lens to acquire double-frame images. The camera and focusing lens are housed in a waterproof case. For the synchronization and trigger measurement, a Dantec timing hub is employed.

2.1.5 2D3C (stereo) PIV measurement system

For the stereo, i.e., 2-dimensional, 3-component (2D3C) PIV layout, a system fabricated by LaVision is employed. It comprises a dual cavity Nd: YAG Evergreen 200 Laser with a pulse energy of 200 mJ at 532 nm. The laser is operated at 13 Hz (the same as the cameras i.e., 13 Hz double frame PIV images) and is placed next to the towing tank. The same components are used for the guiding, narrowing, and ultimately spread to a light sheet as in the 2D2C setup. Image acquisition of the double frame stereo images is achieved with two Imager SX 5M cameras. An underwater torpedo houses the cameras, Scheimpflug optics, and remote lenses.

2.1.6 Characterization of seeding particles

Depending on the flow features under investigation, the flow is seeded with three different types of particles. The particles are used alone and in combination. Solid particles used are Vestosint and glass hollow spheres (GHS). As documented by the manufacturer, Vestosint has a mean diameter of 100 μm and GHS of 65 μm. The other particles used are non-solid micro air bubbles (AB). These micro air bubbles have an estimated mean diameter of 100 μm. The methodology of combining seeding particles is grounded on preliminary experiments with solely one particle type.

The vortex core structure is visible and can be measured when the flow is seeded with either GHS or AB. Because of the lower-than-water particle density, the vortices cores display an accumulation of light particles in the center. Despite Vestosint having a density close to that of water, the particle dynamics imposed by the vortices and axial flow do not result in the accumulation of particles in the center. Therefore, combining seeding particles is beneficial since the vortex core region and the periphery (where Vestosint is suitable) are of interest. On the other hand, the drawback of employing non-solid particles (AB) and hollow spheres (GHS) in water is the buoyancy-related vertical speed.

This flow of particles toward the water surface might modify the flow field only under too-dense seeding conditions. Furthermore, the characteristics (diameter and velocity) of the non-solid particles depend on their local environmental conditions, which makes their handling (sustaining appropriate seeding density) challenging. Contrary to non-solid particles, Vestosint particles exhibit a low velocity in the direction to the bottom of the tank; therefore, the handling is less complicated. This situation is again due to their density being barely higher than water. On resume, the disadvantages of one type of particle can be compensated by the other at the expense of a reasonable experimental effort. The seeding particles are distributed before each run, with at least 20 min intervals. This time-lapse is sufficient for the flow fluctuations due to a prior measurement to decay without affecting the successive one [51].

2.2 Measurements layout for the investigation of wake vortices

2.2.1 2D2C PIV setup for end-effects observations and measurements

The hardware components are configured accordingly to acquire visualization data and, most important, quantitative measurements of the vortex system and axial flow estimations. The hardware arrangements are outlined in Table 2.1 (under the column header 2D2C PIV, where the light sheet tilt angle is labeled α_L). An illustration is given in Figure 2.4 and briefly described in chronological order as follows: In case-0, the light sheet is placed in a plane at 90˚ (reference case $\alpha_L = 0°$) perpendicular to the towing path. The light sheet position lies at 22.8 m from the towing tank beginning.

In case-1, the light sheet is tilted 30˚ relative to the untilted case ($\alpha_L = 30°$). Lastly, in case-2, the light sheet is tilted 45˚ (similar to case-2 with $\alpha_L = 45°$). The DLR-F13 model is hung at the center of the towing wagon in a traverse for its positioning relative to the water surface (constant in this experiment) and later to the ground for the landing cases. The depth below the water surface is fixed at (only for this case) 0.45 m (1.5·b). The distance to the sidewalls (symmetric) of the tank is 2.5 m (8.3·b), and to the ground is 2.55 m (8.5·b).

The camera is positioned on a customized structure (fixed at the tank's sidewall) of high stiffness to avoid vibrations at a submersion depth of 1 m and at an angle of 45° (measured from the sidewall to the camera's main longitudinal axis) to the FOV. This distance is suited for capturing the vortex trajectory slot where it sustains disturbances.

Table 2.1: Experimental setup arrangements with the specification of light sheet tilt angle α_L and corresponding placement of components (lengths for the 2D2C- and 2D3C-PIV layouts as illustrated in Fig. 2.4 and 2.5 .

	2D2C-PIV			2D3C-PIV
case-Nr	**0**	**1**	**2**	**3**
α_L	0°	30°	45°	0°
d_1 $[m]$	1.50	3.00	3.15	1.35
d_2 $[m]$	1.15	1.15	1.15	0.35
d_3 $[m]$	1.00	1.00	1.00	1.50

2.2.2 2D3C (stereo) PIV configuration for end-effects measurements

The 2D3C PIV measurements are carried out exclusively using the configuration where the light sheet is perpendicular to the towing direction. These measurements focused on the flow field velocity components in the cross-sectional vortex plane and the axial direction (specifically at the vortex core). The configuration is labeled case-3. The measurement components' positioning is slightly different from the one for the 2D2C case due to the equipment characteristics (mainly torpedo support and FOV range).

The DLR-F13 is located 1 m below the water surface (3.3·b) and separated 1.5 m (5·b) from the left tank wall and 2 m (6.6·b) to the ground. The cameras are housed in an underwater torpedo below the water surface at 1.5 m, as shown in Figure 2.5 (at an angle of 60° [measured from the sidewall to the camera's main longitudinal axis] to the FOV).

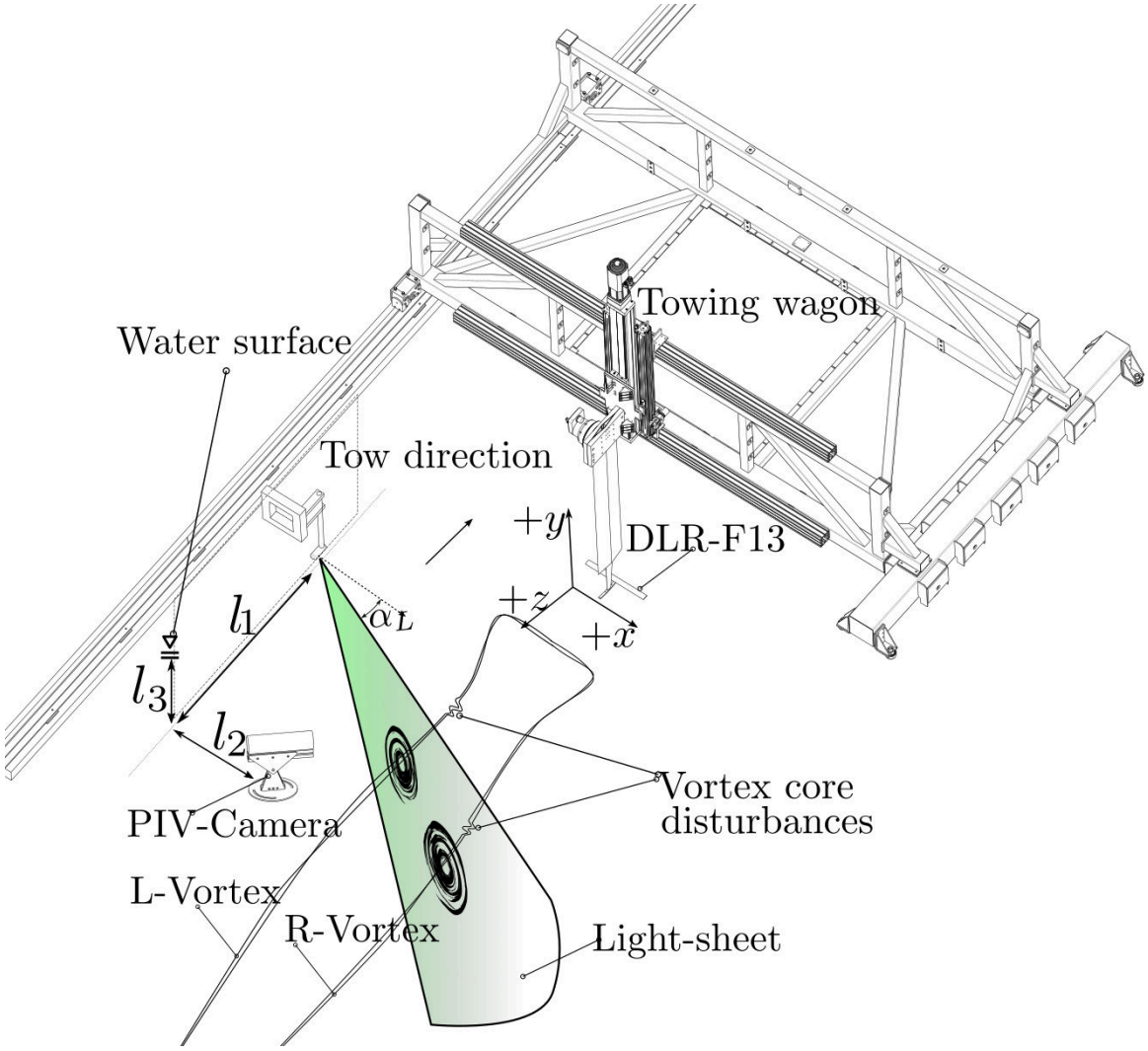

Figure 2.4: Experiment setup for the 2D-PIV measurements. Towing tank facility and wake vortex axial flow produced by the DLR-F13' deceleration.

2.2.3 Overview of the measurement cases for end-effects investigation

Case-0 aims to produce data for comparison with the literature. Therefore, generating reliable data is one of our primary needs, so we begin with a validation study. Case-1 deals with disturbances and a derived estimation of their propagation velocities and their origin (position and time). This estimation is possible through a tilted configuration (30°) and the ensuing offset (temporal) between disturbances in the left and right vortex shed from both wing tips.

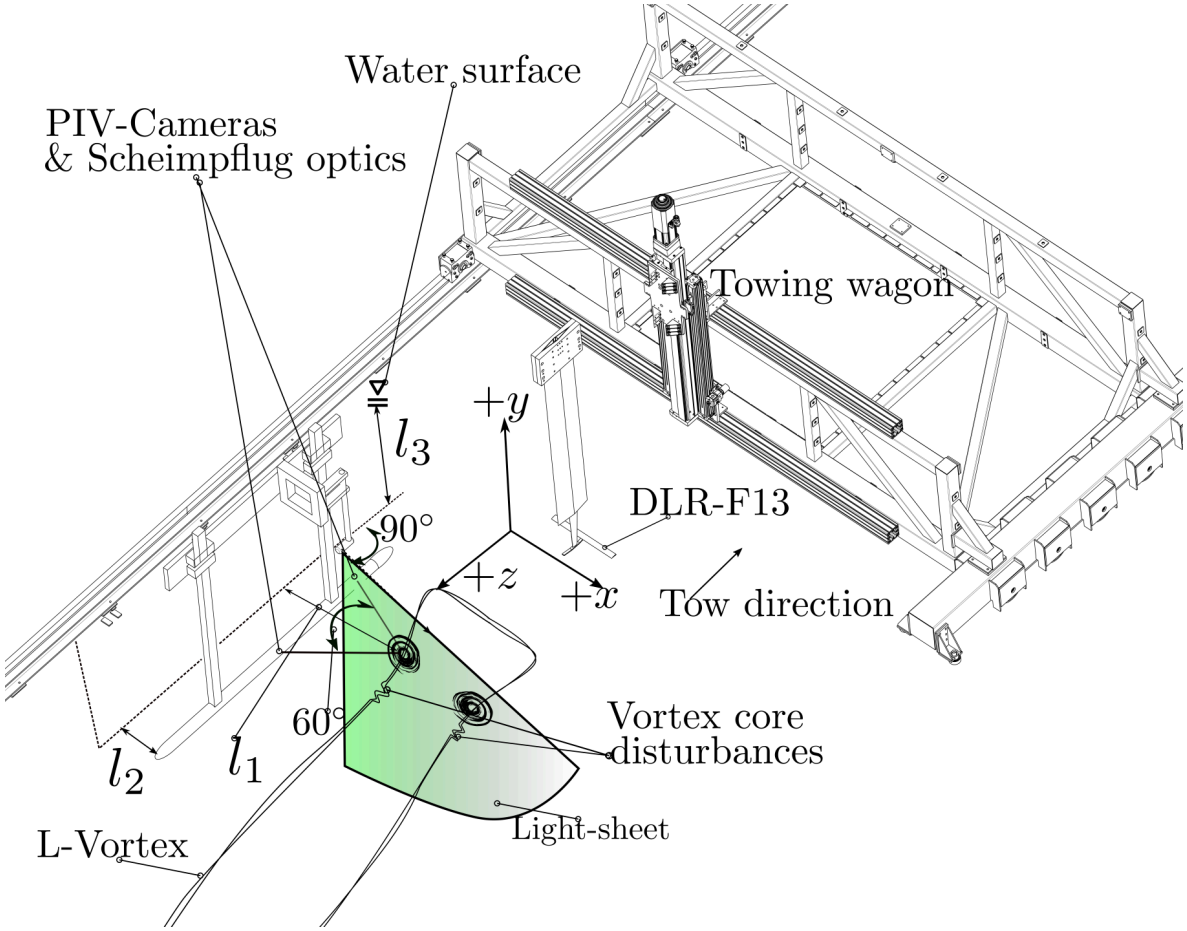

Figure 2.5: Experiment setup for the 2D3C-PIV measurements and equipment hardware. Note that for this case, as depicted in the Figure, the light sheet is not tilted.

Furthermore, this setup enables simultaneous visualization of the disturbances at distinct wake positions per run. It is imperative to acknowledge that the analysis conducted herein presumes that both the left and right disturbances, exhibit identical behavior and symmetry while traveling at the same velocity and originating simultaneously. Correspondingly, the measured velocities in the tilted FOV are a combination of axial and azimuthal components. Nevertheless, this arrangement is valuable for the phenomenological interpretation and explanation of the attributes of the disturbances. Case-2 delivers the data (primarily insightful visualization) in high spatial resolution for the left vortex due to a smaller FOV realized here.

In case-3, all velocity components (azimuthal and axial) are acquired by the 2D3C-PIV measurement technique. Thus the axial flow is measured in the vortex center region along with the observed change from wake- to jet-like flow, as explained in detail later.

2.2.4 2D2C PIV arrangement for ground linking measurements

The following setup was devised to investigate ground linking and the general behavior of the persisting wake vortices near the ground. Three different positions of the light sheet are chosen to capture the wake vortices' behavior in three distinct planes. The data acquired enables the description of the vortex as a whole and a fair description of its 3D characteristics. A preliminary measurement series is conducted to find the most beneficial light sheet arrangements. These preceding observations also give a broad qualitative picture of the phenomena to be investigated. Particularly how the wake vortices are still rolling up immediately after the halt of the wing and the ensuing ground linking. In addition, other characteristics are observed in the vortices, such as their interaction with the ground, meandering, rebound, the formation of secondary vortices, and the induced vorticity layer.

Therefore, the resulting design of the experiments is as follows: Positioning of the light sheet parallel to the ground surface (offset of 10 mm due to the thickness of the calibration target). This configuration enables the measurement of the vortex cross-section parallel to the ground, linking time and vortex-induced velocities. Figure 2.6 displays the placing of the corresponding light sheet at the ground plane. Here two fields of view $FOV_{GP,ref}$ and $FOV_{GP,shift}$ are stitched together as detailed later. Cases concerning the ground plane are given the label GP ($FOV_{GP,ref}$, and $FOV_{GP,shift}$).

In the subsequent case, named 45˚ (Figure 1.6), the light sheet is perpendicular to the ground and tilted 45˚ to the wing's trajectory (the axial vortex direction). The corresponding field of view is labeled $FOV_{45\circ}$. This arrangement's benefit is observing the vortex starting from an old vortex age towards a young vortex age (axial swept towards the heading location). This particular situation is given by the vortex movement relative to the laser position. The vortex sweeps the $FOV_{45\circ}$, entering at a given wake position and exiting at the ground linking position.

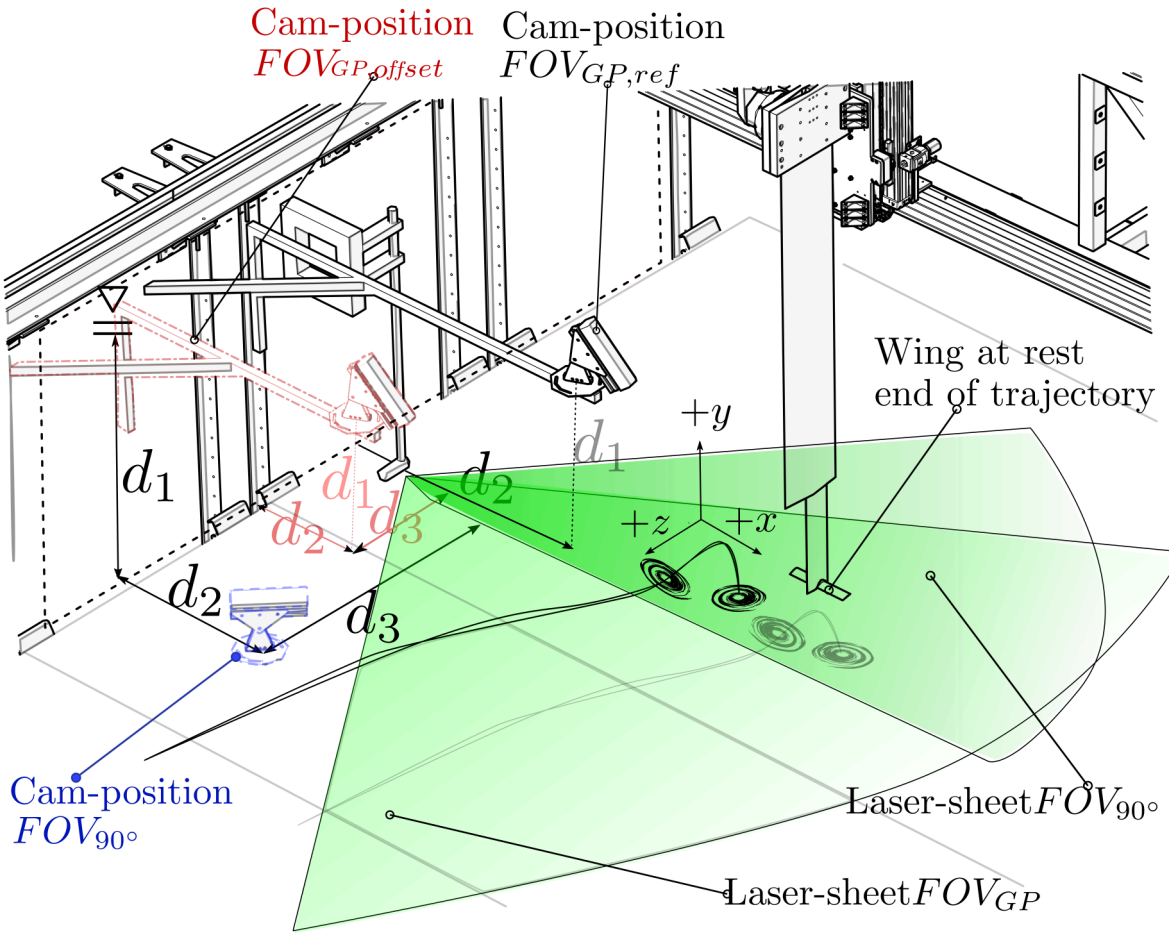

Figure 2.6: Ground-linking measurement setup. The light sheet parallel to the ground is termed FOV_{GP}, whereas the perpendicular to the ground $FOV_{90°}$. Note that the camera positions labeled according to their respective light sheets are for a measure sequence (the same camera is used).

Lastly, in case 90˚, the light sheet is placed at an angle of 90˚ to the direction of towing (cross-section of the towing tank). This positioning is the classic PIV layout; the related field of view is labeled $FOV_{90°}$ and allows measurements of the vortex core trajectory and rebound characteristics.

Table 2.2: Experimental setup arrangements with the specification of light sheet positioning and corresponding placement of the camerarelative to the tank sidewall (lengths for the 2D2C-PIV layout as illustrated in Fig. 2.6 .

	Ground-parallel		Ground-perpendicular	
case-Label	$FOV_{GP,ref}$	$FOV_{GP,shift}$	$FOV_{45°}$	$FOV_{90°}$
d_1 $[m]$	1.00	1.00	0.25	0.25
d_2 $[m]$	0.00	1.00	1.50	1.20
d_3 $[m]$	1.50	1.00	1.00	1.00

2.3 Experimental conditions and cases of study

2.3.1 Decelerating trajectory and end-effects measurement cases

In a preliminary test sequence, we focused on the so-called end-effects (measurement cases for deceleration only). This phenomenon primarily refers to disturbances that travel in the axial direction of a wake vortex. These disturbances are associated with vortex bursting and breakdown. In a flight maneuver, end-effects occur only after a landing since the aircraft can not terminate its movement abruptly in free flight. However, contrary to a flight, this case can be simulated in a towing tank by decelerating and bringing the model to rest, limited only by the deceleration achievable by the towing wagon. The main objective of this experiment was to provide insight into the relationship between the vortex tangential and axial velocity (sustaining disturbances) when decelerating in a horizontal trajectory.

Furthermore, the location where disturbances originate and their propagation velocity were estimated. To this purpose, the vortex characteristics are also derived when the disturbances are present for several Reynolds numbers. The Reynolds number is the variable parameter in many experimental investigations in towing tanks regarding wake vortices. The range of velocities documented is from 1 m/s to 5 m/s. In most of these experiments, the focus lies on two Reynolds numbers (on the order of 10^3). The literature does not provide much insight into the appropriate Reynolds number to utilize; hence it is inferred that the operational parameters of the facility are the deciding factor; this is also the case in the present experiments.

In the preliminary test sequence, Reynolds numbers (based on the length of the profile chord) in the range from $50 \cdot 10^3$ to $175 \cdot 10^3$ are tested, stepped at $25 \cdot 10^3$. The examination of this preliminary data indicates that for Reynolds numbers past $125 \cdot 10^3$, the vortex centerline and disturbances are visible through seeding particles (GHS and AB) entangled at the core. This outcome does not occur for Reynolds numbers below this range, presumably because of the mixture of particle dimensions, light exposition, and strength of the vortex. Therefore, the priority lies on Reynolds numbers above this range $(125, 150, 175) \cdot 10^3$. The trajectory coordinates, along with velocity and acceleration/deceleration over time of the DLR-F13 (wing only), are shown in Figure 2.8. For clarity, only the case $125 \cdot 10^3$ is plotted in Figure 2.8, which corresponds to a velocity of 2.75 m/s.

The examined steady velocities and the resulting Reynolds numbers are outlined in Table 2.3 (the normalization of parameters is invariably marked with superscript $[*]$). The parameter $d^*_{a_0}$ represents the normalized deceleration length, which increases in proportion to the Reynolds number. The value for the deceleration (without normalization) is $a_0 = 1.61 m/s^2$. Thus, the influence of identical disturbance-generating events (deceleration with dimensions) on vortices with different circulation Γ_0 is studied. Furthermore, another interpretation is that when the Reynolds number is increased, the vortex's sensitivity to a given disturbance is less intense due to its upsurge in strength. The normalized deceleration distance, denoted as $d^*_{a_0}$ increases as the non-dimensional deceleration, a^*_0, decreases. The stages of the wake vortex (under investigation here), as categorized by Breitsamter [23], are the extended near-field (z/b $\leq$ 10) and midfield (z/b $\geq$ 10).

Again, the initial data evaluation indicated that the influence on the vortices characteristics (in axial and azimuthal velocity) is negligible when starting the slowdown at distinct locations ahead of the light sheet. In addition, the characteristics of the vortices (namely, tangential velocity and circulation) at the measurement location remain consistent when the vortex parameters are normalized prior to the initial disturbance. This result confirms that the investigations are not carried out in the severe transient near-field or the roll-up range.

In order to disconnect the acceleration range from the rest of the trajectory, a separation plate is positioned at a distance of 3.15 m from the point where the trajectory begins, as shown in Figure 2.7. This plate releases the wake vortex from the end-effects generated by the acceleration. As a result, only the deceleration is left.

Table 2.3: Matrix of measurements for the end-effects investigation. $a_0^* = a_0 b/u_0^2$ corresponds to the normalized deceleration that results from the ratio $a_0 = 1.61 m/s^2$ to steady velocity (three in total for the corresponding Re_c-numbers under examination). Note that u_0 is the free-stream velocity u_∞ and Re_c is computed with the profile chord length c of $0.05m$. The deceleration distance ($d_{a_0}^*$) is normalized with the wing span.

	Measurement matrix End-effects		
Re_c $[-]$	$125 \cdot 10^3$	$150 \cdot 10^3$	$175 \cdot 10^3$
u_0 $[m/s]$	2.75	3.30	3.85
Γ_0 $[m^2/s]$	0.13	0.15	0.18
a_0^* $[-]$	0.064	0.044	0.033
$d_{a_0}^*$ $[-]$	7.81	11.25	15.31

According to a visualization experiment detailed by Bao et al. [52], the vortex system submerges and gets divided at the top edge of the plate. As a result, the remaining vortex portions on each side of the plate attached to it and the propagating axial flow due to acceleration [16] are prevented from interacting with the vortex system under investigation. The reference laser position (not-tilted) is located at 19.8 m from the beginning of the trajectory (case-0 and 3 in Table 2.1 and 0·b in Figure 2.7). When the deceleration begins at this reference position, it is labeled 0·b; at four times the spanwise (b = 300 mm) length forward of the laser, it is labeled 4·b and at eight 8·b.

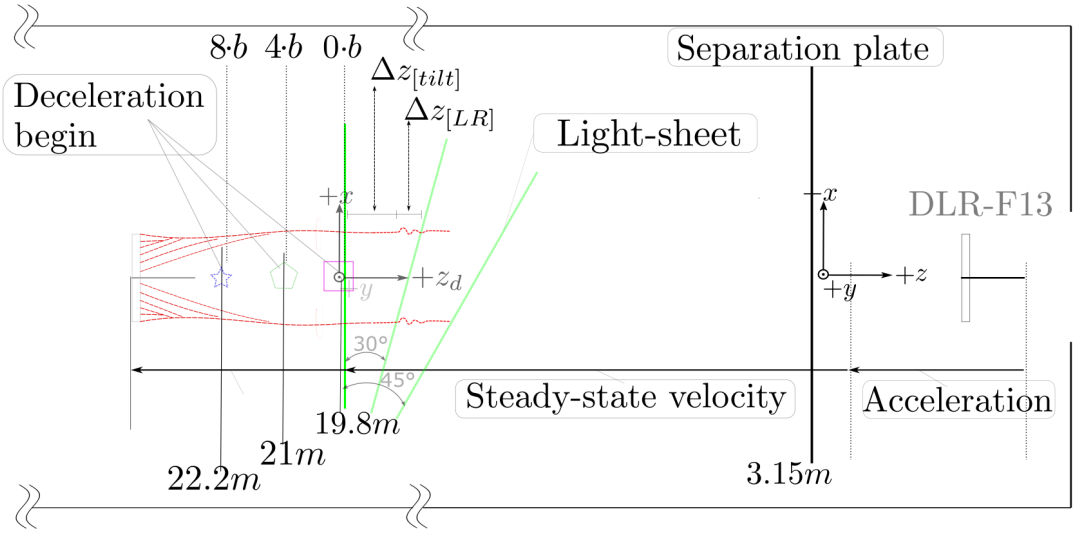

Figure 2.7: Towing tank facility, setup components and trajectory definition for the investigation of end-effects

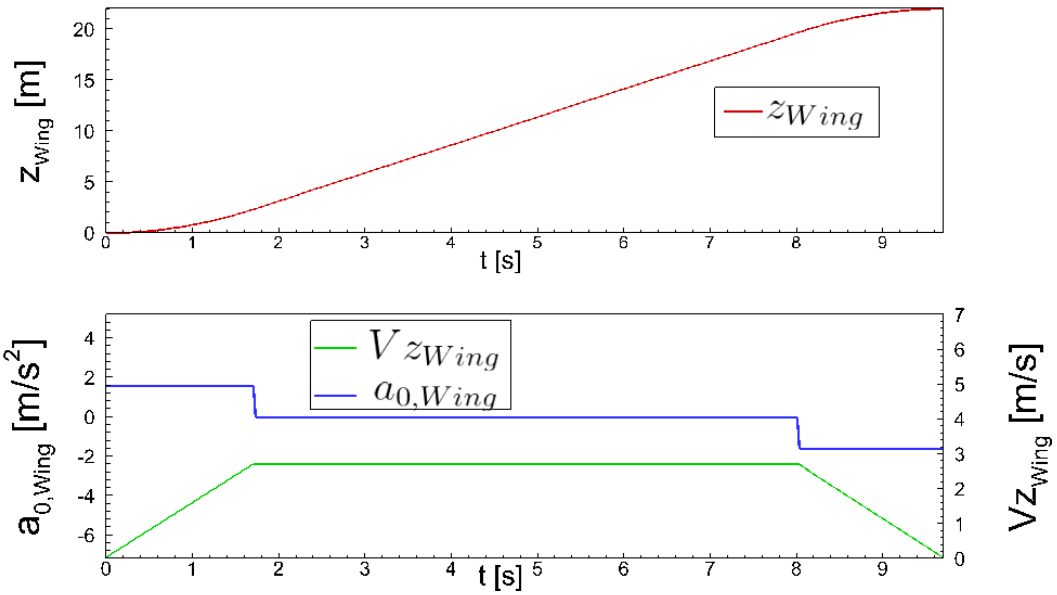

Figure 2.8: Trajectory coordinates. Upper plot: Towing z_{Wing} position, Lower plot: Acceleration/deceleration $a_{0,Wing}$ and velocity Vz_{Wing}

2.3.2 Landing trajectory and ground linking measurement matrix

To investigate the ground linking, it is sought to reproduce a general aircraft's lading under experimental towing tank constraints. In the first instance, these are the scaling down of the vortex generator (DLR-F13 wing) and the dynamic range of the towing wagon. Furthermore, the complexity involved in landing a real aircraft is simplified here for a controlled observation of the dependency of selected parameters. The phases of an actual landing can be distinguished as final approach, flare, and touchdown, as described by Anton et al. [8]. In the present investigation, these landing phases are condensed into only two. One is characterized by a circular arc trajectory while adjusting the angle of attack and keeping the velocity steady (the effective angle of attack remains constant). The second phase is denoted by a constant deceleration with an angle of approach of $\gamma = 5°$, as in actual landings is often the case [53].

The resulting simplified landing takes place at a horizontal distance of about 8 m until a complete stop at a selected height above ground. For this experiment, only one steady velocity magnitude along the trajectory is used, which reads 2.2 m/s. The trajectory data acquired by the towing wagon's control system (CNC based) is shown in Figure 2.9. The upper plot displays the height decrease (reference 0 corresponds to 0.45 m below the water surface) with the horizontal displacement. The plot in the middle shows the components of velocity and position as a function of time, and the bottom is the geometric AOA and rotational speed. The main parameter variation is the height above ground at the end of the landing trajectory. The measurement setup, which was adapted to capture the wake vortex's quantitative and qualitative characteristics, are summarized in Table 2.4.

Table 2.4: Matrix of measurement parameters. Dimensional height above ground h_{AG} and deceleration.

case-ID	**1c**	**2c**	**3c**	**4c**	**5c**	**6c**
h_{AG} $[mm]$	50	100	150	200	250	300
a_{dec} $[m^2/s]$	1.6					
u_0 $[m/s]$	2.22					
$d^*_{a_{dec}}$	5.35					
Γ_0	0.1060					

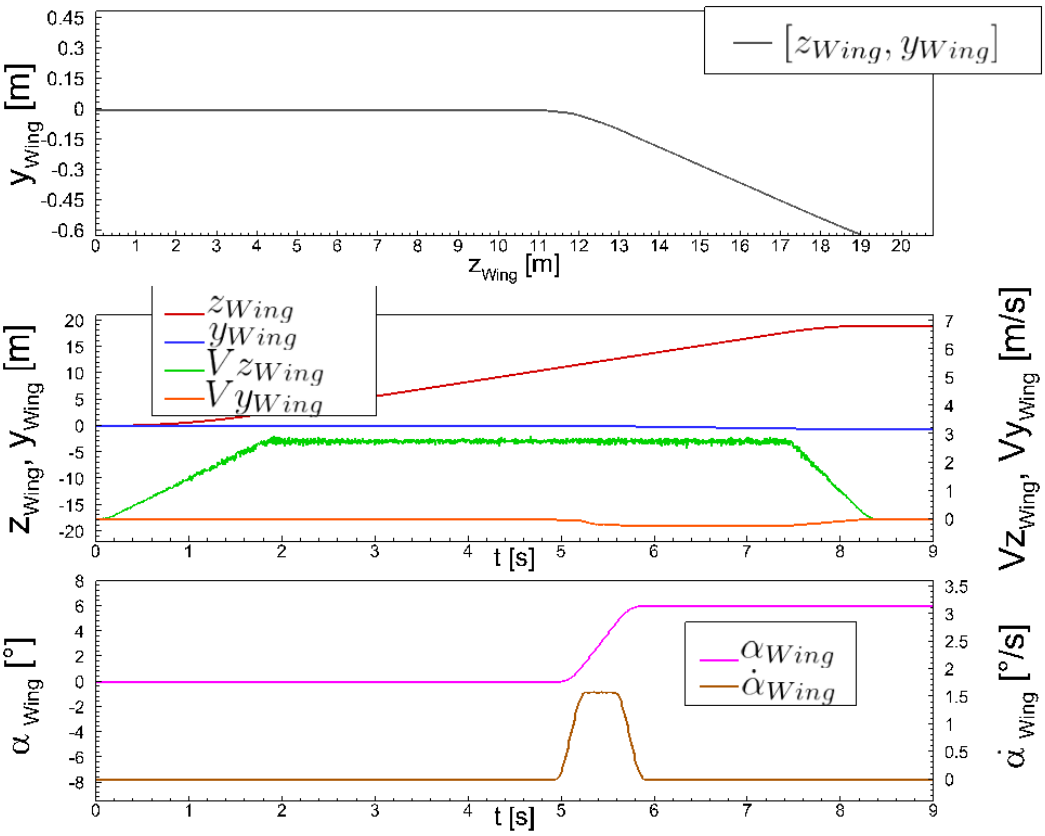

Figure 2.9: CNC trajectory data. The upper plot shows the y_{Wing} coordinate (note that a decrease corresponds to a submersion depth increase) against the horizontal z_{Wing} coordinate. The plot in the middle shows the corresponding components of position and velocity against time, and the bottom plot is the AOA (geometric).

Figure 2.10 depicts the definition of the trajectory schematically together with Table 2.5. In order to clarify the meaning of the adapted setup, the different laser positions alongside a schematic illustration of the vortex core trajectory (dash-dot square outline in 2.10) are sketched in detail in Figures 2.11 to 2.12. The vortex core displacement and the intersection with the respective FOV are shown as the black line. The vortex core tube is shown as the red dash line, where each τ is a vortex age snapshot. The aging of the vortices is therefore given as $\tau_1 < \tau_2 < \tau_3$. As portrayed in Figure 2.11, the lateral and retroceding displacement of the vortex core displays a characteristic movement, which is observed differently depending on the FOV. In the ground plane, it is trivial, i.e., lateral and retroceding displacement (the black line connecting τ).

Because of the superposition of movement in two directions, the vortex core traverses the FOV tilted 45°. This situation is observed in this FOV as an outward movement approaching the ground, shown in Figure 2.12a. This movement (observed in the $FOV_{45°}$) can be explained by the vortex's strong curvature at the ground linking location, which sweeps the FOV. The standard measurement plane configuration is depicted in Figure 2.12b; here, the vortex core follows a curved trajectory (vortex rebound).

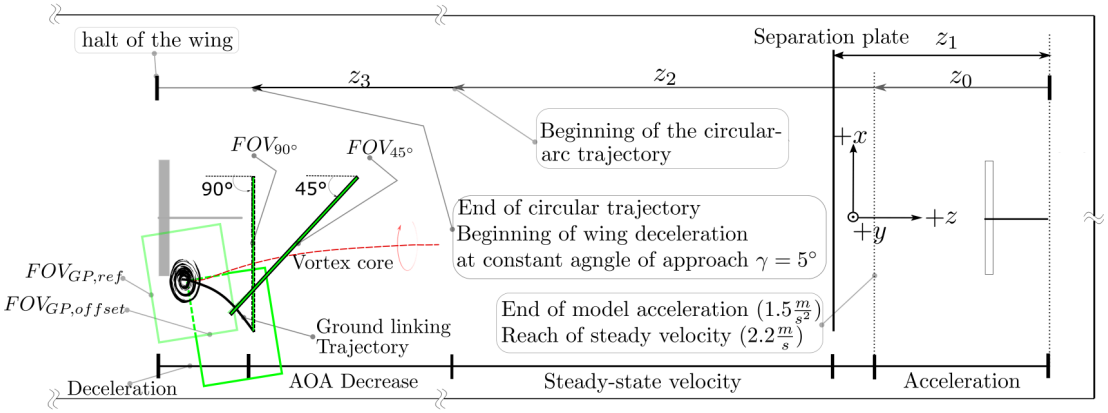

Figure 2.10: Towing tank facility, setup components, and trajectory definition for the investigation of ground linking.

Table 2.5: Entries of relevant trajectory distances in towing direction depicted in Figure 2.10

Distance z in towing direction	
z_0 $[m]$	4.50
z_1 $[m]$	6.15
z_2 $[m]$	11.15
z_3 $[m]$	12.45

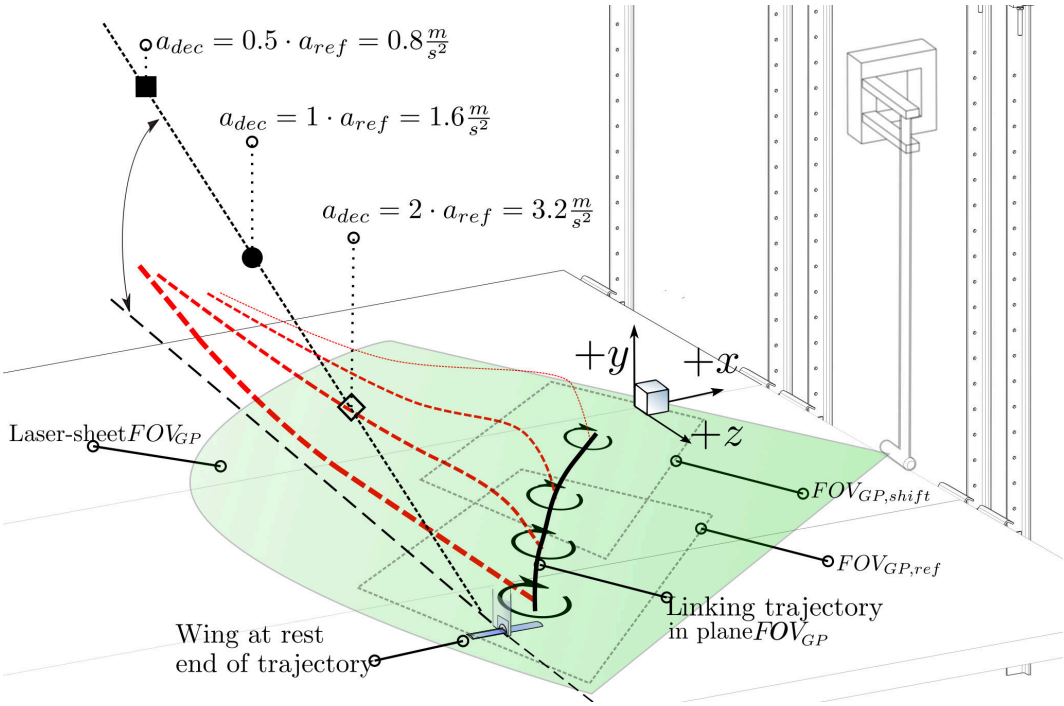

Figure 2.11: Close-up isometric view shows the parallel to the ground surface light sheet with $FOV_{GP,ref}$ and $FOV_{GP,shift}$. The red dashed line represents the vortex core and the continuous movement by only four core lines at different vortex ages.

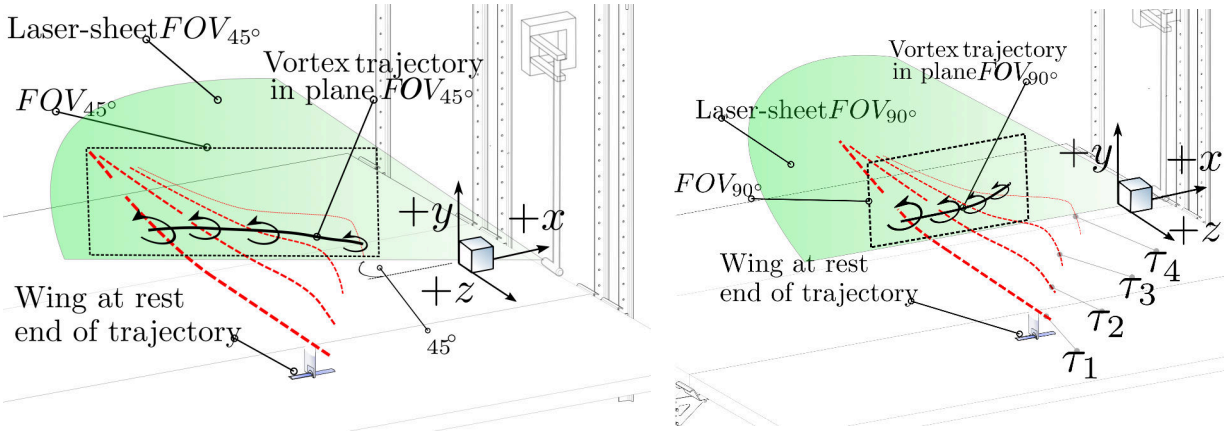

(a) Close-up isometric view $FOV_{45°}$. (b) Close-up isometric view $FOV_{90°}$.

Figure 2.12: Vortex evolution adapted measurement setups $FOV_{45°}$ and $FOV_{90°}$ cases. Increasing τ (four core lines at different vortex ages $\tau_1 < \tau_2 < \tau_3 < \tau_4$) represents the vortex core evolution. The black line describes the vortex core trace from left to right.

2.4 Data acquisition and processing

2.4.1 PIV Velocity fields

The 2D2C measurements are carried out with a FOV of the dimensions 1664×1398 in pixel, equal to 1141×959 mm. Accordingly, the resolution in physical space is estimated to be 22.8 mm. This estimate is based on the 32-pixel size of the interrogation area (IA) and the division sensor pixel spacing over optical magnification (M =1.4 [pixel/mm] for this 2D2C) [54]. The double frame images that result in the velocity vector field sequence are processed in DynamicStudio 6.9 (Dantec) with the incorporated adaptive PIV analysis. The size of the interrogation window is at a minimum of 32×32 pixels to a maximum of 64×64 pixels. The grid step length corresponds to 16×16 pixels giving for the minimum IA an overlap of 50% and for the maximum IA 75%. The vectors are validated via outlier detection within a neighborhood of 5×5 and an acceptance limit of 2 for the N-sigma method used here [55].

Finally, the outliers are replaced successive to the last iteration, and the result is sequences of vector fields. One vector field (from a double-frame image) contains an average of 15,000 single vectors. In the 2D3C measurements, the FOV has a size of 2500×2100 pixels, matching to 200×168 mm. For this case, the estimated spatial resolution reads 2.5 mm. For the estimation, the interrogation window corresponds to 32 pixels and an optical magnification of M = 12.4 [pixel/mm]. The double-frame images are processed in DaVis 10.0 (LaVision software) with a multi-pass method. In the first pass, an IA of 64×64 pixels with an overlap of 75% is used. Sequentially four additional passes are applied with an IA of 32×32 pixels and an overlap of 50%. The 2D3C system delivers sequential vector field data, each containing 10,000 single vectors on average.

Furthermore, the data corresponding to the end-effects investigation shown (2D2C and 2D3C) are averaged for noise reduction. The average used here is over five sequential vector fields. All presented results are the average over five successive vector fields (for the end-effects results). The choice of this averaging method is beneficial in describing the axial flow. This averaging allows for avoiding canceling of positive and negative axial velocity, contrary to the average over several runs (stochastic transition between wake- and jet-like flow).

The accuracy estimation is accomplished by computing the vector statistics of four independent runs. The resulting standard deviation amounts to less than 15% and is attributed primarily to the flow velocity underestimation caused by the restricted spatial resolution as described by Scarano et al. [56].

2.4.2 Error analysis

For the error assessment, we compute the total relative uncertainty (ϵ) following the description of Raffel et al., [57]. This total relative uncertainty is defined by the weighted time between pulses (not to confuse with the acquisition frequency) as $\epsilon = \delta/M \cdot \Delta t$. The displacement error in pixels δ comprises a systematic and a random component (M corresponds to the sensor pixel spacing over optical magnification [pixel/m]). As stated by the PIV system manufacturers (Dantec and LaVision) and by Raffel et al., [57] correct calibration in addition to as specified system operation permits inferring convergence of the total error towards the standard deviation of the random error; hence the systematic error becomes negligible. In this sense, the random error assumes a Gaussian distribution, and an interval of confidence is provided for estimating uncertainty. Using this procedure, the estimation of the displacement deviation is calculated on independent measurements.

This calculation for the 2D2C case is grounded on a cross-correlation peak height ratio algorithm proposed by Charonko and Vlachos [58] (available in DynamicStudio 6.9). The computed displacement deviation amounts to a maximum of 0.7 pixels falling in a confidence range of 68.2%. This displacement deviation translates to a velocity deviation of 0.05 m/s with the values M=1400 [pixel/m] and $\Delta t = 0.01s$. The confidence range remains the same. Finally, the uncertainty in the measured velocity is estimated to be 10% of the maximal tangential velocity (on average 0.5 m/s). In the stereo PIV data, the methodology of error estimation remains the same with the difference that the δ is computed as proposed by Wieneke [59] ($\delta = 0.4$ pixel, M = 12403 pixel/m, $\Delta t = 0.001$ s) with a statistic correlation. The estimated deviation of velocity reads 0.03 m/s, equaling nearly 6 % of the maximum tangential velocity. Note that these estimated uncertainties agree with the previously stated standard deviation based on the vector statistics.

2.4.3 Vortex detection

The vortex center detection is the starting point for the further extraction of derived vortex parameters (described in the following subsection). Unfortunately, a general and precise definition of a vortex is still absent. The consensus is that a vortex is a swirling pattern of a fluid ensemble revolving around a common center [45], [60]. This flow pattern can be regarded as a specific type of coherent structure. Implicitly in the lack of a vortex definition are the unfeasible precise finding of the vortex center coordinates and core extent. Nevertheless, several methods for the determination of these parameters are in use. These methods perform differently depending on the flow field type under investigation, allowing to determine the center in the first instance under necessary assumptions. The vortex center coordinates obtained by each method lie in the same neighborhood for the experimentally obtained data obtained here. The methods used in the present work are four in total. Three are derived from the characteristic equation obtained from the velocity gradient tensor [60], [61]. First, the velocity gradient tensor (VGT) is given in Equation 2.1.

$$D_{ij} = \frac{\partial u_i}{\partial x_j} \tag{2.1}$$

Secondly, because it is a tensor of second order, it can be decomposed in strain rate (symmetric S_{ij} in Eq. 2.2) and rotation rate (antisymmetric Ω_{ij} in Eq. 2.3).

$$S_{ij} = \frac{1}{2}\left(\frac{\partial u_i}{\partial x_j} + \frac{\partial u_j}{\partial x_i}\right) \tag{2.2}$$

$$\Omega_{ij} = \frac{1}{2}\left(\frac{\partial u_i}{\partial x_j} - \frac{\partial u_j}{\partial x_i}\right) \tag{2.3}$$

Lastly, an eigenvalue analysis leads to the characteristic equation for incompressible flow Eq. 2.4 (note that Q Eq. 2.5 is the second, and R Eq. 2.6 is the third invariant, and P equals zero).

$$\lambda^3 + P\lambda^2 + Q\lambda + R = 0 \tag{2.4}$$

$$Q = \frac{1}{2}\big(tr(D_{ij})^2 - tr(D_{ij}^2)\big) = \frac{1}{2}\big(||\Omega||^2 - ||S||^2\big) \tag{2.5}$$

$$R = -det(D_{ij}) \tag{2.6}$$

Q criterion

The Q criterion was introduced by Hunt et al. [62]. It was schemed to specify ranges where the second invariant of D_{ij} is positive and where the pressure is below ambient. Furthermore, the Q parameter can be interpreted as the rotation rate over the strain rate. When the Q parameter is greater than one, it expresses the surplus in the rotation rate. For further data evaluation, a vortex is identified when $Q > 0$.

Δ criterion

The Δ criterion (Equation 2.7) is based on the VGT eigenvalues at the vortex core region. When the streamlines exhibit a closed or spiral-like character, the VGT has one real and two complex eigenvalues. [63]. Furthermore, the discriminant of the characteristic equation is computed. For a $\Delta > 0$, the condition on the set of eigenvalues is given (vortex found).

$$\Delta = \left(\frac{Q}{3}\right)^3 + \left(\frac{R}{2}\right)^2 > 0 \tag{2.7}$$

Swirling strength criterion

This method is derived from the matrix representation of the VGT in eigenvectors and eigenvalues (Equation 2.8). The matrix of eigenvalues can have components, which are all real λ_r or one real and a complex conjugate pair $\lambda_{cr} \pm \lambda_{ci}$. As described by Zhou et al. [64], the vortex streamlines can be represented in a coordinate system ($y_1(t)$, $y_2(t)$ and $y_3(t)$) derived from the eigenvectors ($\vec{v}_r$, $\overline{v}_c r$ and $\vec{v}_c i$) as given in Equations 2.9. This mathematic representation of a vortex enables a direct association of λ_r with the vortex elongation, λ_{cr} with the magnitude of the swirl motion, and λ_{ci} with the swirl frequency (the time required for one revolution corresponds to $2\pi/\lambda_{ci}$). Values of $\lambda_r > 0$ are associated with a vortex.

$$D_{ij} = \begin{bmatrix}\vec{v}_r & \vec{v}_{cr} & \vec{v}_{ci}\end{bmatrix}^T \begin{bmatrix}\lambda_r & 0 & 0 \\ 0 & \lambda_{cr} & \lambda_{ci} \\ 0 & -\lambda_{ci} & \lambda_{cr}\end{bmatrix} \begin{bmatrix}\vec{v}_r & \vec{v}_{cr} & \vec{v}_{ci}\end{bmatrix}^T \tag{2.8}$$

$$
\begin{aligned}
y_1(t) &= C_r e^{\lambda_r t}, \\
y_2(t) &= e\lambda_{cr} t \left[C_{c1} cos\lambda_{ci} t + C_{c2} sin\lambda_{ci} t \right], \\
y_3(t) &= e\lambda_{cr} t \left[C_{c2} cos\lambda_{ci} t - C_{c1} sin\lambda_{ci} t \right].
\end{aligned} \tag{2.9}
$$

Γ_2 criterion

Criteria that depend on spatial velocity derivatives (Q, Δ, and Swirling strength) are problematic when applied to experimental data. False vortex detection arises when the mathematical derivation enhances the measurement error. Therefore an alternative Criterion that provides a reliable vortex detection when the spatial derivative-based fail is the Γ_2. Γ_2 stands for a so-called "pseudo-circulation" [65] as defined in Equation 2.10.

$$
\Gamma_2(\vec{x}) = \frac{1}{S} \oint_{\vec{x}' \in S} sin\theta \, \vec{dx}' \tag{2.10}
$$

The integration that leads to Γ_2 is carried out on a close circular disc area S (containing the point $\vec{x}$). The angle θ arises from the normalized vector cross product [66] $sin\theta = |\delta\vec{x} \times \delta\vec{u}| \; / \; |\delta\vec{x}| \; |\delta\vec{u}|$, where $\delta\vec{x} = \vec{x}' - \vec{x}$ and $\delta\vec{u} = \vec{u}' - \vec{u}$ [65]. A vortex is found in the location where rotation dominates strain($|\Gamma_2| \geq 2/\pi$). Vortex centers are practically identified with the Matlab function supplied by Endrikat [67].

Implementation of vortex detection

As mentioned earlier, the different criteria for vortex detection provide similar results except for the Γ_2 criterion, which is more robust, faster, and consistent. This criterion still finds the primary vortex when the velocity field is quite noisy (robustness). Furthermore, the vortex positions identified by this criterion between successive velocity frames (time sequence of measurement) are in close proximity (consistency), which is a hint of physical plausibility. For these reasons, the first choice is the Γ_2 criterion. The other methods come into play only when the Γ_2 criterion fails to find a vortex.

This procedure is implemented in Matlab with a loop and successive conditional statements with function calls for Q, Δ, and Swirling strength. To confirm the newly discovered center position, it must exhibit a variance of less than 5% from the previous center position. This particular threshold is determined with several measurement runs of the highest data quality. On average, the Γ_2 finds a vortex center in more than 90% of the vector field sequence for a given measurement run.

2.4.4 Derived quantities

After the vortex detection algorithm provides the center coordinates, extracting derived quantities is possible. These post-processing steps are conducted in Matlab and Tecplot. First, velocity profiles are computed with the PIVMat4.10 toolbox made available by Moisy [68]. Velocity profiles are extracted corresponding to the azimuthal average of either swirl velocity (also denoted tangential)$v_\theta(r)$ or axial velocity $v_z(r)$ (only computed in the 2D3C measurements).

Also, the origin of the radial profiles is always placed at the vortex center. Together with the velocity profiles, the vortex's circulation is computed (using $v_\theta(r)$) to characterize the vortices. Direct multiplication of the tangential velocity $v_\theta(r)$ with $2 \cdot \pi r$ (2.12) results in the radial profile of vortex circulation. For cases where an absolute circulation value is required (in an average sense), the Γ_{5-15} is computed. Suited for sub-scale experimental data is the weighted average circulation over the interval $[1/12 \cdot b, 1/4 \cdot b]$ (Equation 2.12) [69], [48], and [70].

$$\Gamma_{5-15} = \frac{6}{b} \cdot \int_{\frac{1}{12} \cdot b}^{\frac{1}{4} \cdot b} \Gamma(r)\, dr \tag{2.11}$$

The reference circulation value for normalization is computed with Equation 2.13 (where AR is the aspect ratio and s the wing load coefficient assume to be $s = \pi/4$ [eliptic distribution]). Furthermore, C_L is the corresponding lift coefficient in the steady-flow regime computed with a 3D wing analysis (Prandtl's Lifting Line Theory based) in Xfoil [71].

Another parameter that is used for vortex characterization is the core size. The definition of the vortex core size is sometimes controversial. However, to align with the current literature, the definition of the core diameter given in Equation 2.14 is used. Here the radial position where the tangential velocity is maximum is assumed to be the vortex core radius.

$$\Gamma(r) = 2 \cdot \pi r v_\theta(r) \quad (2.12) \qquad \Gamma_0 = \frac{C_L u_0 b}{2ARs} \quad (2.13) \qquad v_\theta(r_c) = max\{v_\theta\} \quad (2.14)$$

The vortex age parameter τ in Eq. 2.15 (note that this value is independent of light-sheet arrangements) is used to characterize the temporal development of vortices. This parameter is defined as the time t divided by the vortex-time-constant t_0, as given in Equation 2.17 . Particularly the vortex-time-constant is defined as the time required for the vortex system to move a distance of one vortex spacing $b_0 = s \cdot b$ downwards (due to mutually induced velocity). Consequently, as the Reynolds number increases, the vortex-time-constant decreases (vortex system descend speed increases). Since the PIV velocity fields are inherently time discrete (pulsed acquisition), the vortex age is computed as the product $\tau = \Delta\tau \cdot N_{frame}$ (Frame counter-N_{frame}). In this context, two different $\Delta\tau$ (Δt inverse of acquisition frequency over t_0 Eq.2.16) values are fixed by the hardware components, denoted $\Delta\tau_1$ for 2D2C and $\Delta\tau_2$ for 2D3C.

$$\tau = \frac{t}{t_0} \quad (2.15) \qquad \Delta\tau = \frac{\Delta t}{t_0} \quad (2.16) \qquad t_0 = \frac{4\pi s^3 A_R b}{C_L u_0} \quad (2.17)$$

The different $\Delta\tau$ are summarized in Table 2.6 for the towing velocities examined. For the 2D2C-PIV, the acquisition frequency reads $45Hz$ yielding in $\Delta\tau_1$ and $13Hz$ for the 2D3C-PIV yielding $\Delta\tau_2$.

For the end-effects investigation and free flight cases in general, the instant whenτ is defined as 0 can be arbitrarily chosen. However, the convention is to assume τ to be zero at the instant when the model crosses the laser sheet (start of frame counter $N_{frame} = 0$).

In cases denoted by α_L, the light sheet lies perpendicular to the ground, and the tilt angle (relative to the cross-section of the tank) α_L is equal to either 45° or 30°. In tilted angle cases, the vortex aging is chosen to begin when the leading edge of the profiled vertical strut crosses the light sheet.

Table 2.6: Towing velocity u_0 and the corresponding $\Delta\tau$ computed with the time constant t_0.

	vortex-time-constant t_0 and $\Delta\tau$			
u_0 $[m/s]$	2.20	2.75	3.30	3.85
t_0 $[s]$	3.320	2.656	2.213	1.897
$\Delta\tau_1$ $[-]$	0.006	0.008	0.010	0.011
$\Delta\tau_2$ $[-]$	-	0.028	0.034	0.040

This definition enables to consider the initial $\tau = 0$ as the middle state between the left and right vortex. In the ground linking experiments (landing trajectory), $\tau = 0$ is set the instant the wing comes to rest, therefore independent of laser time crossing.

3 Preliminary validation results

Once ready to recreate representative wake vortices in the towing tank facility, validation measurements were carried out. The setup for this purpose is labeled case-0 (Table 3.1a). In this case, the light sheet is normal to the towing direction (without tilt), as explained in Section 2.2.3. The 2D vector fields of velocity are further evaluated in Matlab as described in Section 2.3. The derived parameters for the literature comparison are vortex core trajectory, circulation, and the vortex core (detailed in section 2.3). These parameters are selected to directly compare the results documented by Carmer et al. [48]. In their experiments, likewise in a towing tank, an upscaled DLR-F13 model is used, resulting in higher Reynolds numbers.

Figures 3.1a and 3.1b depict our measurement results for this validation. Particularly for this case, the origin $(x/b, y/b = 0, 0)$ is set at the center of the left vortex (L-vortex) when the model crosses the laser sheet (following the definition in [48]). The vortex coordinates in the light plane are normalized by the initial vortex spacing value b_0 and time expressed by the vortex age parameter. The captured wake vortex ranges from near- to mid-field ($z/b \approx 10$). The acquired data corresponds to the extended near-field. Here the vortex sheet is still rolling up (note that this only applies to the validation case). The roll-up impact on the vortex core (Fig. 3.1a) can be noticed in the lateral drift towards the wing root in accordance to [72], [43].

Furthermore, the vortex core trajectories do not show irregularities (resulting from wall interactions or vortex disruption due to model misalignment), as shown in Figure 3.1a. Towards the end of the captured vortex path, the distance between vortices is almost equal to b_0, implying that the vortex roll-up is ending for the three Reynolds numbers being studied. Likewise, the computed vortex center distance to the ground reads about 5.5·b. Considering the definition of Robins et al., [4] ($h_{AG} > 3 \cdot b$), the wake vortices are out of ground effect as corroborated in the data. The core radius and vortex circulation corresponding to the vortex plane positions in Figure 3.1a are given in Figure 3.1b.

The values for the core radius stand for the radial distance where the tangential velocity (azimuthal average) is at its maximum. Similarly (using the azimuthal average of velocity), the vortex circulation is computed with Equation 2.11 and normalized. Particularly in Figure 3.1b, the vortices display a simultaneous nuanced radius increase and circulation decrease. The core radius falls into the range of $0.05{\cdot}b_0$ and $0.15{\cdot}b_0$, in agreement with the results reported by Carmer et al. [48]. Due to their upscaled model, the lower Reynolds number they investigated amounts to twice our lowest($Re_c = 125 \cdot 10^3$). Nevertheless, the presented agree with the low Reynolds numbers featuring a larger core radius compared to higher Reynolds numbers. For the circulation, a moderate decaying tendency is observed in agreement with the theory (viscous vortex decay models). This tendency is also reported in field measurement investigations of Burnham and Hallock [73] dealing with vortex dissipation and decay.

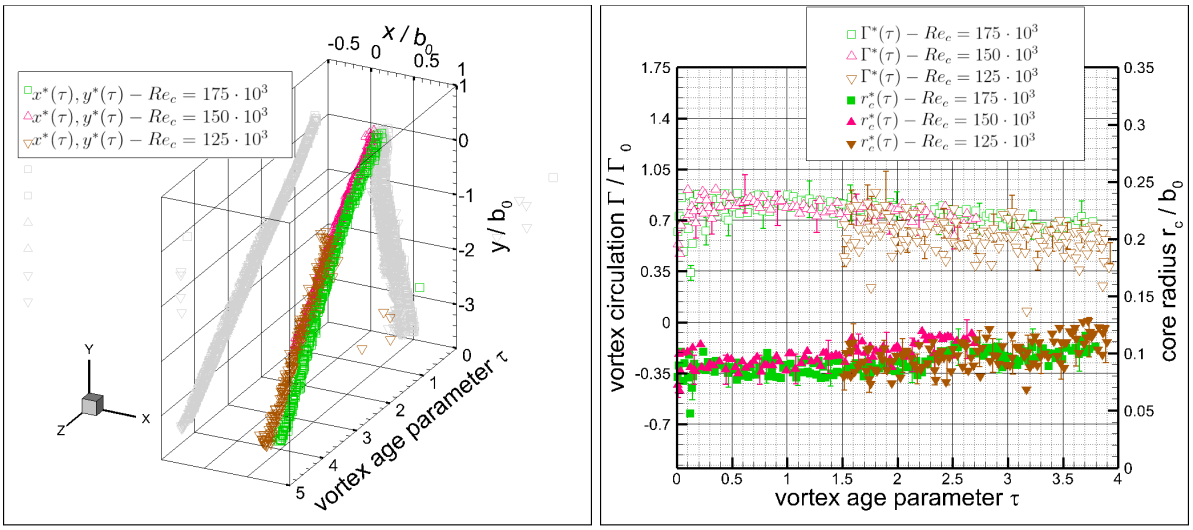

(a) Vortex core trajectory. The x/b_0 coordinate stands for the lateral displacement and y/b_0 for descending.

(b) Vortex circulation and core radius plotted against the vortex age parameter. τ.

Figure 3.1: Validation data for the L-vortex and $\alpha_L = 0°$ (case-0 in Table 2.1) and the investigated Reynolds numbers as given in Table 2.3 .

4 End-effects

4.1 Qualitative analysis of the vortices evolving with end-effects

Visualizations are used to acquire a preliminary understanding of the wake vortex characteristics while the wing is decelerating. For this purpose, the unprocessed PIV data suffices. The visualization depicts axial flow at the vortex center, first towards the model, behaving like a wake and later away from the model like a jet. The terms jet-like and wake-like axial flow are used, as is the case in several publications [74], [75], [76], [77].

The transition from wake to jet-like axial flow is presented in Figures 4.1 to 4.4. Each image is a single frame chosen from the sequence of raw images from the same measurement run. Here the setup corresponds to case-2, where the Reynolds numbers reads $Re_c = 175{\cdot}10^3$. The arrangement of the acquisition equipment is provided in Table 2.1 and depicted in Figure 2.4. The flow is seeded with GHS and Vestosint, and the laser triggered at 45 Hz provides illumination. Due to a high particle concentration, the backscatter lighting is enough to illuminate the trace of trapped (at the center core) particles.

At the beginning of the observation, GHS particles trapped at the vortex center follow the wing rapidly (wake-like). Here the particles follow a smooth and straight trajectory (in the upstream direction), as shown in Figure 4.1, which agrees with the description of Devenport et al. [43]. Shortly after, what is labeled as the first disturbance appears (Figure 4.2), moving away from the wing in the opposite direction of towing (in the downstream direction). Mainly this disturbance is related to the collision of the priorly developed wake-like axial flow still present in the mid-field and beyond with the emerging jet-like axial flow. Therefore interfaced by the disturbance, the transition between wake-like to jet-like flow convects in the direction opposite to the towing.

As a result, the prevailing axial flow at the vortex core behaves like a jet throughout the rest of the observation run (terminated when the vortex leaves the FOV).

The jet-like axial flow displays a decrease in velocity magnitude while the vortex system moves downwards (due to mutual induction). In this stage, the particles at the vortex center follow an irregular trajectory forming a deformed core path, as depicted in Figure 4.3. Succeeding the first disturbance, a second disturbance emerges, as shown in Figure 4.4 (labeled second disturbance).

This disturbance also propagates in the downstream direction but exhibits a longer extent, along with a sinusoidal-like deformation of the vortex core. Shortly after the second disturbance crosses the FOV, the GHS particles detach from the vortex core. The release of seeding particles hints at a rash drop in the pressure gradient (radial) that no longer balances the centrifugal force. Overall, the wake vortex has an estimated length of 18 m and remains in the towing tank long after the observation run. Concerning the location and time, these two disturbances appear; it can be agreed that they occur between starting the deceleration and the complete halt of the wing. This observation is based on the fact that both disturbances show up shortly after the wing crosses the light sheet, and the disturbances travel in the downstream direction.

An estimation of the disturbances' origin and velocity using the 2D2C data is presented later. Corroborating this interpretation, a CFD investigation on a decelerating wing, carried out by Lonfils et al. [39], outlines the occurrence of disturbances. A first disturbance induced by the deceleration that exhibits a surge in the axial flow is observed. Furthermore, they show that this disturbance is axisymmetric. Grounded on the analysis of the present experimental results (discussed later), it is derived that the first disturbance is closely related to the starting of deceleration. The onset of the slowdown is the first event that implies a change in the vortex circulation, which, according to Lonfils et al. [39], is the condition necessary for forcing disturbances. Furthermore, the data suggest that the disturbances take some time to evolve entirely. Taking an alternative perspective, as the deceleration process initiates, the circulation flow toward the vortex experiences a decline, leading to a decrease in the radial pressure gradient as well. Consequently, now in the axial direction, a pressure gradient is created, driving an axial flow from high to low pressure along the vortex axial direction.

Following this interpretation of the underlying disturbance-inducing mechanism, the two events observed (vortex core enlargement and circulation decrease) are described by Moet et al. [34] Misaka et al. [78] and Nybelen and Boussuge [38] as vortex bursting.

A formal definition of vortex bursting is still to be found, but following Spalart [36], bursting displays the spreading of localized unsteadiness in the axial flow. Vortex bursting redistributes the vorticity without ending the vortex. According to the findings of Stephan et al. [21] and Moet et al. [34], the second disturbance assumes helical-like characteristics. This feature is observed in Figure 4.4. Likewise, Lonfils et al. [39] describe this second disturbance as induced by a strong axial flow. In the discussed observations and measured data, this disturbance also takes time to develop, suggesting the wing's halt as the originating event (also reported by Bao et al. [79]). A visualization of the wake vortex right behind the stopping wing is shown in Figure 4.5a.

In this context, Misaka et al., [78] found helical substructures induced by the reconnection of the vortex system. The data strongly suggest that the mechanism behind the second disturbance lies in the interaction of the left vortex, the stopping bound vortex (due to deceleration), and the right vortex, i.e., their reconnection. Again, based on the acquired data (visualization and PIV shown later), the disturbances investigated display the characteristics of vortex bursting. In this sense, it should be emphasized that vortex bursting and breakdown are generally different events but closely related. However, the mutual relation is still to be found [35]. According to Sarpkaya and Daly [37], breakdown exhibits an immediate spread of unsteadiness in three dimensions of flow field parameters in the vortex. The unsteadiness comes with a severe expansion of the vortex core diameter, ultimately breaking down the flow into small, turbulent structures. A visualization of the left (L-) and right (R-) vortices together are shown in Figure. 4.6 (likewise frames of the same run at different times). This run corresponds to case-1, where the Reynolds number reads $Re_c = 125 \cdot 10^3$. The flow here is seeded with AB and Vestosint particles. A pictorial overview of the setup is given in Figures 1.5 and 2.4 in combination with Table 2.1.

Before the first disturbances, the vortices display a beam-like formation of particles in the axial direction seen in Figure 4.6 . This behavior is due to the balance between the centrifugal force and pressure gradient acting on the AB at the vortex center. Therefore particles near the vortex core region accelerate toward the core while decreasing in diameter, as shown in Figure 4.5b . Once in the centerline, the AB diameter does not change significantly. This behavior revealed a clear visualization of the axial flow only at the centerline when it sustained disturbances. However, shortly after the second disturbance propagates, the AB detaches from the vortex center.

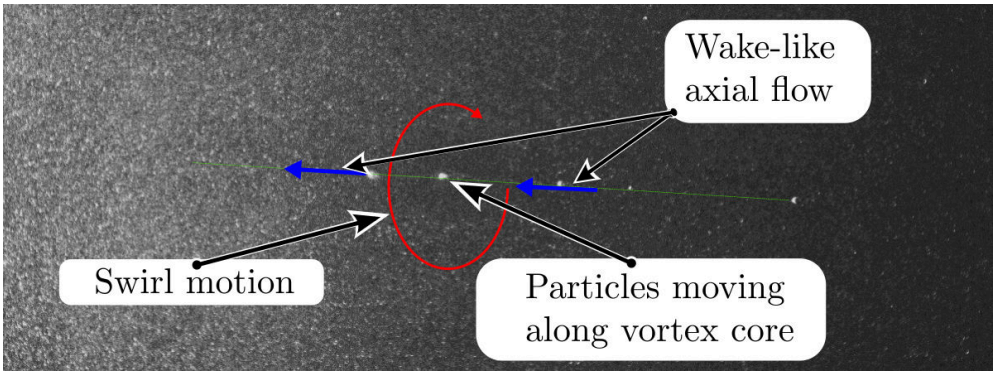

Figure 4.1: Undisturbed vortex axial flow towards the wing (wake-like).

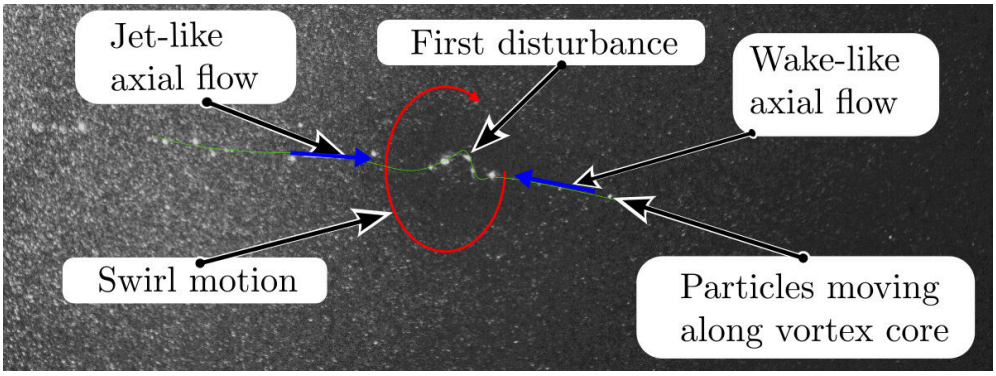

Figure 4.2: The switch between wake- and jet-like axial flow is transported by the first disturbance in the opposite towing direction.

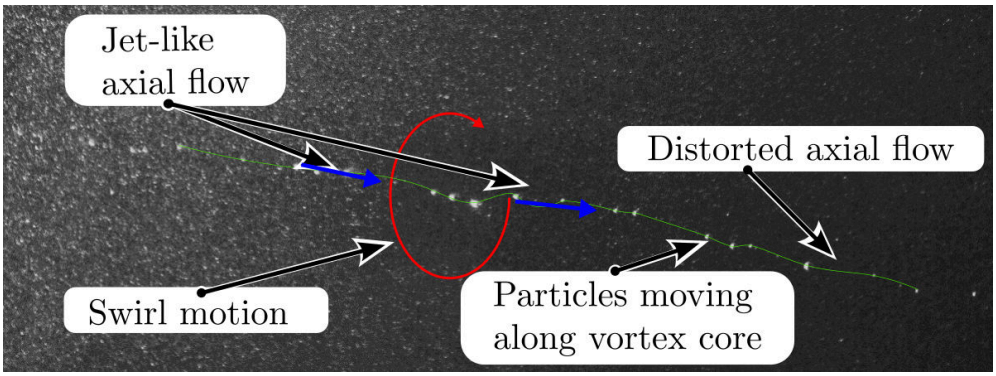

Figure 4.3: Distorted axial flow behavieng like a jet prior to the second disturbance.

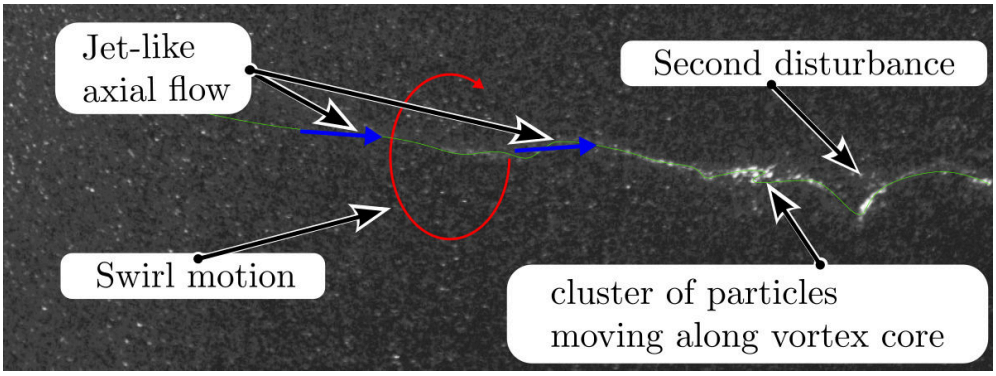

Figure 4.4: Second disturbance and the helical-like topology.

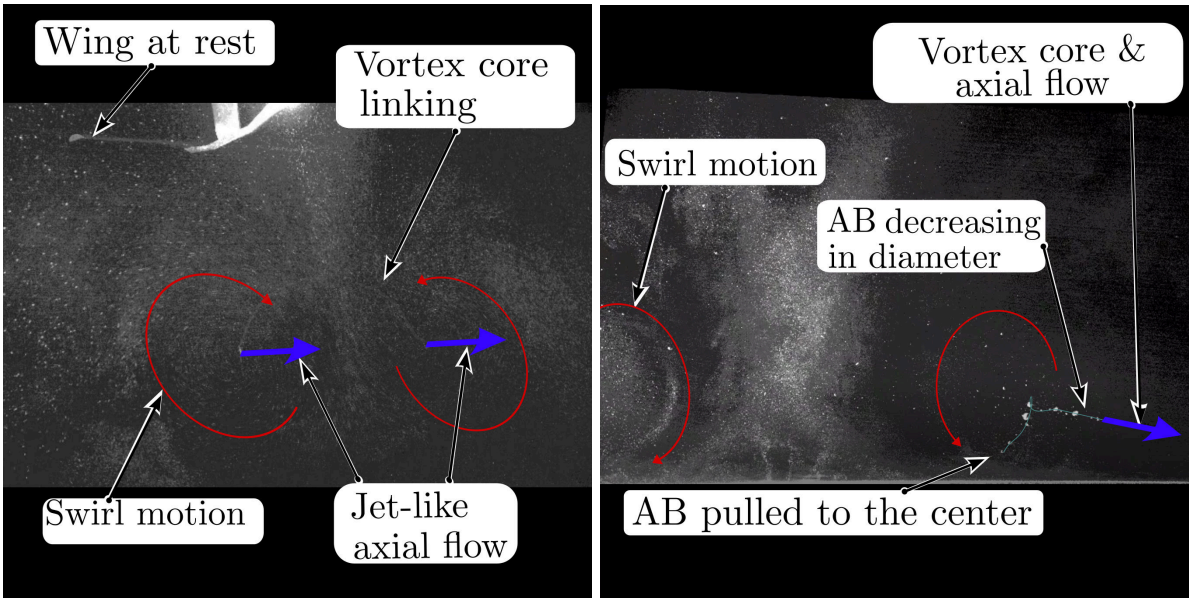

(a) Average image of the wake stopping-vortex displaying vortex reconnection. The small size AB form a ring-like path between the trailing edge of the wing and the light sheet.

(b) Wake vortex axial flow, pulling AB towards the center. Note that in this case (for the purpose of visualization of AB behavior), the seeding takes place from the ground surface.

Figure 4.5: Wake vortex AB visualization, Left: Vortex reconnection after the wing is decelerated and is entirely at rest. Right: AB trajectory and diameter decrease of the decelerating wing.

Therefore an acceleration away from the vortex core takes place. Furthermore, due to the tilted light sheet (30°), the spacing between the left vortex (L-vortex) and right vortex (R-vortex) forms the hypothenuse of a right triangle. Therefore the disturbances in the R-vortex must propagate an additional distance $\approx 0.5 \cdot b$ (opposite leg of the triangle) until showing up at the light sheet. Consequently, the switch between wake-like to jet-like axial flow features a time lag between the L- and R-vortex (in the tilted sheat).

This condition describes the disturbance implication on the vortex parameters in relation to a prior vortex age. Therefore Figure 4.6a shows the first disturbance in the L-vortex only with a sinusoidal-like deformation implying jet-like axial flow. The R-vortex features a prior-to-disturbance contraction (outlined in the measurements discussed later), hinting at a wake-like axial flow.

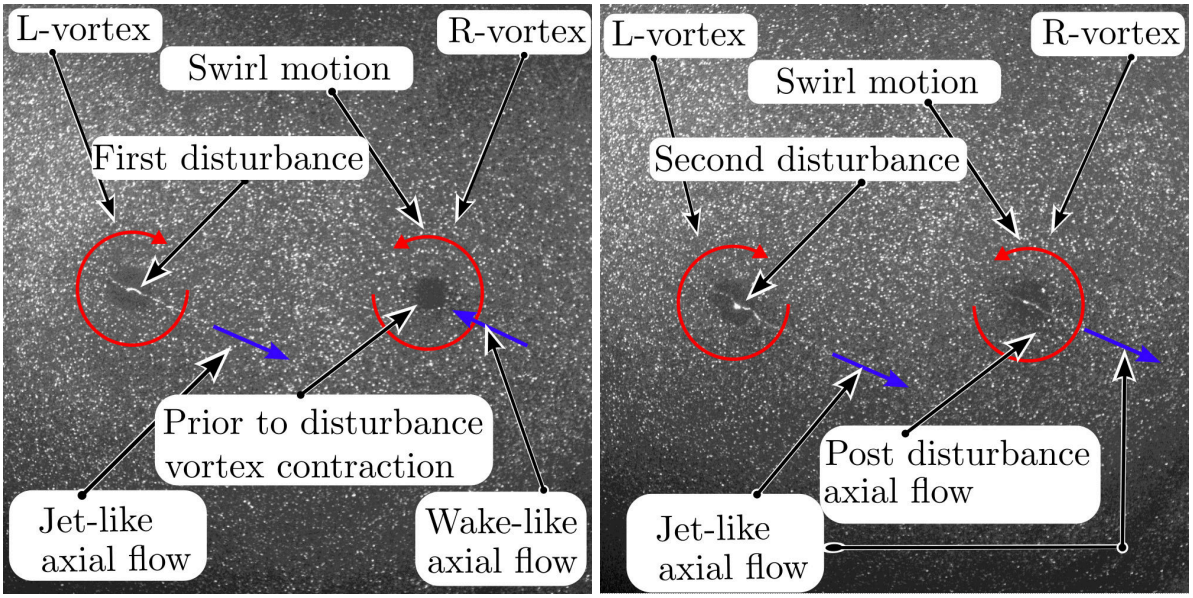

(a) jet-like axial flow for the L- and wake-like for the R-vortex. The first disturbance arrives at the FOV first for the L-vortex.

(b) The second disturbance reaches the FOV for the L-vortex first, while in the R-vortex, the first leave with a delay.

Figure 4.6: Wake vortices at different ages for left and right(jet-like axial flow for the left and wake-like for the right) due to the tilted light sheet. The first disturbance arrives at the FOV first for the L-vortex 4.6. The vortex age difference between Fig. 4.6a and Fig. 4.6b corresponds to $\Delta\tau \approx 0.8$

In Figure 4.6b , a similar sequence of events is shown at a later time. Here the second disturbance is visible at the L-vortex, while in the R-vortex, a post-disturbance state. Again the second disturbance enforces a spiral-like deformation of the vortex core along a surge in particle concentration. At this stage, jet-like axial flow prevails for L- and R-vortices.

4.2 2D2C PIV Measurement results and analysis

The raw data (from which Figure 4.6a is taken) obtained with the setup configuration shown in Figure 2.4 was captured to investigate the wake vortex depicted in Figure 1.5. For this purpose, case-1 is selected (Table 2.1), and the deceleration begins at $8 \cdot b$. The post-processing steps leading to the results presented in the present section are described in Section 5.1. These are (in chronological order) the calculation of the 2D2C velocity fields, vortex center detection, and the extraction of derived parameters.

The vorticity in the axial direction is shown as a contour map superimposed on the velocity vector field. As described in Section 2.3, the derived parameters swirl velocity (tangential) and circulation are displayed as radial profiles. Due to the tilt of the measurement plane, the left and right vortex feature an offset in their age. This condition is assumed to be equivalent to the simultaneous measurement of the vortices at different axial positions separating the R-vortex by a distance of $0.5 \cdot b$ further downstream (see Figure 2.7). The corresponding offset in vortex age reads $\Delta\tau_{[LR]} \approx 0.25$. The vortex-age offset is computed by scaling the $\Delta\tau_1 = 0.008$ with the corresponding frame count starting when the first disturbance arrives at the FOV in the L-vortex and ending when it arrives at the R-vortex (around 32 frames).

The relevant findings are described using three instants of time, focusing only on the first disturbance here. These instants are 1) Right before the first disturbance reaches the FOV in the L-vortex. 2) Same event as 1) on the R-vortex and 3) Right after the first disturbance leaves the FOV in the R-vortex. The selected Reynolds number reads $Re_c = 125 \cdot 10^3$. For the instant 1), Figure 4.7a shows the velocity field, and Figure 4.7b the extraction of the tangential velocity and circulation radial profiles.

As shown in Figure 4.7a ($\tau = 1.6$), before the first disturbance reaches the FOV (L-vortex), there is a slight increase in the swirl velocity and a vertical elongation of the vortex (compared to the undisturbed case). At the same time, the deformation is moderate on the R-vortex (non-symmetric). The maxima of the radial profiles increase due to the increased swirl velocity. However, besides the raised maxima of the L-vortex, the velocity profiles for both vortices remain similar before equalizing at $r = 0.3 \cdot b_0$. The raised maxima in the L-vortex enhances the vortex circulation maxima, as shown in Figure 4.7b.

However, the circulation increase remains contained in the core region (up to $r = 0.3 \cdot b_0$). At a radius past $r = 0.3 \cdot b_0$, the tangential velocity and circulation profiles even out, with deviation due to the measurement noise, which scales as the radius increases.

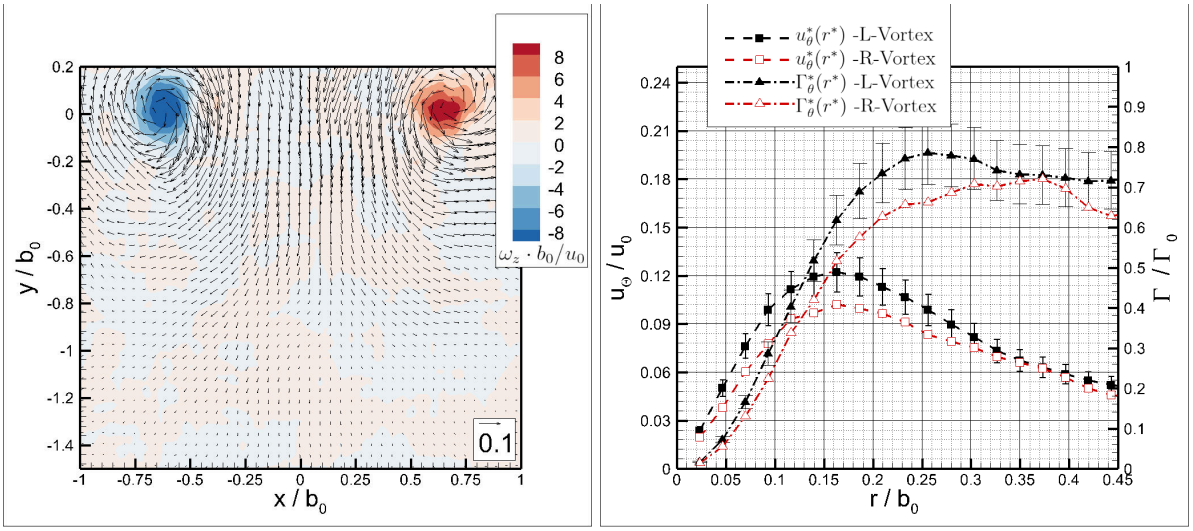

(a) Velocity field and vorticity.

(b) Tangential velocity and vortex circulation.

Figure 4.7: Wake vortex measured velocity and derived parameters for the L- and right R-vortex at $\tau = 1.6$ ($\alpha_L = 30°, Re_c = 125 \cdot 10^3$).

The next time instant 2) ($\tau = 2.4$), the R-vortex features a similar sequence of events (prior to the first disturbance) Figures 4.8a and 4.8b . However, axial symmetry increases. This difference is assumed to be the consequence of the further downstream observation position of the R-vortex. In the L-vortex, after the first disturbance leaves the FOV, the vortex core displays an increase in diameter along a flattening of the boundary (swirl velocity maxima). Furthermore, the L-vortex deformation is now symmetric 4.8a . Furthermore, the maximum swirl velocity of the R-vortex moves towards the center while at the same time increasing to reach a value of about $0.1 \cdot u_0$.

This increase in swirl is reflected in the circulation enhancement and redistribution in the core region. Due to the definition chosen for the vortex core, the term contraction is convenient (note that by using a different core definition, the discussion will be about a shift in maxima). In conclusion, up to this point, the first disturbance implication on the vortex flow is consistent (almost identical behavior on L- and R-vortex).

The term vortex contraction is used by Misaka et al. [78] in the vortex bursting context, also referred to by Spalart [36]. The descriptive explanation given by Spalart [36] relates to the contraction at a given vortex location and an expansion at a different location (simultaneously on the same vortex). Furthermore, Fabre et al. [80] report vortex deformation of contraction and expansion type due to the spreading of Kelvin waves, which are axially symmetric. The implication of Kelvin waves is the alternation of low and high axial vorticity induced by the stretching and compressing of the vortex by the axial flow.

Despite the description of Fabre et al. [80] emphasizes standing waves, it can be inferred that the conditions required for this to occur in the present experiment are given. Particularly Fabre et al. [80] suggest that the superposition of waves traveling in opposing directions results in a standing wave. It can be assumed that the visualization and indirect measurements of vortex contraction result from the non-linear [38] interplay of bursting and Kelvin (short-living) waves. Using the 2D3C PIV data, radial velocity profiles and the time evolution of radial flow rate are presented and discussed in the next section. The last time instant 3)

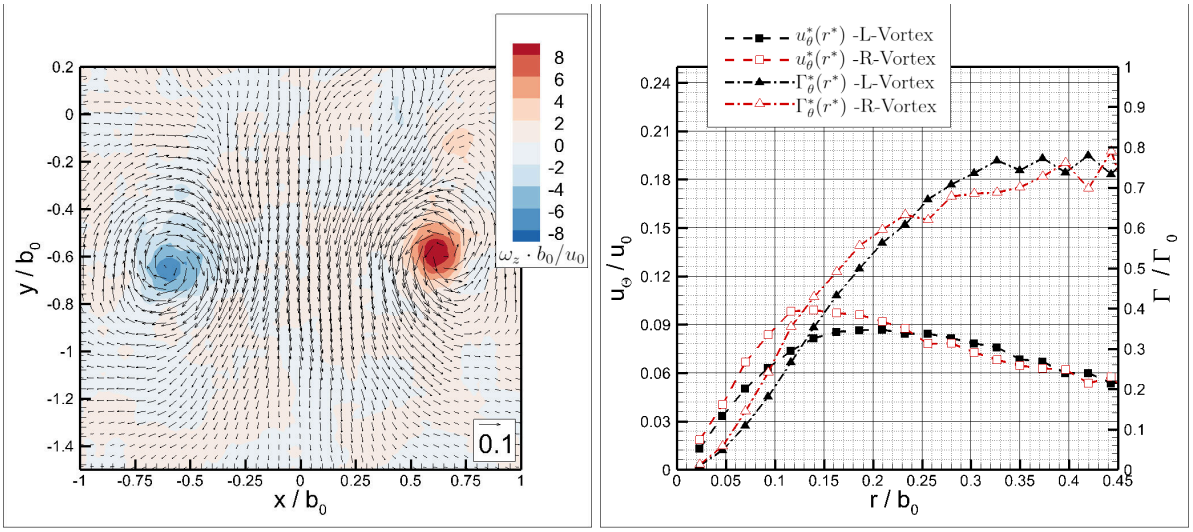

(a) Velocity field and vorticity.

(b) Tangential velocity and vortex circulation.

Figure 4.8: Wake vortex measured velocity and derived parameters for the L- and right R-vortex at $\tau = 2.4$ ($\alpha_L = 30°, Re_c = 125 \cdot 10^3$).

under discussion corresponds to $\tau = 3.9$. Here L- and R-vortex feature jet-like axial flow.

Despite the measurement at different axial locations between L- and R-vortex, the radial profiles of velocity and circulation fall on top of each other, as depicted in Figure 4.9b . A similar observation can be made for the velocity field (Figure 4.9a), differing in symmetry due to the age difference. Furthermore, the vorticity boundary is diffused but still similar for both vortices. This condition is reflected in the corresponding smother swirl velocity profile with a peak at about $0.09 \cdot u_0$. Furthermore, the circulation approaches a value of $0.7 \cdot \Gamma_0$ as in the previous time instants suggesting that the changes related to this disturbance remain contained in the core region. Past $\tau = 3.9$ L- and R-vortex retain the similitude discussed. Since the second disturbance occurs when jet-like axial flow at the vortices prevails, the 2D3D results provide complementing insight.

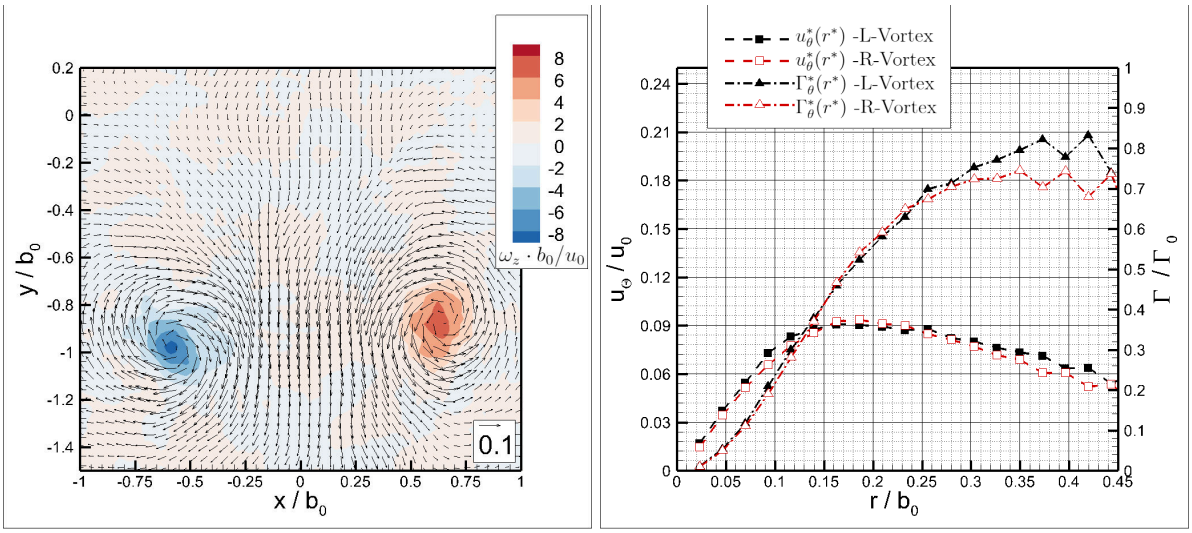

(a) Velocity field and vorticity.

(b) Tangential velocity and vortex circulation.

Figure 4.9: Wake vortex measured velocity and derived parameters for the L- and right R-vortex at $\tau = 3.9$ ($\alpha_L = 30°, Re_c = 125 \cdot 10^3$).

The consecutive series of events remains the same for the two higher Reynolds numbers measured. These events are axial vortex flow behaving like a wake (towards the wing), the first disturbance, and the switch from wake-like to jet-like axial flow. The corresponding results are condensed in plots for each Reynolds number.

For $Re_c = 150 \cdot 10^3$ Figure 4.10a, shows the swirl velocity profiles. The peak velocity at $\tau = 1.4$ is higher on the L-vortex than the R-vortex (older vortex range).

Likewise, in this case, the first disturbance is imminent on the L-vortex. After that, at $\tau = 2.7$, the R-vortex features the same characteristics, visible in the higher peak velocity compared to the L-vortex.

Furthermore, the radial position of peak velocity in the L-vortex displays a shifting away from the vortex center. This increase in core diameter indicates a slight expansion succeeding the first disturbance. Finally, the swirl velocity profiles equalize at a vortex age of $\tau = 3.4$.

The circulation profiles are shown in Figure 4.10b , as in the previous case, the circulation is enhanced prior to the first disturbance ($\tau = 1.4$ L-vortex). Here the circulation approaches a value close to $\Gamma = 0.8$, decreasing as the vortex matures. This observation regarding a decrease of the vortex circulation is also reported by De Gregorio and Ragni's [81]. Here a full-configuration aircraft model is used for PIV measurements in a towing tank. Despite using a different vortex generator and the different Reynolds number range, the results agree qualitatively. Burnham and Hallock [73] suggests that vortex decay is related to the viscous dissipative phenomenon of low Reynolds numbers.

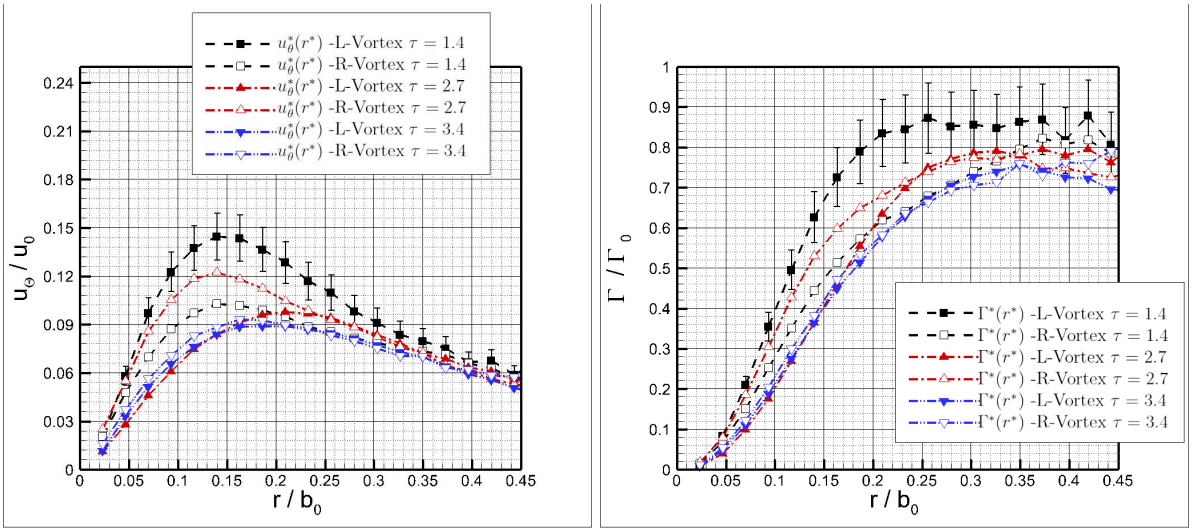

(a) Tangential velocity.

(b) Vortex circulation.

Figure 4.10: Wake vortex derived parameter from the wake- to jet-like axial flow ($\tau = 1.4$ to $\tau = 3.4$) for L- and R-vortex ($\alpha_L = 30°, Re_c = 150 \cdot 10^3$).

Figures 4.11a and 4.11b show the results of the $Re_c = 175 \cdot 10^3$, where the same characteristics are observed.

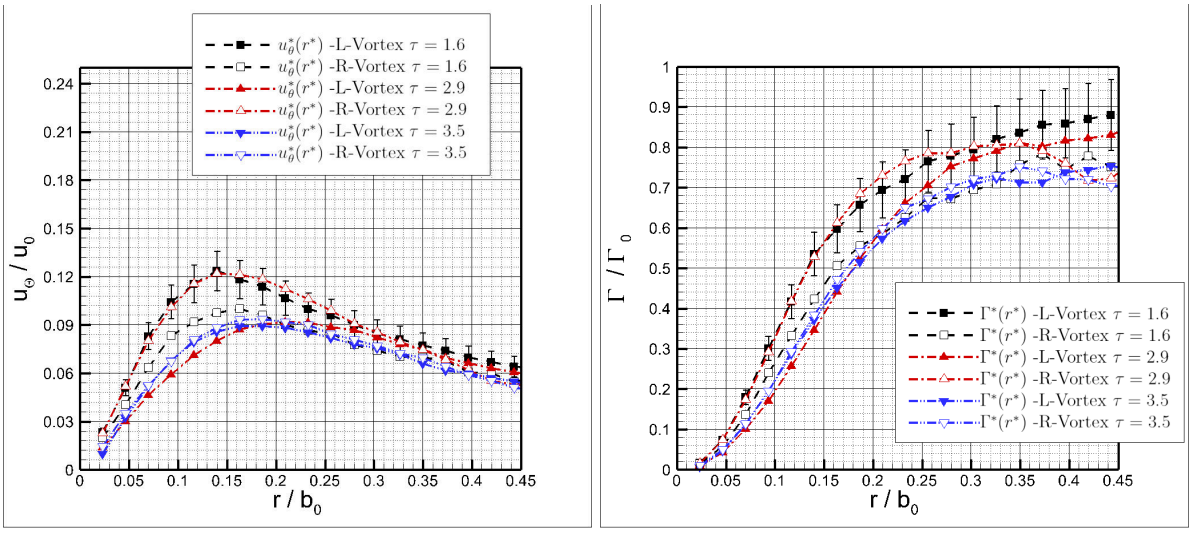

(a) Tangential velocity.

(b) Vortex circulation.

Figure 4.11: Wake vortex derived parameters from the wake- to jet-like axial flow ($\tau = 1.6$ to $\tau = 3.5$) for L- and R-vortex ($\alpha_L = 30°, Re_c = 175 \cdot 10^3$).

In conclusion, the 2D2C-PIV results can be summarized as follows:

- prior to the first disturbance, there is an increase in the swirl velocity in the vortex core region; likewise, there is an enhancement of the circulation rate of increase.
- After the first disturbance, the swirl velocity peaks at a lower value with a flattened radial profile. Consequently, the slope of the circulation decreases, and the vortex core radius increases.
- At later post-disturbance times, the swirl velocity and circulation profiles are almost identical, and the vortex core radius keeps its size.
- A decremental circulation (decay) over time is noticeable for all cases investigated.

4.3 2D3C PIV Measurement results and analysis

Since the disturbances primarily impact the axial vortex flow, a three-dimensional measurement technique is required. Hence 2D3C-PIV is used to measure the through-plane velocity (axial direction) and the in-plane swirl velocity (tangential velocity). The focus here is on the R-vortex solely and its temporal axial flow development along with the disturbances it sustains (first and second). The Reynolds number presented here reads $Re_c = 125 \cdot 10^3$ achieved with the same trajectory used for the 2D2C-PIV measurements.

The arrangement of the measurement components and positioning of the wing (submersion depth and sidewall distance) differs due to the given characteristics of the measurement system. These characteristics are the cameras' range of operation (distance) and the maximum submersion deep of the torpedo that houses the cameras, as shown in Figure 2.5 with the corresponding case-3 in Table 2.1). This measurement configuration is in line with the geometric characteristics of the vortex, i.e., there is no superposition of swirl and axial velocity components caused by a tilt light sheet, as is the case in the 2D2C measurements. Furthermore, the flow is seeded with a mixture of Vestosint and GHS. For this Reynolds number, the Vestosint particles follow the vortex flow region beyond the core, and GHS accumulates in the vortex core center line. Because the GHS have a constant diameter and are almost buoyancy neutral, an accurate measure of the axial flow can be realized. The vortices descending movement is suppressed in the velocity field analysis by setting the origin of the coordinate system at the detected found vortex center.

Furthermore, the spatial coordinates are normalized by the initial vortex spacing parameter b_0 and the velocity by u_0. Finally, for convenience, the wings moving direction is assigned with the negative z-direction with origin at the light sheet (see Figure 2.5). In line with this selected convention, axial flow behaving like a wake (following the wing) is negative; otherwise, jet-like axial flow is positive. Shown in Figures 4.12a to 4.15b are the three-component velocity fields spanning the time interval (given in vortex age) that begins after the wing crosses the light sheet and ends beyond the second disturbance. For reference, note that the wing's movement is terminated about three seconds after the deceleration starts (8·b ahead of the light sheet), equivalent to a distance of six meters.

As soon as the wing crosses the light sheet (about two double-frame images), the vortex age parameter is set to zero $\tau = 0$. At $\tau = 1.8$ (Figure 4.12a), the vortex features the smallest core size and highest magnitude of axial flow velocity (wake-like), which reads around $u_z/u_0 = -0.18$. By inspecting the vortex center, it can be observed that the axial velocity decreases with an increasing radius. Also, at a radius of about $r/b_0 = 0.025 - 0.05$, the axial velocity approaches zero. Between the vortex center and the radial location of almost no axial flow, a ring-like region forms with $u_z/u_0 = -0.04$. The interface between the different axial flow magnitudes is visible in the color coding transition from dark blue to orange. Later on, at $\tau = 1.9$, the wake-like axial flow in the core region decreases, as shown in Figure 4.12b. Furthermore, the annular-like domain around the center displays an increase while the axial velocity magnitude remains nearly unchanged $u_z/u_0 = -0.04$.

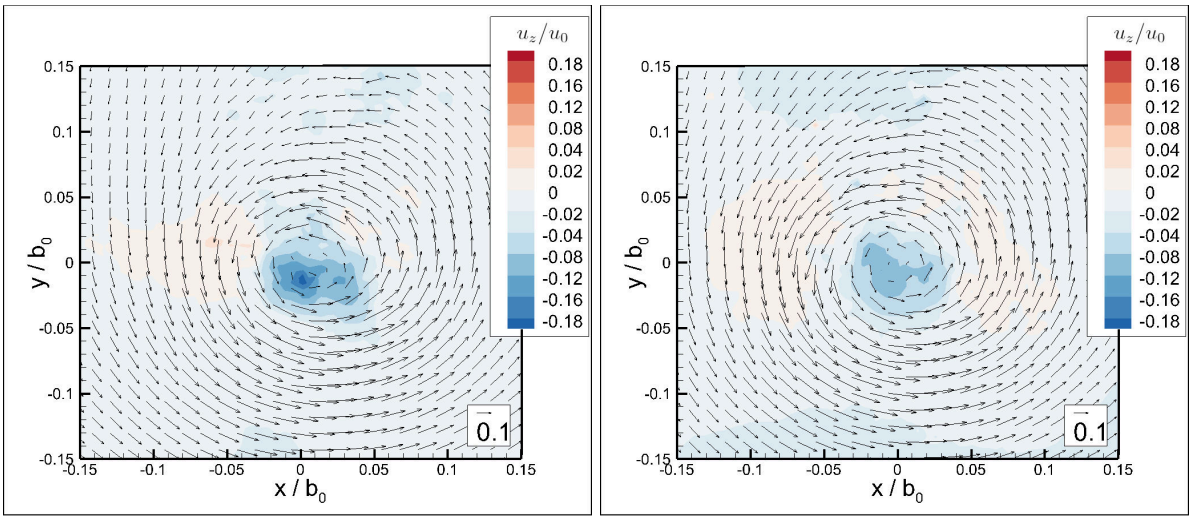

(a) Velocity field at $\tau = 1.8$ with substantial wake-like axial flow (towards the wing).

(b) Velocity field at $\tau = 1.9$ with reduced magnitude of the wake-like flow at $\tau = 1.9$.

Figure 4.12: Wake vortex velocity field featuring wake-like axial flow ($\tau = 1.8$ and $\tau = 1.9$) for the R-vortex ($Re_c = 125 \cdot 10^3$).

The rapid and notable change of the axial flow at this time is confined to the core domain. Nonetheless, at a time $\tau = 2.2$, the axial flow in the core almost decreases to zero, as indicated in Figure 4.13a . At the time $\tau = 2.5$ (See Figure 4.13b), the axial flow direction is inverted(occurrence of the first disturbance and vortex bursting), and the domain of this conversion extends beyond the vortex core.

An additional conclusion can be derived from Figures 4.12a to 4.13b . A small area with positive axial flow past the core region (where the wake-like axial flow dominates) is notable in Figure 4.12a . This small area dilates gradually, alters its location, and translates towards the center of the vortex after the wake-like flow ceases at $\tau = 2.5$. This particular behavior hints at the collision of opposing axial flow currents, as pictorially shown in Figure 4.2 . Unfortunately, because of the limited temporal resolution of the measurement equipment, this characteristic can not be further investigated.

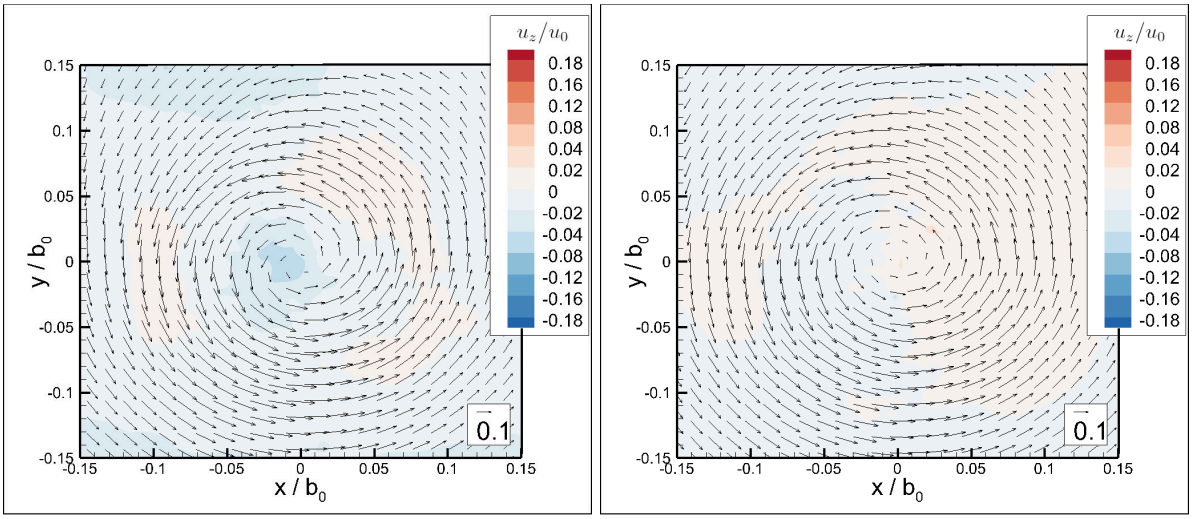

(a) Velocity field at $\tau = 2.2$, when the first disturbance occurs.

(b) Velocity field at $\tau = 2.5$, prevalence of jet-like axial flow post disturbance.

Figure 4.13: Velocity flow fields before and after the first disturbance ($\tau = 2.2$ and $\tau = 2.5$) for the R-vortex ($Re_c = 125 \cdot 10^3$).

At later times the jet-like axial flow prevails. This situation is depicted in Figures 4.14a to 4.15b ($\Delta\tau = 0.1$ prior to the second disturbance). Furthermore, there is a shell-like increase in velocity magnitude and vortex core diameter. The radial distribution of axial velocity is shown in Figures 4.16a [$Re_c = 125 \cdot 10^3$ (case-3)]. Most of these profiles are extracted from Figures 4.12a to 4.15b . The vertical axis corresponds to the mean velocity value in the azimuthal direction and the horizontal to the normalized radius. Here the vortex age range begins at $\tau = 0.8$ and ends at $\tau = 3.2$. The complete evolution of the axial flow (containing the switch of the flow direction and the disturbances) is inside this range.

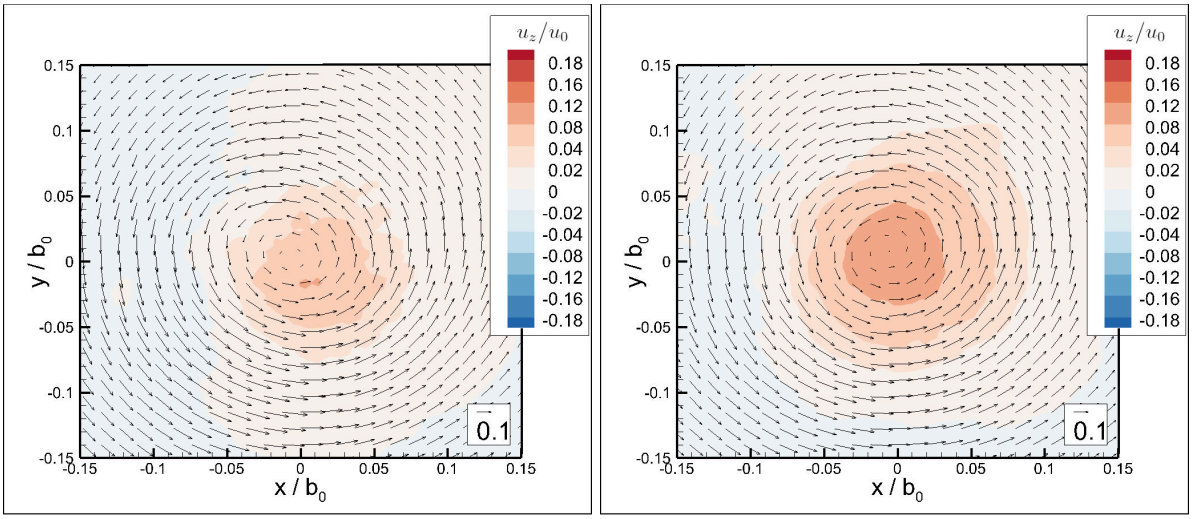

(a) Velocity field at $\tau = 2.6$, with pronounced axial symetry.

(b) Velocity field at $\tau = 2.7$, with incresing vortex core and axial velocity.

Figure 4.14: Wake vortex velocity with only jet-like axial flow ($\tau = 2.6$ and $\tau = 2.7$) for R-vortex ($Re_c = 125 \cdot 10^3$).

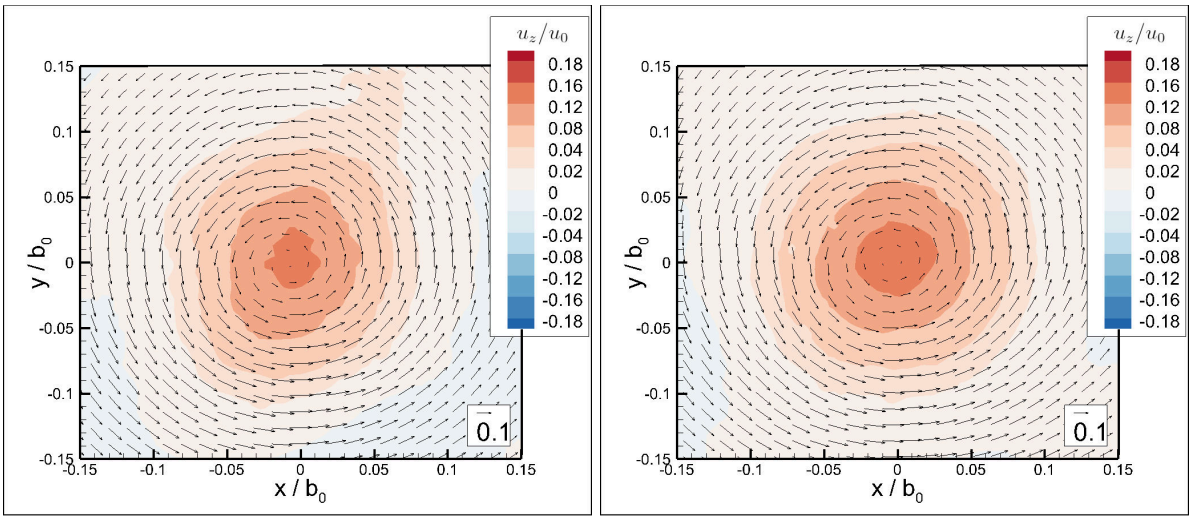

(a) Velocity field at $\tau = 2.8$.

(b) Velocity field at $\tau = 3.0$.

Figure 4.15: Wake vortex velocity field featuring wake-like axial flow ($\tau = 2.8$ and $\tau = 3.0$) for R-vortex ($Re_c = 125 \cdot 10^3$).

Prior to the first disturbance, minor differences in the axial velocity are shown (note that the averaging removes most of the measurement noise, and comparing the curves refers to the average values).

The differences observed are assumed to be related to the unsteadiness of the wake flow in the near-field. Nevertheless, the axial velocity peaks asymptotically at the vortex center, and the core region can be interpreted as undergoing a contraction up to $\tau = 1.9$. Surrounding the severe negative axial flow at the vortex center, a region of zero velocity can be observed ($r/b = 0.03 - 0.09$). Beyond that region, it follows another region with negligible but still negative axial flow. There is a time-decreasing trend from $u_z/u_0 = 0$ to $u_z/u_0 = -0.025$ up to $\tau = 2.2$. At times $\tau = 2.2$ and $\tau = 2.5$, there is a switch in the vortex flow direction at the vortex center (related to the first disturbance). The positive axial flow (jet-like) spreads radially from the vortex center and prevails in the core. The positive axial flow (jet-like) builds up to $\tau = 3.1$, where the velocity peaks at around $u_z/u_0 = 0.16$, and the second disturbance occurs (Figure 4.4).

Furthermore, the vortex core with positive axial flow increases beyond its previous counterpart (wake-like) flow. At a time $\tau = 3.2$, the jet-like axial flow maxima drop to about $0.12 \cdot u_0$, related to ensuing a gradual vortex decay. In the raw data, the seeding particles leave the core at this point, and the boundary is diffused. The radial profiles of swirl velocity that match Figure 4.16a are shown in Figure 4.16b . Up to the time $\tau = 1.9$, the maximum swirl velocity moves towards the vortex center (contraction), while at the same time, the maxima itself increases. After the switch in axial flow from wake-like to jet-like occurs, the vortex core expands again (peak velocity moves to a higher radius). Finally, the core expansion proceeds, and the swirl velocity's peak flattens, as is the case for the 2D2C results, without the noticeable influence of the second disturbance (contrary to the axial velocity profiles).

In order to further check the validity of the measurement data, a radial flow analysis was conducted. Since there is a vortex pair and each vortex sits in the flow field of the other, the data is not as smooth as in the case of a single vortex. The radial velocity profiles of the horizontal cross-section are used to eliminate the influence of the adjacent vortex on the radial velocity. The results are plotted in Figure 4.17a. Focusing first in the plot corresponding to $\tau = 0.8$: This instant is close to the roll-up region. Transient behavior is to be expected since this is not the far-field. Nevertheless, the radial velocity distribution compares very well to the literature, e.g., Aboelkassem [82], Fig. 1, or Bhagwat and Leishman [83], Fig. 11.

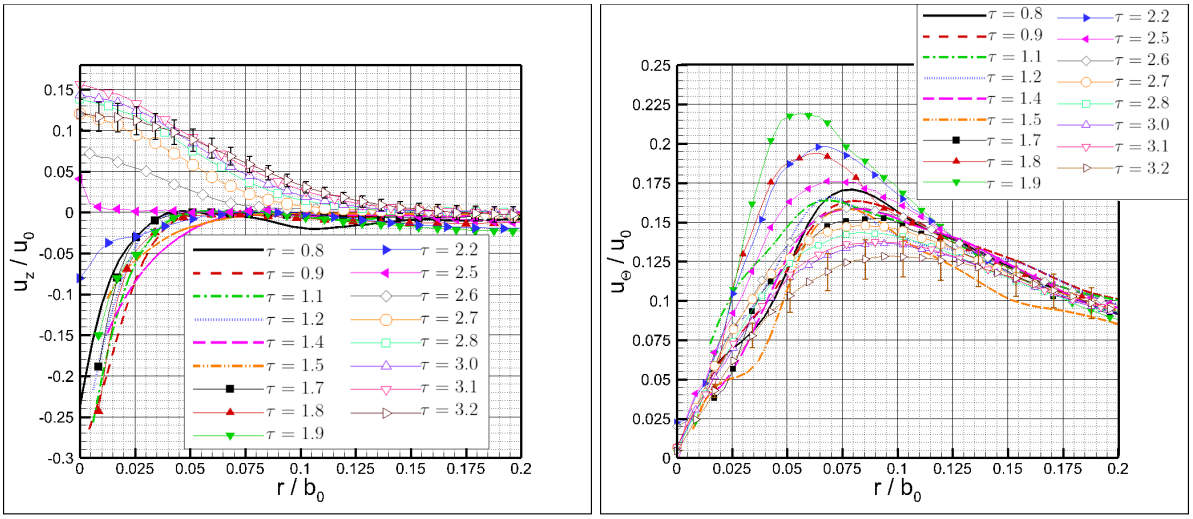

(a) Axial velocity radial profile.

(b) Swirl velocity radial profile.

Figure 4.16: Azimuthal average radial distribution of axial and swirl flow velocity for $Re_c = 125 \cdot 10^3$.

Three radii locations are arbitrarily chosen to quantify (in an estimated sense) the vortex core expansion in terms of the radial velocity change over time. These are $r_1 = 0.05 \cdot b_0$, $r_2 = 0.06 \cdot b_0$ and$r_3 = 0.07 \cdot b_0$. Figure 4.17b shows the temporal development of the radial velocity (left vertical axis) at the selected radii locations. A trend can be recognized of increasing negative radial velocity beginning at around $\tau = 1$ until $\tau = 2.6$. This development is disturbed by a peak with a positive radial velocity between $\tau = 1.75$ and $\tau = 2$. This peak is assumed to be caused by the opposing wake-like and jet-like axial flow in the core of the vortex at the position where the direction of the axial flow switches (jet-like axial flow prevails).

This observation is in line with Fabre et al. [80] findings and, most importantly, with vortex bursting (localized superposition region of both effects). At $\tau = 2.2$, the first disturbance related to the vortex bursting is observed. At $\tau = 3.1$, the vortex experiences the second disturbance associated with the reconnection of the vortex (after stopping the wing) that triggers a helical instability. This diagram cannot totally explain the contraction under observation. The contraction happens on a shorter timescale than the slowly increasing negative radial velocity in Figures 4.17a and 4.17b (note that the velocity proves in Fig. 4.17b are chosen at arbitrarily radial locations and aimed to demonstrate the radial inflow/outflow of the disturbed vortex).

The flow's three-dimensional character (time-dependent) does not allow for finding a simple relation. Nevertheless, throughout the continued analysis of the experimental data, it is assumed that the contraction takes place and is not an artifact. Here one can only refer to several citations from the previous works [36], [34], [78], [38] that describe the simultaneous occurrence of a contraction and an expansion, just like in the present case, and leave a small amount of research for the future.

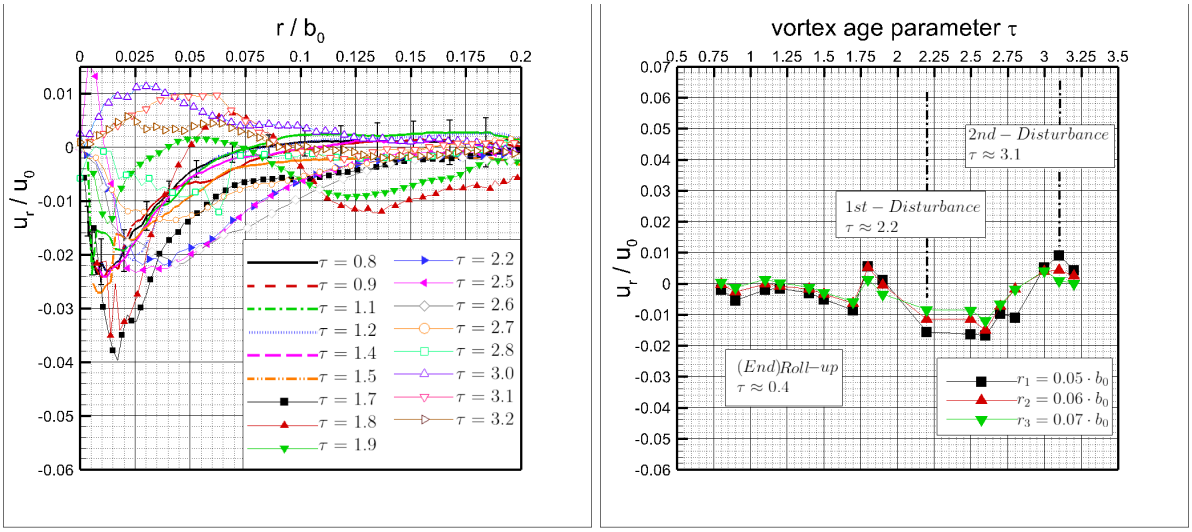

(a) Radial velocity profile of the vortex horizontal cross section.

(b) Time development of the radial velocity with a label of relevant vortex events.

Figure 4.17: Radial velocity and the corresponding mass flow rate at $Re_c = 125 \cdot 10^3$.

Qualitatively in line with the results, vortex axial flows exhibiting peaks at the center are also described by Singh et al. [33]. In addition, Singh et al. measured the wake vortex with a hot-wire technique in a wind tunnel at several axial (downstream) locations. They suggested their results as experimental proof of axial instability of helical type. Notably, they observed an excess in axial velocity behind the wings trailing edge that drops in the downstream direction (velocity deficit). Hence, with the terminology used, Singh et al. [33] first measured jet-like, followed by wake-like axial flow. A potential reason is that the quick axial speed change in the wake vortex near-field (rolling-up) demands a high acceleration of seeding particles. The likely strong but short-living and severe pressure gradients at the vortex core cannot reach this demand in the case of solid particles.

Nevertheless, Ash and Khorrami [26] questioned these affirmations, arguing that the non-stationary characteristics in the mean flow were not considered. Likewise, the fluctuation of the upstream flow was not quantified. Because of the low resolution of PIV measurements, instabilities can not be studied in detail. Therefore the comparison remains qualitative.

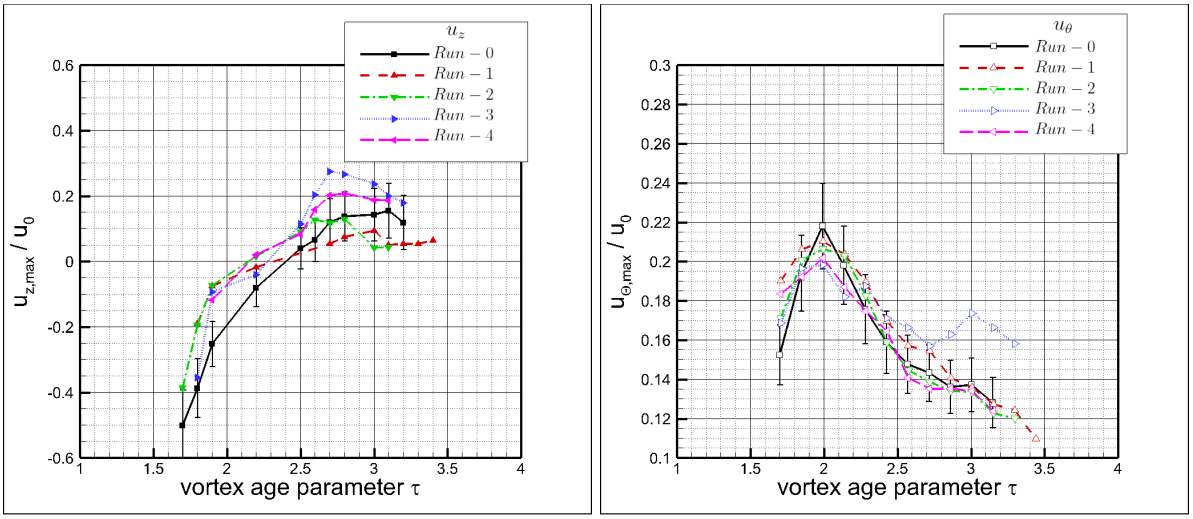

(a) Peak axial vortex flow (at the vortex center $r(u_{z,max})$) developing in time.

(b) Peak swirl vortex flow (at the radii $r(u_{\theta,max})$) developing in time.

Figure 4.18: Time development of axial velocity maxima and swirl velocity for five independent measurements run at $Re_c = 125 \cdot 10^3$.

In order to corroborate that the results and derived observations are consistent (in independent measurements for $Re_c = 125 \cdot 10^3$), four repetition runs were carried out. Figure 4.18a shows the time development (in vortex ages) of the peak axial velocity for the total five runs. Here the general similarity of the profiles is evident. However, there is minor variation in peak magnitudes, rates of increase/decrease, and time occurrence. These variations are expected since, as mentioned before, the vortices have nonlinear properties, and unavoidable towing tank variations (ambient temperature, lingering turbulence, seeding quality, among others) make every run unique. Furthermore (Figure 4.18a), the axial flow features initially severe wake-like axial flow (negative velocity) that reduces towards zero as time increases. The time the axial flow changes from wake-like to jet-like (crossing zero at about $\tau = 2.2$ to $\tau = 2.5$) corresponds to the time the first disturbance is observed in the raw data.

Afterward, the axial flow steadily becomes positive. Finally, the jet-like axial flow reaches a peak value with a time corresponding to the occurrence of the second disturbance. Beyond this time, the particles trapped in the vortex core are released, hindering an accurate localized measurement of the axial velocity at the center. Nevertheless, there is a smooth decrease in the positive axial velocity in the core region. Figure 4.18b shows the time development of the peak in swirl velocity. Before the first disturbance, the peak velocity increased (at about $\tau = 2.0$) due to the previously discussed contraction for all runs.

An enhancement in the tangential velocity and the related contraction is the outcome of the conservation of angular momentum. Because the axial flow behaves like a wake in the beginning, there is an inflow from outside to the core (radial-in). This inflow enforces an acceleration in the swirl velocity contracting the vortex (angular momentum is conserved). Then, right after the contraction, there is an expansion of the vortex, where the analysis of conservation of momentum applies but with flow in the opposite direction (same rate of change). Finally, the swirl velocity decreases steadily at times up to $\tau = 2.7$ for almost all cases. This change in decrease rate coincides with the time the maximum axial velocity is reached before the second disturbance.

4.4 Estimation of velocity and origin of disturbances

To estimate the propagation velocity of the first and second disturbances, the 2D2C PIV data is used. Here the whole data range, i.e., three Reynolds numbers measured ($Re_c = 125 \cdot 10^3, 150 \cdot 10^3$ and $175 \cdot 10^3$) is used along with the three positions where the deceleration begins ($0\cdot$,$4\cdot$ and $8\cdot$)b. The analysis is carried out for the tilted case light-sheet [$\alpha_L = 30°$ (case-1)] that implies an offset distance from the start of deceleration to FOV of $\Delta z_{[tilt]}$ (2.5 m [model placed in the middle of the tank] $\times \tan 30°$). Consequently, the total distance of the start of deceleration to the FOV reads for the individual case ($0 \cdot b$, $4 \cdot b$ and $8 \cdot b$) plus $\Delta z_{[tilt]}$ (2.5 m $\times \tan 30°$) as shown in Figure 2.7. The following analysis is carried out with dimensional parameters for easy comprehension. The first method for estimating the velocity is based on the time offset between the occurrence of a disturbance (L-vortex only) in the FOV when shifting the start of the deceleration. The time offset corresponds to the interval that starts when the wing is at the FOV and ends when the particular disturbance reaches the FOV.

To further facilitate the understanding, the different positions where the deceleration begins are coded with a symbol (square - 0·b, pentagon - 4·b, star - 8·b) in Figures 2.7 and in Figure 4.19a. Also, the horizontal axis is given the parameter z_d, and when the deceleration begins, it takes the value $z_d = 0$. This convention enforces a shift of the trajectories while the model decelerates along with the axial position of the FOVs resulting in virtually three light sheets coexisting (when plotted together). Accordingly, the coding symbols (Figure 2.7) collapse together in Figure 4.19a, where additionally the model trajectory and disturbances (estimated time and position) are plotted. Here the estimated average standard deviation for the time reads 30%.

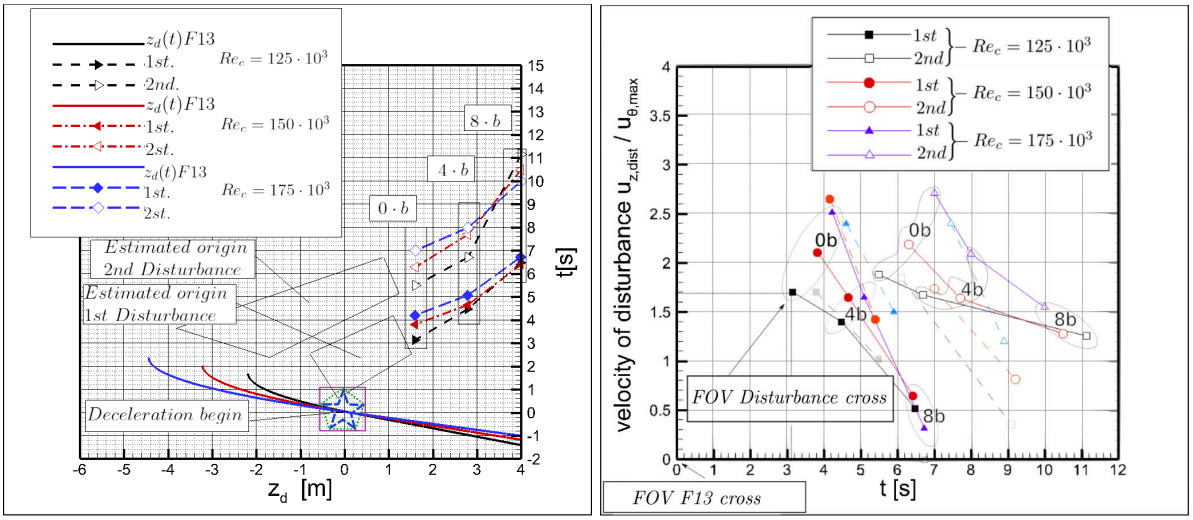

(a) Wing position as a function of time for deceleration trajectories and disturbance time and position of the left vortex.

(b) Estimated velocity of disturbances.

Figure 4.19: Disturbances position and propagation velocity and dependence of Reynolds number.

The following conclusions are offered by carefully inspecting Figure 4.19a .

- The disturbances decelerate as they propagate in the vortex core.
- By extrapolating the plotted points, it is possible to estimate the origin of the disturbance in time-space.
- The first disturbance arises shortly after the beginning of deceleration and takes some time to develop.

- The second disturbance arises after the wing comes to rest and the vortex reconnection takes place.
- The velocity of the disturbances scales with the Reynolds number.
- The second disturbance decelerates faster for low Reynolds numbers than the first disturbance.

Helical axial instabilities are reported by Lonfils et al. [39], Nybelen, Boussuge [38] and Moet et al. [34] in relation with vortex reconnection. Their CFD results corroborate the experimental results, particularly the observations after the wing comes to rest, i.e., vortex reconnection, subsequently, the second disturbance with helical-like topology. By extrapolating the time-space data of the first disturbance, its likely origin is located after the deceleration begins. This observation is in line with the mentioned references and the occurrence of bursting.

The second method for estimating disturbance propagation velocity is based on the time offset between the L- and R-vortex (assuming that the disturbances originate simultaneously and propagate with an identical speed). Here the offset in the axial distance (owed to the tilt of the light sheet) $\Delta z_{[LR]}$ is divided by the time interval that begins when the particular disturbance occurs in the L-vortex and ends when it occurs in the R-vortex $\Delta\tau_{[LR]}$. Applying this method to the raw data leads to Figure 4.19b displaying the propagation velocity estimation for the first and second disturbances at the corresponding position where the deceleration begins. For this method, the standard deviation reads, on average, about 30% for the time and 40% for velocity.

Figure 4.19b suggests the following:

- The propagation velocity of the disturbances (first and second) decreases as they progress.
- The propagation velocity scales with the Reynolds number.
- The propagation velocity suggests time convergence regardless of the Reynolds number.

Further deeper analysis of these findings and comparison to the literature are given in Castaneda Fuentes et al. [44].

5 Ground linking

5.1 Qualitative analysis of the vortices evolving close to the ground

Despite the simplified landing trajectory realized in the present experiments discussed in this section, several features previously described in the literature for large-scale aircraft experiments and CFD simulations are reproduced in the present setup. The following discussion begins with the FOV_{90° followed by the FOV_{45° and lastly, the FOV_{GP} when the wing comes to rest at a distance $h_{AG} = 1 \cdot c$. Here a sequence of averaged images (5 consecutive frames except the first one displaying the model at the FOV for reference) of selected time instances featuring general characteristics of the vortex and ground interaction is presented.

In Figure 5.1, three different snapshots of the vortex behavior at the FOV_{90° are shown. The tracing particles compose a path line (note that only for the visualization of the FOV_{90° microbubbles are added from the ground to make the vortex core visible and the roll-up). Additionally, for this case only, the camera was axially shifted 1 m away from the light sheet to capture the vortex pair and ensure they behave symmetrically. Furthermore, the image in Figure 5.1a is trimmed differently than the rest to highlight the model's position. Particularly for this case, it can be stated:

- The rapid rolling-up vortex system descends to the ground while fluid entrainment in the cores' vicinity increases.
- The oval enclosing the vortex pair increases in size due to the symmetric vortex core enlargement.
- The vortex core (visible through the line formation of particles traversing the FOV) displays the transition from wake- to jet-like axial flow.
- The vortices' symmetric descent follows a hyperbolic trajectory as predicted by the non-viscous theory.

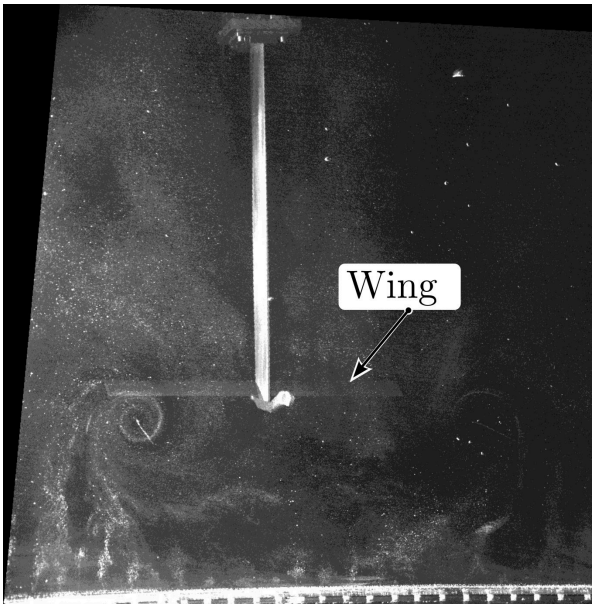

(a) Wing traversing the light sheet.

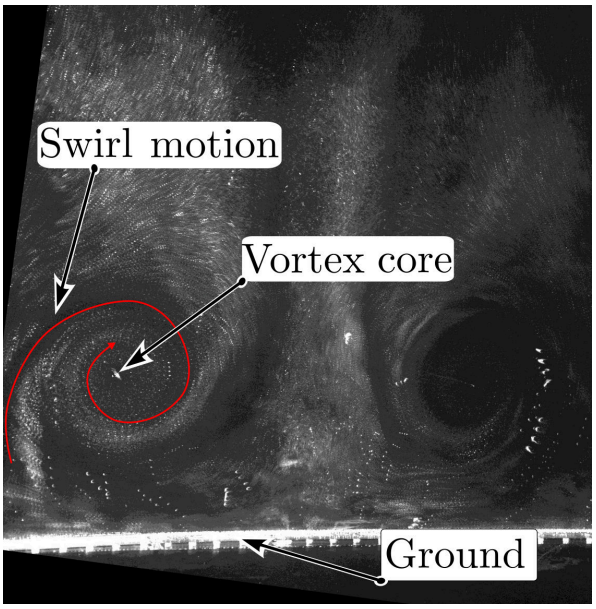

(b) Vortex age $\tau = 0.12$.

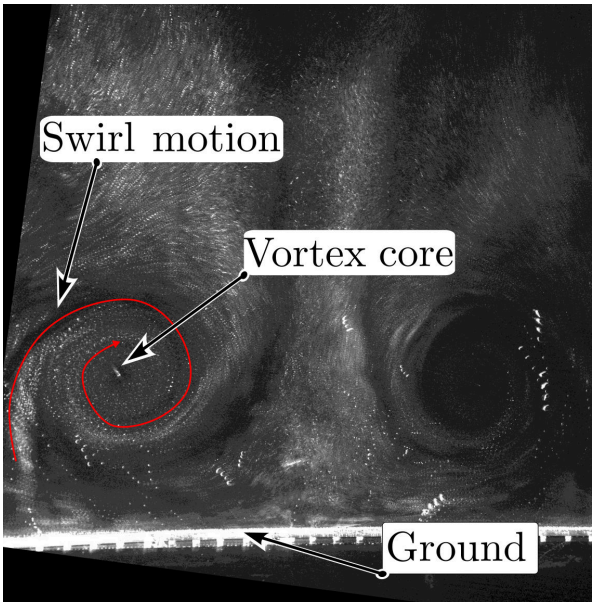

(c) Vortex age $\tau = 0.48$.

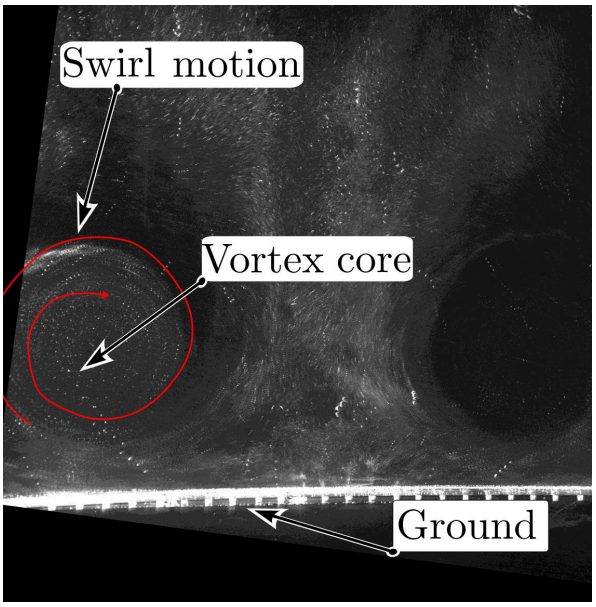

(d) Vortex age $\tau = 0.73$.

Figure 5.1: Visualization of time development of the wake vortex at FOV_{90°.

The following visualization corresponds to the tilt light sheet FOV_{45°. Shortly after, the model comes to rest, and the trajectory ends ($h_{AG} = 1 \cdot c$). Figure 5.2a shows for reference the wing at rest. Here the image was taken with background light to make the model visible, and the image was likewise trimmed slightly differently. After $\tau = 1.4$, vortex linking with the ground is observed.

However, the detachment of the wingtip vortices and the bound vortex from the wing before it links to the ground is not visible. The plausible reason is that in the time interval from the model halt $\tau = 0$ to $\tau = 1.4$, the region immediately behind the wing expels seeding particles instead of attracting them. The expelling of seeding particles is most likely due to the high centrifugal force exerted on the particles moving in the highly curved streamlines and the superimpose unsteadiness. This hypothesis is based on the analogy of centrifugal force produced by the axial disturbances due to the halt of the wing (end-effects presented in the previous chapter), where particles are released from the vortex cores. The observation of ground linking is depicted in Figure 5.2 for three successive instants in time.

Due to the tilted light sheet and the light ground reflection, the vortex core and the newly enclosed particles are visible. The blue guiding lines estimate the vortex core, and the red ones the swirl motion. One can note in Figure 5.2b severe vortex meandering [84], [85] and localized stretching. These topology changes converge rapidly toward a wavy vortex core structure and smoother circular swirl motion (Figure 5.2c and Figure 5.2d). The vortex structure quickly readjusts, which prevents decay caused by the vorticity of opposite sign from stretching, meandering, and creating structures in the azimuth plane. [37]. Additionally, due to the hyperbolic vortex trajectory, L- and R- vortices diverge apart, inhibiting the vorticity exchange across the vortex pair symmetry plane [86].

In general, for this case, the following is recognized as the vortices evolve:

- The vortex exhibits deformation (meandering and stretching) of the core that reduces as the vortex ages.
- The axial symmetry of the vortex increases with time.
- As the vortex ages, the axial velocity increases, evident in the higher concentration of seeding particles.

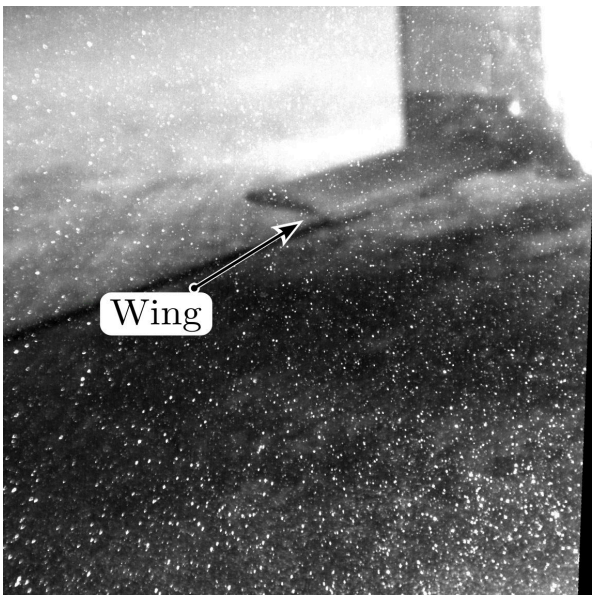

(a) Vortex age $\tau = 0$.

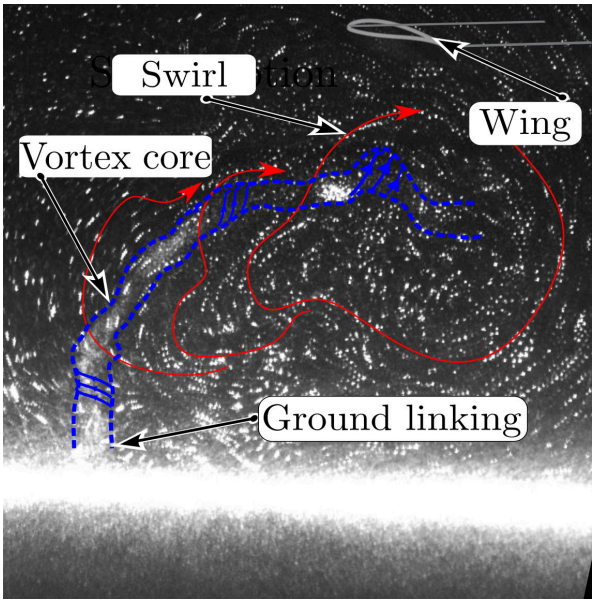

(b) Vortex age $\tau = 1.4$.

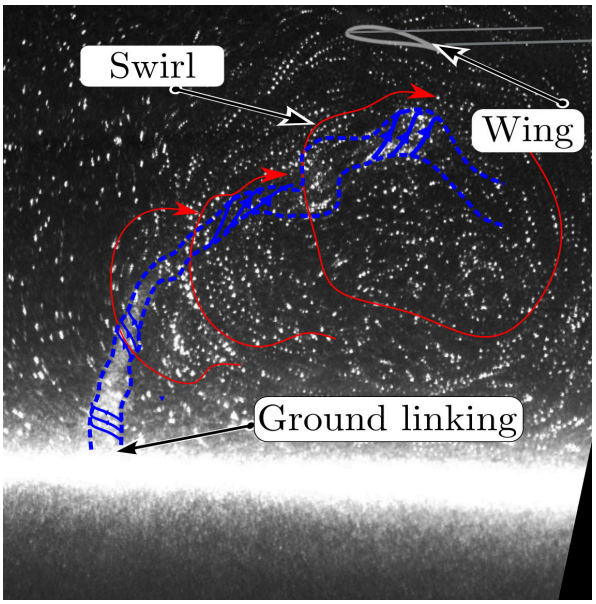

(c) Vortex age $\tau = 2.3$.

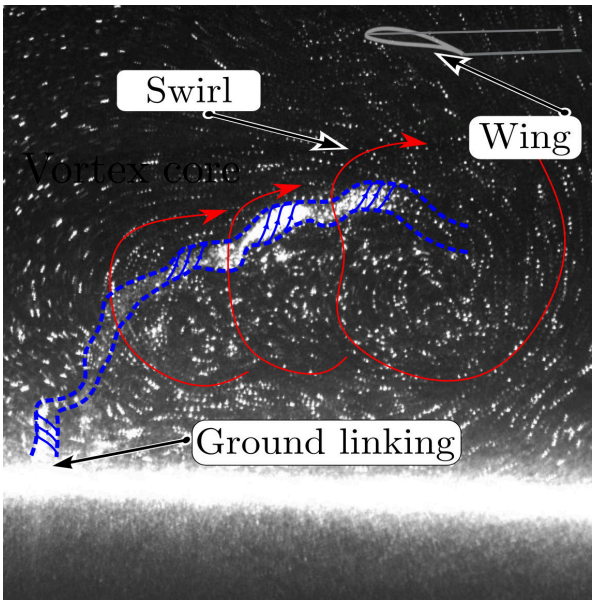

(d) Vortex age $\tau = 3.6$.

Figure 5.2: Visualization of time development of the wake vortex at FOV_{45°.

Lastly, the plane parallel to the ground FOV_{GP} is discussed (Figure 5.6). Once again, Figure 5.3a is shown for reference right before the wing comes to rest and the successive figures show the average of 5 successive images. Figure 5.3b shows the vortex ground linking location (at the center of the Figure), which takes place at about $\tau = 1.6$ vortex ages.

This scenario corresponds to the wedge vortex linking analyzed in the following subsection. For reference, the wing's rest position is overlaid (upper right corner of the Figures). The vortex swirl velocity induces a strong vorticity ground layer in the wake of the vortex (departing from the linking location). Judging by the observed path lines, the vorticity at the ground tends to form a cluster pattern (red lines in the vortex wake Figure 5.3b and 5.3c as also reported by Schlegel et al., [87]. Figure 5.3d shows the vortex state at time $\tau = 4.5$.

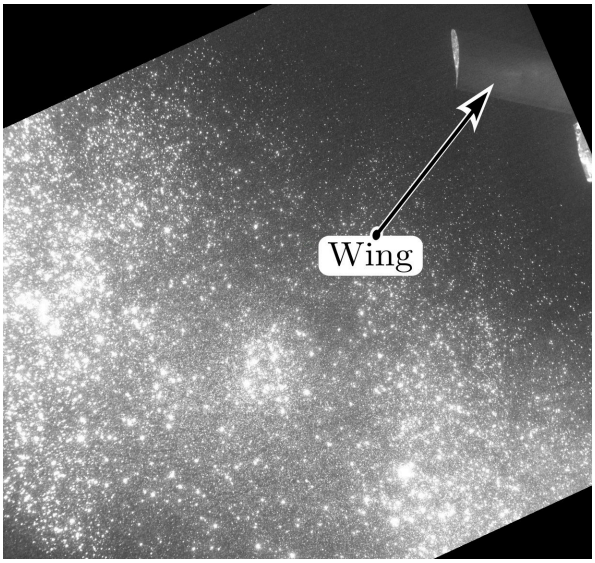

(a) Wing shortly before reaching terminal rest position.

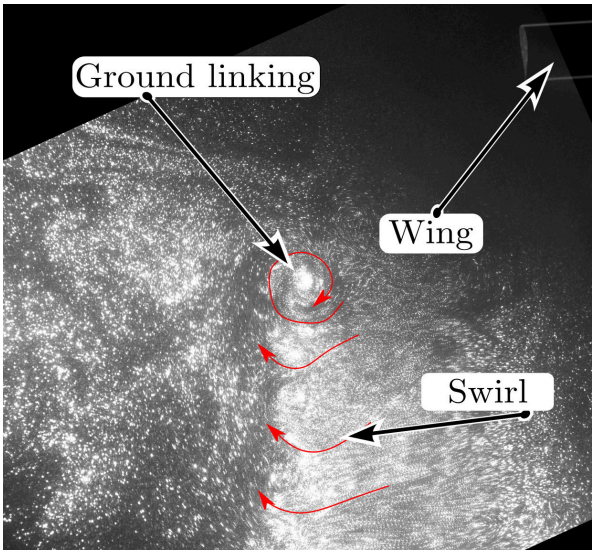

(b) Vortex age $\tau = 1.6$.

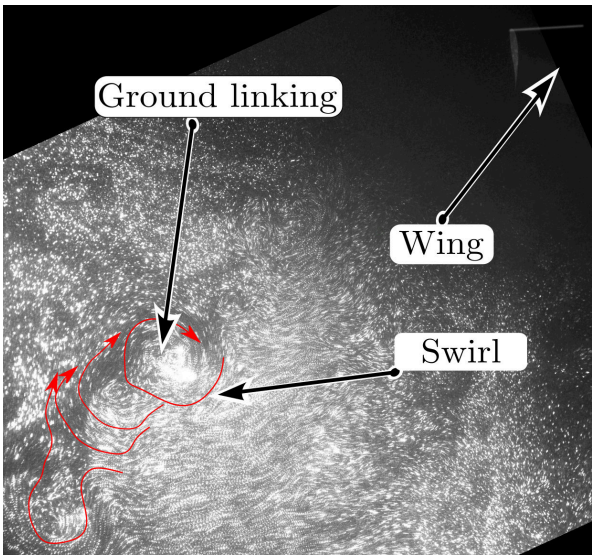

(c) Vortex age $\tau = 3.1$.

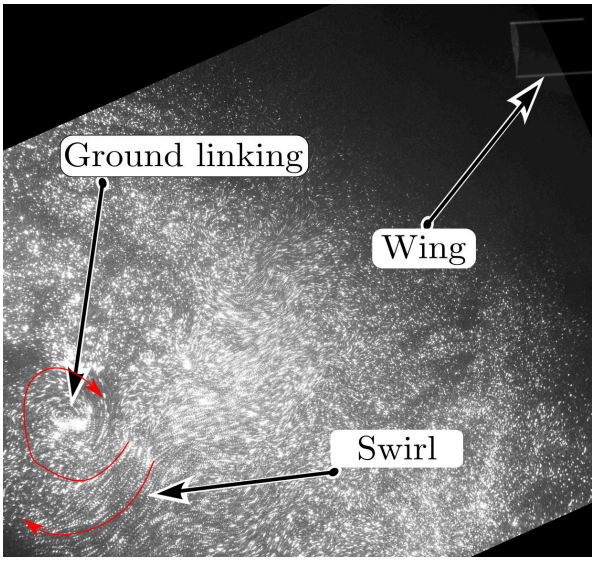

(d) Vortex age $\tau = 4.5$.

Figure 5.3: Visualization of time development of the wake vortex at FOV_{GP} and Height above the ground $h_{AG} = 1 \cdot c$.

Besides the lateral and retroceding drift of the linked vortex, the following observations are summarized:

- The vortex at the ground linking location loses coherence and increases in size.
- The vorticity cluster in the wake concentrates and rolls towards the linked vortex.
- The vortex's shape pivots around the linking spot, causing it to bend.

Despite the limiting view due to the vortex moving out of the FOV, the vorticity cluster seems to merge into one (Figure 5.3d). This final merging stage agrees with the coalescence of corotating vortices described by Meunier et al. [88].

5.1.1 Ground linking types

The evolution of vortices follows two distinct patterns based on the terminal height above the ground. These patterns can be best observed by comparing two extreme scenarios: when the wing comes to rest at a height of one chord length above the ground and when it comes to rest at a height of six times the chord length (which is equivalent to one spanwise length). The discussion starts with the case shown in Figure 5.4. Once the wing completes its trajectory, the vortices still are rolling up along with the short-living stopping vortex detaching from the wing's trailing edge and connect to the ground at their free ends. This linking happens rapidly, and because of the vicinity to the ground, the vortices form a wedge angle when attached to it, as displayed in Figure 5.4a. As the linked vortices evolve, they interact more with the ground, resulting in a vortex reshaping as shown in Figure 5.4b. Here the linked vortices develop an upright position on the ground. As a result, the vortex is parallel to the ground where it is linked. However, it bends like an elbow in the direction of the vortex wake, causing the vortex cross-section to be perpendicular to the ground.

The second extreme case is shown in Figure 5.5. Once the wing completes its trajectory and reaches a distance from the ground equal to its spanwise length (300 mm), the L- and R-vortex detaching from the wingtips along with the stopping vortex merge to form a horseshoe vortex, as illustrated in Figure 5.5a. The horseshoe vortex maintains its closed structure and has minimal interaction with the ground at first.

As it approaches the ground, it experiences a rebound that helps it to maintain its height. However, as it ages, it begins to interact more with the ground, causing it to elongate at the front corners and form a shoulder-like shape. Eventually, the horseshoe vortex breaks apart, and the remaining parts connect with the ground, resulting in multiple vortex linking. This behavior is illustrated in Figure 5.5b. The time frame for these events is much longer than the previous sequence of the quick ground connection at a lower height.

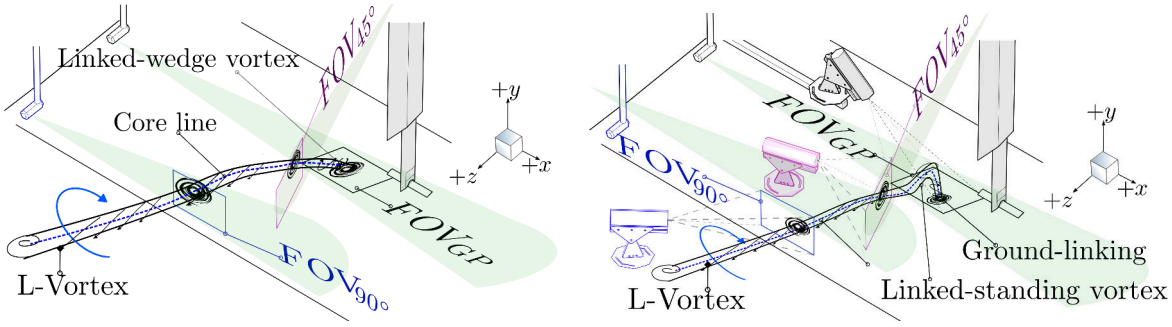

(a) Linked-wedge vortex at an early age.

(b) Linked-standing vortex at a mature age.

Figure 5.4: Vortex ground linking and corresponding cross section in the FOV_{GP}, $FOV_{45°}$ and $FOV_{90°}$ when $h_{AG} = 1 \cdot c$.

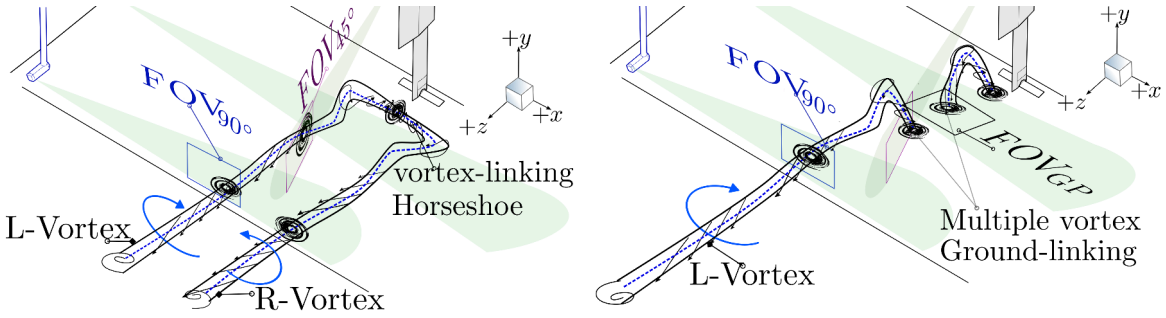

(a) Horseshoe vortex at an early age.

(b) Multiple vortex linking at a mature age.

Figure 5.5: Vortex ground linking and corresponding cross section in the FOV_{GP}, $FOV_{45°}$ and $FOV_{90°}$ when $h_{AG} = 6 \cdot c$.

5.1.2 Visualization of ground linking types

Flow visualizations are included to explain the different ground linking types further. The first type, wedge vortex linking, is depicted in Figure 5.6a (which shows the average of 5 consecutive frames). In this type of linking, the vortex body near the ground creates a vorticity front (represented by red arrows) as it departs from the linking location. As a result, the wake of the vortex appears clustered, indicating a wavy deformation. This situation causes some parts of the vortex to be closer to the ground and substantially impacts the induced vorticity layer(the red arrows enclose these parts), as previously described. The development of the linked vortex (average of 20 consecutive frames) is depicted in Figure 5.6b.

The field of view is adjusted to account for the vortex's lateral and axial drift such that the linked vortex appears in the center of the image without the wing being visible. Furthermore, at this time, the vortex appears upward or oblique to the ground. In the image shown in Figure 5.6c, which is an average of 10 consecutive frames, the second type of ground linking is seen. This scenario occurs when the wing reaches a height above the ground that equals one spanwise length. In this type of linking, the wingtip vortices detach from both the left and right tips, and a weakly shed bound (stoping) vortex links them together to form a horseshoe shape. The slow-developing ground velocity shows the footprint of this horseshoe vortex.

In Figure 5.6c, the vortex can be seen by the swirl representing red lines. It bends towards the location where the L- and R-vortex meet, and there are fewer particles in that area. This condition suggests that the vortex is lifted off at that site. As the vortex moves beyond the curve, it gets closer to the ground and accelerates the ground velocity layer. The horseshoe vortex breaks into several parts in Figure 5.6d (which shows an average of 40 consecutive frames). Three ground-linking locations can be seen to the left of the wing, with two of them confirming the closure of a single loop with the ground. The third location is the remaining part of the linked wake vortex, followed by a swirl velocity front.

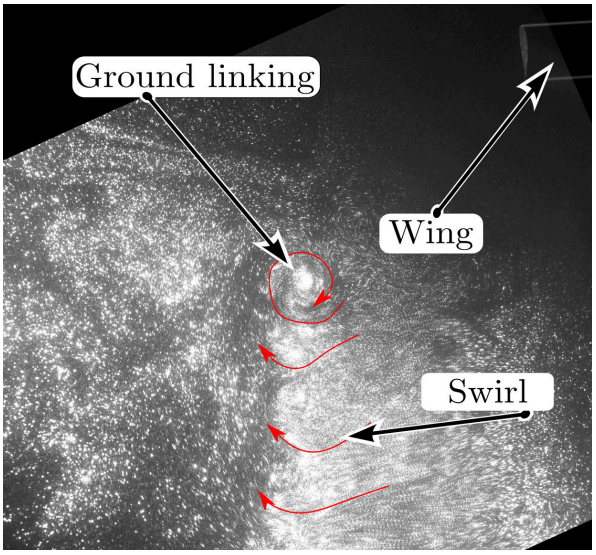

(a) Linked-wedge vortex $h_{AG} = 1 \cdot c$ and $\tau = 1.6$.

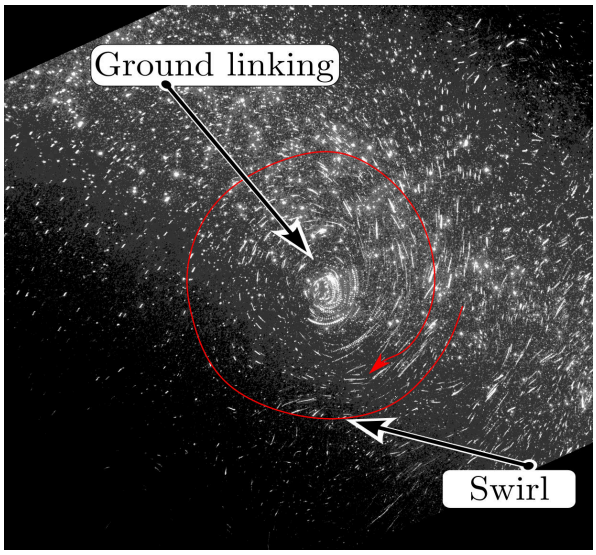

(b) Linked-standing vortex $h_{AG} = 1 \cdot c$ and $\tau = 7.3$.

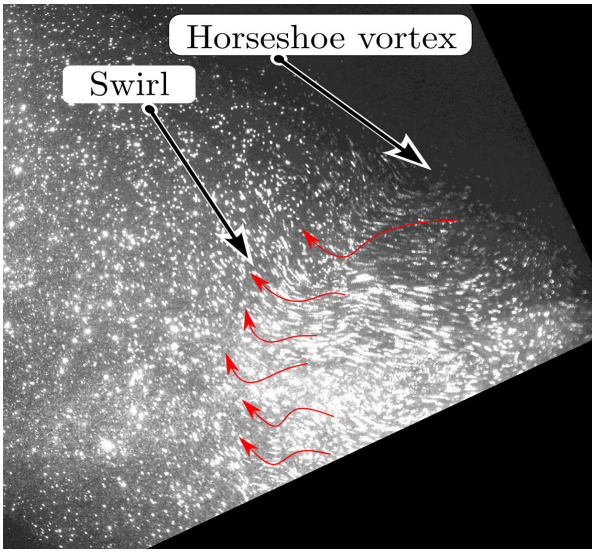

(c) Horseshoe vortex $h_{AG} = 6 \cdot c$ and $\tau = 6.3$.

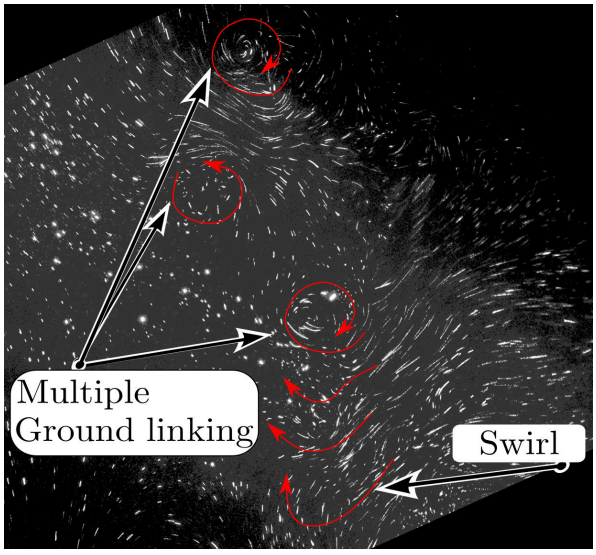

(d) Multiple vortex linking $h_{AG} = 6 \cdot c$ and $\tau = 12.7$.

Figure 5.6: Visualization of the ground linking types and time development of the wake vortex at FOV_{GP}.

5.2 Experimental findings using PIV

To discuss the results, the analysis is divided into two parts. The first part outlines the findings when the terminal height above the ground is changed while maintaining the same steady velocity and deceleration. Here an analysis of the two types of ground linking and their unique characteristics is carried out.

In the second part of the presented analysis, the wing's deceleration is doubled and halved while keeping a steady velocity before entering the circular trajectory segment and the terminal height above the ground constant. Only one parameter at a time for each experiment sequence is changed. The results of the experiment are presented in a consistent manner for each case. First, the PIV results of the cross-tank section $FOV_{90°}$ will be discussed. Next, the results of the tilted $FOV_{45°}$ will be covered, and lastly, the light sheet arrangements parallel to the ground (FOV_{GP}) will be discussed. Secondly, the time development of the center position and vortex circulation in the same FOV order are shown.

5.3 Results: changing the height above the ground

To substantiate the relevant findings, the results of the two different cases that show distinguishing vortex behavior are presented: $h_{AG} = 1 \cdot c$ (50 mm) and $h_{AG} = 6 \cdot c$ (300 mm). In the former, vortex ground linking is the distinguishing factor, while in the latter, L- and R-vortex linking (horseshoe vortex) is followed by multiple vortex ground linking. Therefore, the analysis of the results will focus on these two events. In the subsequent subsection, the information on the vortex evolution of the three different measurement planes is put together.

This analysis allows for the reconstruction of the structure of the vortex and its main parameters, including circulation and vortex core trajectory. The drifting and rebound are also discussed using the center locations' footprint. For all the investigated cases, the vortex age parameter is set to zero ($\tau = 0$) at the moment the wing comes to rest. In the velocity fields, the coordinates x/b_0, y/b_0 and z/b_0 are set to zero at the point in the FOV, where the crossing wingtip sheds the vortex. The coordinates of the vortex center are labeled x_c/b_0, y_c/b_0 and z_c/b_0 and move together with the vortex as it evolves. Therefore, in the velocity field discussion, the vortex distance to the ground (given in vortex center coordinates) assumes positive values.

5.3.1 End of trajectory at $h_{AG} = 1 \cdot c$ (50 mm) distance to ground

Wake vortex evolving in ground proximity at cross-section plane $FOV_{90°}$ and $h_{AG} = 1 \cdot c$

Beginning with the case where the model ends its trajectory closest to the ground $h_{AG} = 1 \cdot c$ (50 mm), the following events are described. First, at a vortex age of $\tau = 2.3$ (Figure 5.7a), the vortex is entirely inside the FOV. Here the substantial swirl velocity in the horizontal range $x/b_0 \approx -0.5$ to $x/b_0 \approx -1$ is driven by the remaining roll-up process of the vortex [89]. Consequently, flow entrainment from the undisturbed lateral region beyond $x/b_0 \approx -1$ (radial inflow from left to right) is enforced by the resulting pressure gradients. The radial inflow imposes an asymmetric stretching of the vortex and, an open ring-like distribution of vorticity of $\omega_x \cdot b_0/u_0 \approx -0.5$. As a result, the vortex core shows significant deformation.

At this time, the vortex is closest to the ground ($y_c/b_0 \approx 0.2$), hinting at an early vorticity layer development, with negligible opposite signed vorticity lifting the vortex. Later, at $\tau = 2.9$ in Figure 5.7b, the velocity distribution in the azimuthal direction is symmetric, and the vortex core is almost undeformed. Here the vortex begins to lift up, with a distance of $y_c/b_0 \approx 0.35$ to the ground due to the vorticity layer's thickening. The vortex strength gradually decreases while simultaneously holding symmetry at a time $\tau = 3.4$ (Figure 5.7c), lateral drifting is present, and the distance to the ground is slightly above $y_c/b_0 = 0.4$. Finally, at $\tau = 3.8$ in Figure 5.7d, the vortex core shows a horizontal elongation due to meandering and stretching [1], [90]. At this time, the induced vorticity layer at the ground is strong enough to cause severe vortex rebound [91]. Thus, the vortex center reaches a height of $y_c/b_0 \approx 0.5$.

The corresponding tangential (swirl) velocity is computed and plotted for these and more time instances in Figure 5.8a. Here at $\tau = 2.3$, the swirl velocity peaks at a value of $u_\theta/u_0 \approx 0.18$. The previously described vortex core deformation due to the remaining roll-up is shown in the range $r/b_0 \approx 0.2$ to $r/b_0 \approx 0.4$. At $\tau = 2.9$, the vortex features almost ideal symmetry. Consequently, the swirl velocity distribution reaches a maximum slightly past $u_\theta/u_0 \approx 0.14$ and smoothly decreases in the radially outward direction. After that, core deformation is seen in the velocity fields as spotted at times $\tau = 3.4$ and $\tau = 3.8$. A transition from an undisturbed vortex can be assumed in the former, while the vortex stretches, featuring a multiple-peak distribution in the latter. Figure 5.8b shows the circulation profiles.

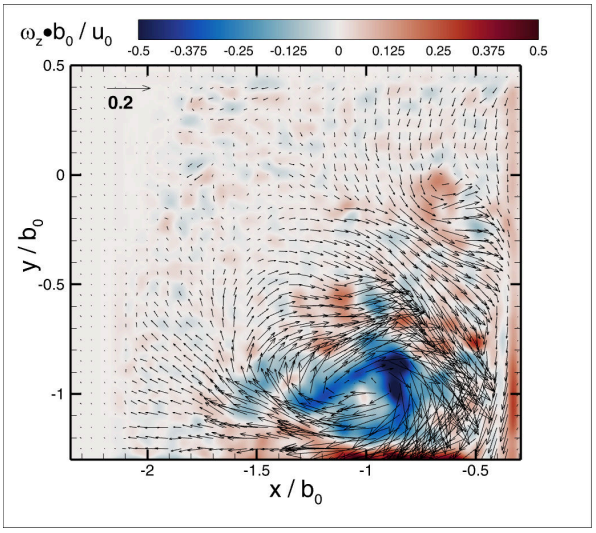

(a) Velocity field at $\tau = 2.3$.

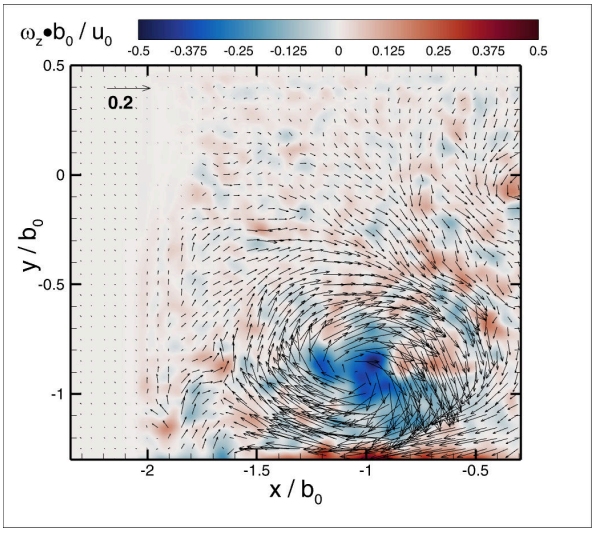

(b) Velocity field at $\tau = 2.9$.

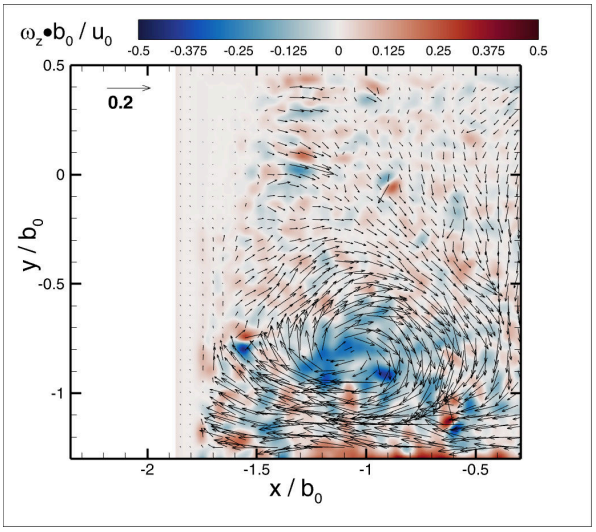

(c) Velocity field at $\tau = 3.4$.

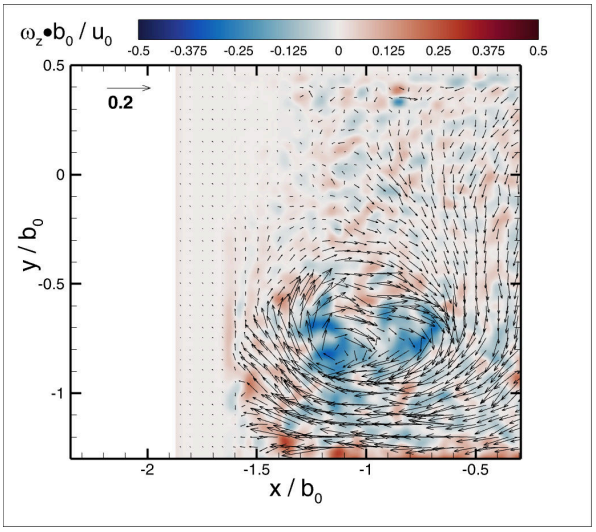

(d) Velocity field at $\tau = 3.8$.

Figure 5.7: $FOV_{90°}$ velocity field of wake vortex at $h_{AG} = 1 \cdot c$.

The circulation assumes a so-called "hill" shape as seen for vortices with severe jet components (swirling jets). This "hill" shape is measured and described by Liang et al. [92]. They categorize the flow into two regions on each side of the peak (hill), before the peak as the vortex core and after the peak as the shear layer. In general, the circulation profiles measured are in qualitative agreement with the ones reported by Liang et al. [92]. Given these similarities, the data suggest that the stagnation point of the linked vortex enhances a jet component. As described in the previous chapter, this jet component enriches the jet-like axial flow that ensues disturbances after deceleration and vortex ground linking.

2D3C PIV measurements can provide evidence of this particular observation in the future. Particularly Figure 5.8b shows a peak at $\tau = 2.3$ of $\Gamma_0/\Gamma \approx 0.35$. As time passes, the peak in circulation reduces, and the distribution evens out. Moreover, the position of highest circulation moves towards greater radii. These changes result from vortex decay [93].

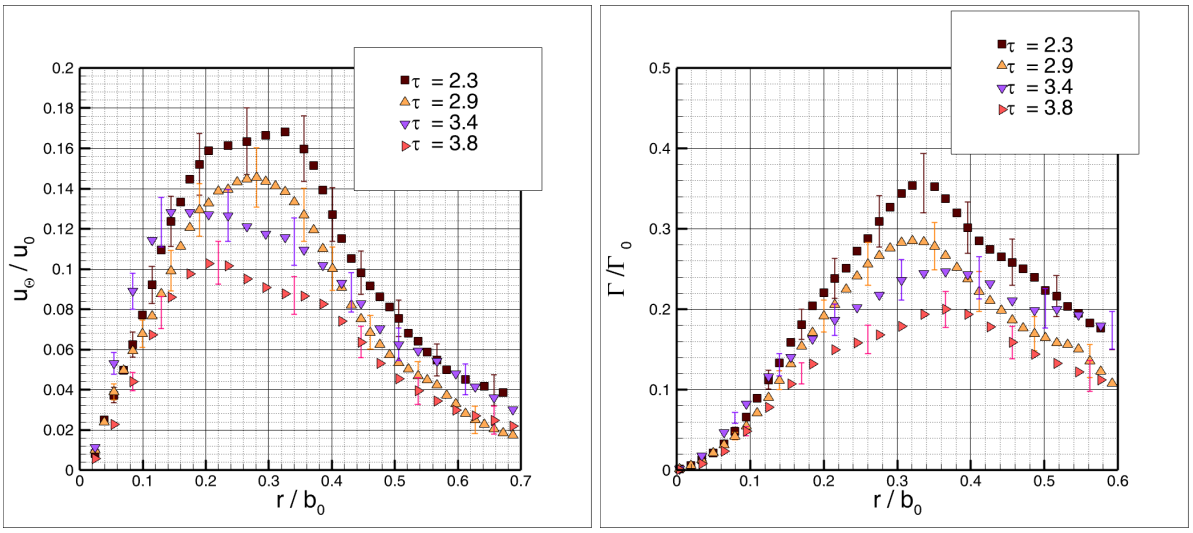

(a) Swirl velocity in the range $\tau = 2.3$ to $\tau = 3.8$.

(b) Circulation profile computed with the swirl velocities of Figure 5.8a .

Figure 5.8: Average swirl velocity and circulation time development of the wake vortex at $FOV_{90°}$.

Wake vortex drifting at tilted plane $FOV_{45°}$ and $h_{AG} = 1 \cdot c$

Figure 5.9 shows four snapshots of the PIV velocity measurements taken at a light sheet tilt angle of 45°. The axially and laterally drifting vortex is sweeping through the FOV. Due to the tilted light sheet, the perception of the sweeping is enhanced. This vortex enters from the far wake site and exits at the ground linking location, as can be observed in Figure 1.6, 2.11, and 2.12. Figure 5.9a shows the vortex entering the FOV at the time $\tau = 2.7$, here the vortex stretching and meandering are substantial and lead to a bifurcation, resulting in two cores within the FOV. This observation is consistent with the study by Holzäpfel et al. [94].

Also, judging by the vector magnitude, stretching and meandering result in a severe (unsteady) asymmetric increase in velocity (azimuthal velocity and pressure gradients). At the time $\tau = 3.1$, the vortex reorganizes, featuring a symmetric shape. Likewise, there is lateral drift, but instead of rebound, the vortex approaches the ground.

This approach is due to the previously explained sweep of the FOV, i.e., the vortex ground linking location moves towards the light sheet. The approaching of the ground linking location towards the FOV is proceeding as seen at times $\tau = 4.2$ and $\tau = 5.5$, along with the expected decay characteristics and lateral drift.

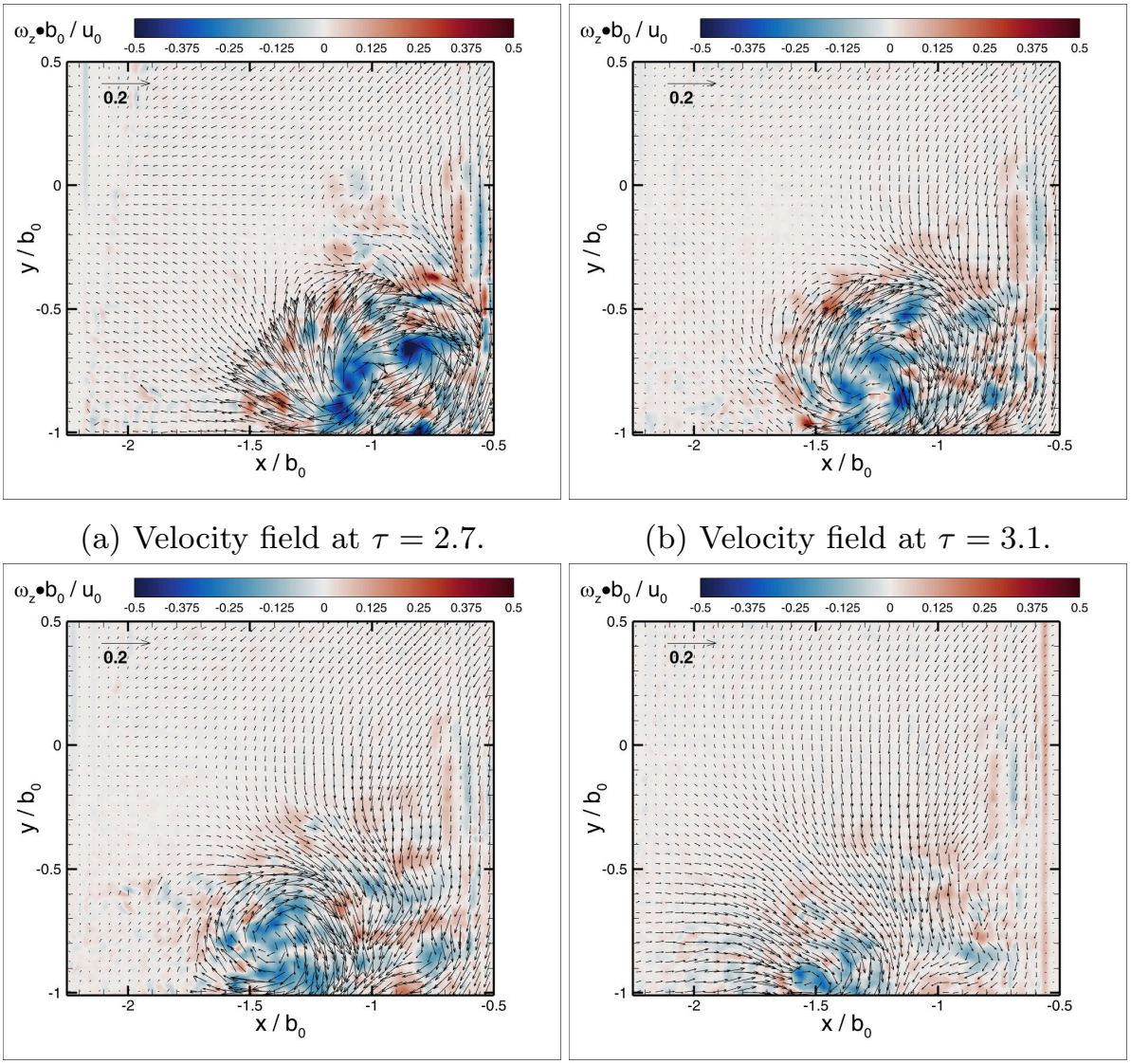

(a) Velocity field at $\tau = 2.7$.

(b) Velocity field at $\tau = 3.1$.

(c) Velocity field at $\tau = 4.2$.

(d) Velocity field at $\tau = 5.5$.

Figure 5.9: Velocity field of wake vortex at $h_{AG} = 1 \cdot c$.

The radial profiles for swirl and circulation are displayed in Figure 5.10. It is noteworthy that at $\tau = 2.7$ (as depicted in Figure 5.10a), the vortex detection algorithm identifies the center as the midpoint between two vorticity minima positioned at $x/b_0 \approx -0.9, y/b_0 \approx -0.6$.

As a result, the two peaks are averaged out, leading to only one peak being observed for the swirl velocity at this particular time. Nonetheless, the vortex velocity fields' characteristics (previously discussed) are reflected in the radial distributions. For example, Figure 5.10a shows the peak decrease in tangential velocity as time proceeds. Similarly, as the vortex ground linking location approaches the FOV (giving the impression of decreasing and getting closer to the ground), the swirl velocity decreases accordingly. Likewise, Figure 5.10 describes this trend in the circulation profiles.

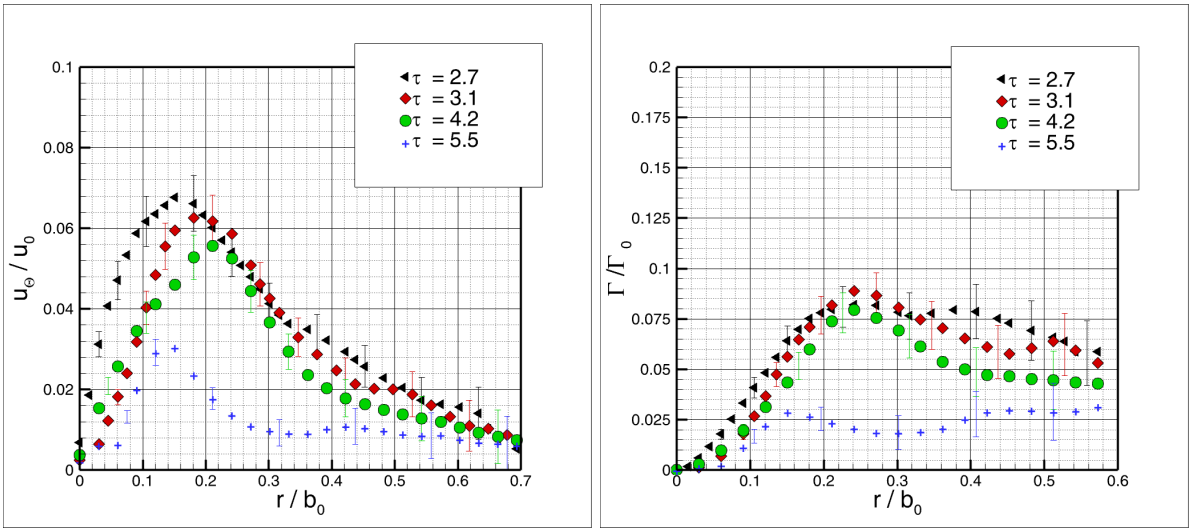

(a) Swirl velocity profiles in the range $\tau = 2.7$ to $\tau = 5.5$.

(b) Circulation profiles computed with the swirl velocities of Figure 5.10a .

Figure 5.10: Average swirl velocity and circulation time development of the wake vortex at FOV_{45°.

Ground linked-wedge vortex at ground reference plane ($FOV_{GP,ref}$ and $h_{AG} = 1 \cdot c$)

In this case, the light sheet lies parallel to the ground, and the field of view is labeled $FOV_{GP,ref}$. Right after the wing comes to rest, a strong velocity front moves away from the wingtip (mainly laterally). This velocity front revolves around an emerging concentrated vortex (near the wingtip). This development is depicted in Figure 5.11a, where the velocity front (that goes along the line $x/b_0 \approx -0.6$) displays coherence and ground linking is evident at $x/b_0 \approx -0.6, z/b_0 \approx -0.4$. This particular velocity field is the signature of a vortex that forms a wedge angle with the ground, as shown in Figure 1.1.

As the vortex further develops (Figure 5.11b $\tau = 3.1$), the ground linking leaves its footprint behind, while simultaneously, the velocity front begins to merge with the linked vortex. This evolving pattern is displayed in Figure 5.11c and 5.11d. Furthermore, the linked vortex moves in lateral $(-x/b_0)$ and axial $(-z/b_0)$ direction. In addition to its displacement, the linked vortex begins to decay, as seen by the swirl velocity magnitude decrease and the simultaneous core increase. Additionally, the remaining vortex footprint begins to dissipate ($x/b_0 \approx -0.5, y/b_0 \approx -0.5$ time $\tau = 4.5$ to $\tau = 6.5$).

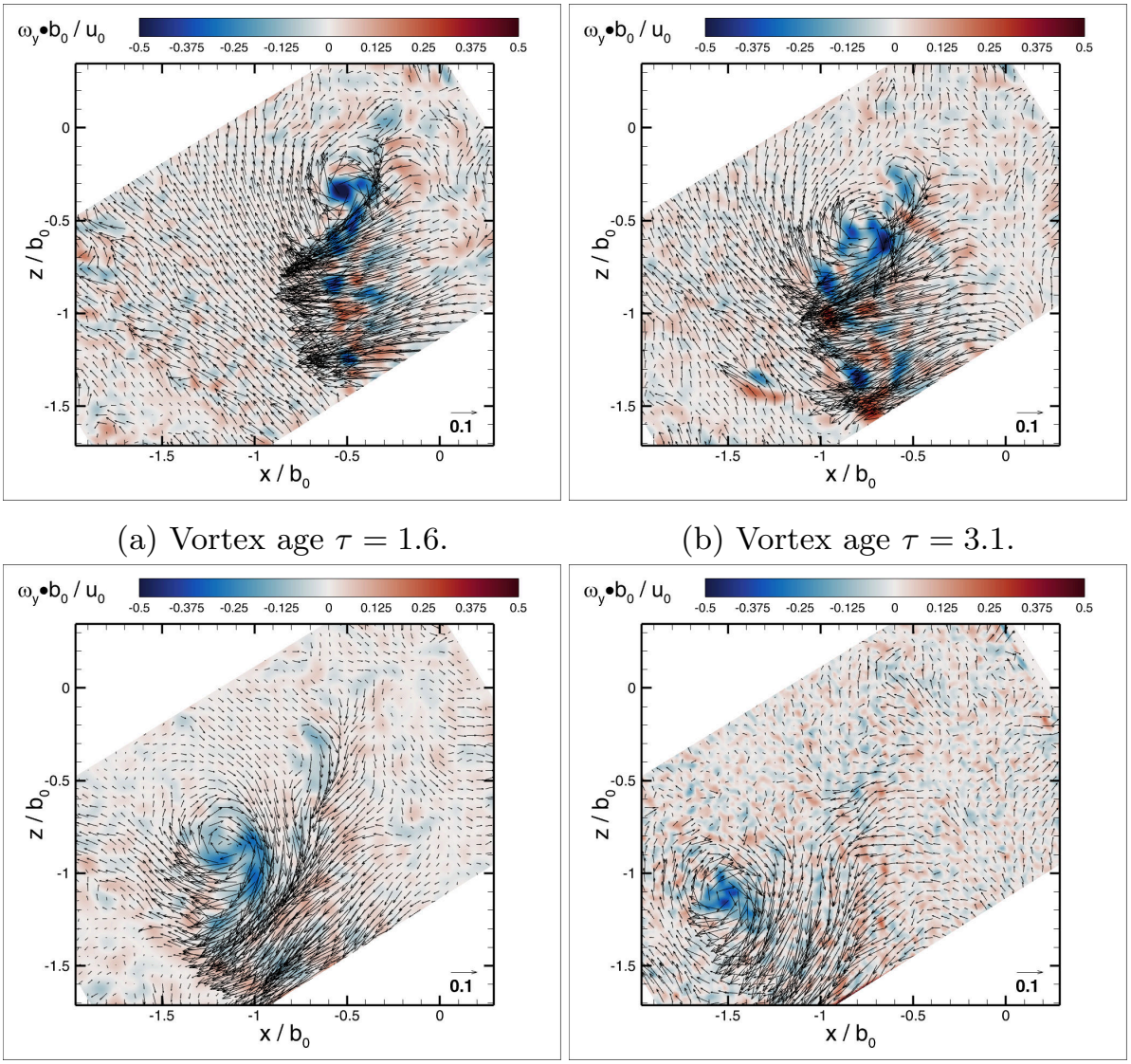

(a) Vortex age $\tau = 1.6$.

(b) Vortex age $\tau = 3.1$.

(c) Vortex age $\tau = 4.5$.

(d) Vortex age $\tau = 6.5$.

Figure 5.11: $FOV_{GP,ref}$ velocity field of wake vortex at $h_{AG} = 1 \cdot c$.

Persisting standing vortex at the ground plane $FOV_{GP,shift}$ and $h_{AG} = 1 \cdot c$

Because of the vortex drift, the ground-linking spot exits the $FOV_{GP,ref}$ at the left bottom corner. In order to follow the vortex, the FOV is shifted accordingly and labeled $FOV_{GP,shift}$ and plotted in Figure 5.12. The developing pattern described in Figure 5.11c proceeds. Again, as

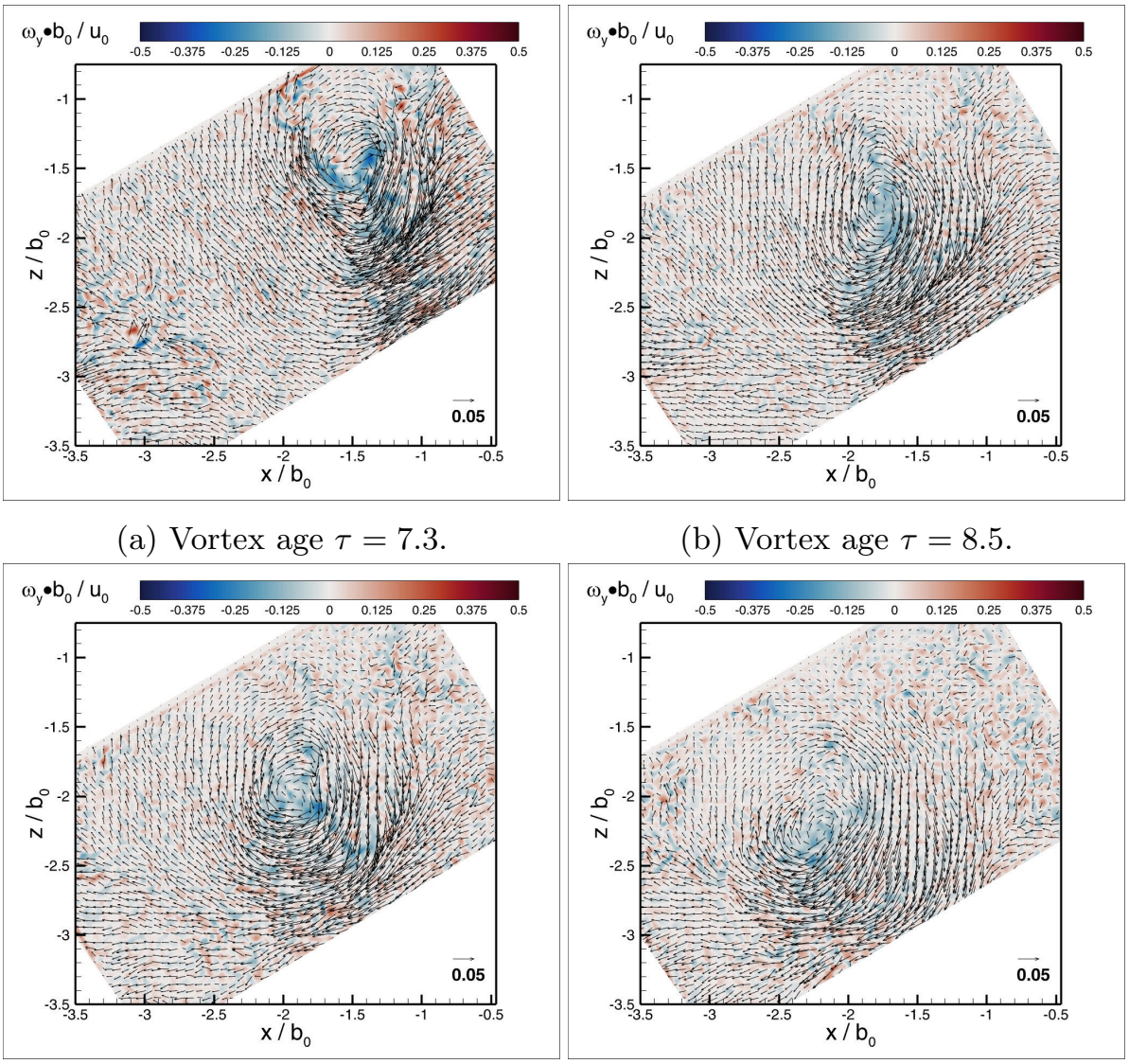

(a) Vortex age $\tau = 7.3$.

(b) Vortex age $\tau = 8.5$.

(c) Vortex age $\tau = 10.6$.

(d) Vortex age $\tau = 12.6$.

Figure 5.12: $FOV_{GP,shift}$ velocity field of wake vortex at $h_{AG} = 1 \cdot c$.

the vortex ages, the core exhibits moderate in-plane deformation. Contrary to the wedge angle signature described before, the vortex forms an oblique angle with the ground as it ages until it stands upright, as visualized in Figure 1.2 and Figure 5.2.

This reorganized vortex leaves a new signature characterized by a minor deformed velocity distribution (azimuthal and radial).

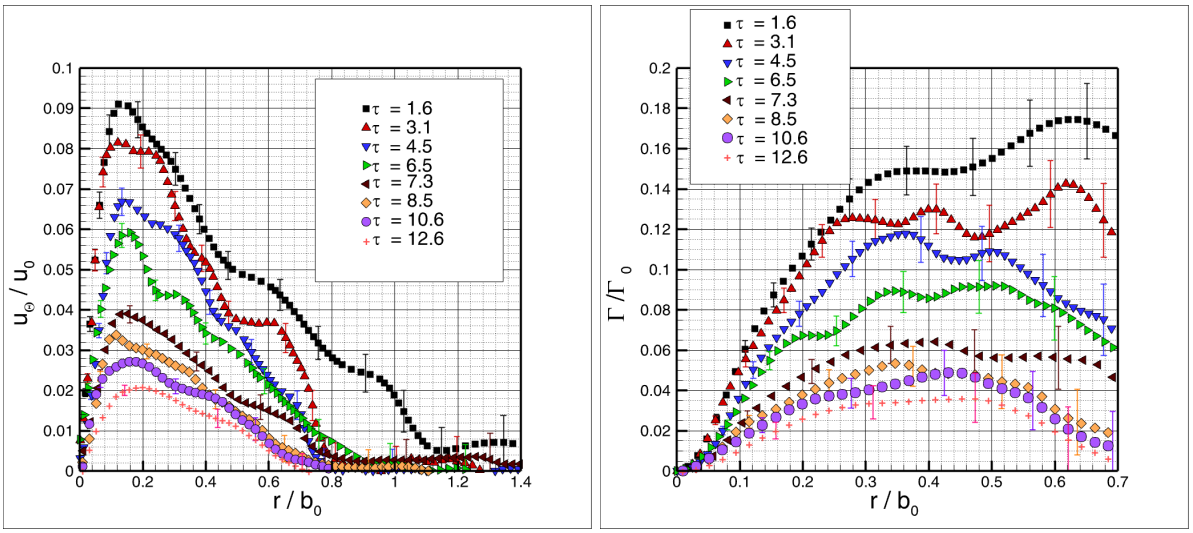

(a) Swirl velocity profiles in the range $\tau = 1.6$ to $\tau = 12.6$.

(b) Circulation profiles in the range $\tau = 1.6$ to $\tau = 12.6$.

Figure 5.13: Average swirl velocity and circulation time development of the wake vortex at $FOV_{GP,ref}$, $FOV_{GP,shift}$ and $h_{AG} = 1{\cdot}c$.

Lastly, the radial distribution of swirl velocity for the $FOV_{GP,ref}$ and $FOV_{GP,shift}$ is presented in Figure 5.13a here is put in evidence that the velocity front revolving around the linking location imposes a multiple peak distribution. Therefore the velocity front has regions of increasing/decreasing velocity outward from the vortex center. As the speed increases and surrounds the concentrated vortex, the swirling motion becomes smoother (notable when comparing $\tau = 1.6$ to $\tau = 8.5$). Additionally, in this time interval, the peak in swirl velocity, located at $r/b_0 \approx 0.2$, remains nearly constant, suggesting that despite the deformations, wake stretching, and meandering, the core holds its diameter. Eventually, while the velocity magnitude decreases for all vortex ages, the onset of decay is visible beyond $\tau = 8.5$. Here, the characteristic core size increase and flattening of the distribution are evident.

Figure 5.13b shows the circulation profiles. The circulation increases from the vortex center until it reaches the core boundary (please note that the horizontal axis is adjusted). Beyond the vortex core, multiple peaks in the swirl velocity create alternating maxima and circulation minima. However, in contrast to cases where the light sheet is perpendicular to the ground, the circulation only reaches a maximum value of $\Gamma/\Gamma_0 \approx 0.18$.

5.3.2 End of trajectory at $h_{AG} = 6 \cdot c$ (300 mm) distance to the ground

In the current case, the wing comes to rest at a distance from the ground $h_{AG} = 6 \cdot c$, equivalent to one wingspan. Here, the bound vortex detaching from the wing's final position (closest to the ground) is the NGE ($b < z < 3 \cdot b$) to IGE ($z < b$) interface region. Because of the angle of approach $\gamma = 5°$, the older portion of the vortex (opposite to the towing direction) is located only in the NGE domain.

As previously mentioned (Section 1.3), the vortices have a minor reaction to the ground in this domain. However, due to the wing deceleration and the change of effective angle of attack ([95]), L- and R-vortex reconnect and form a horseshoe vortex as described by Sarpkaya [96].

Vortex stretching and bending at cross-section plane $FOV_{90°}$ and $h_{AG} = 6 \cdot c$

The discussion begins with the case $FOV_{90°}$ Figure 5.14a. Compared with the previous case, the L-vortex core is inside the FOV much later ($\tau = 4.5$). In addition, the vortex core has an oval shape that matches the previous case at a similar age of the vortex. Despite this similarity, the vortex strength is higher, as seen in the vector field annular concentration. At $\tau = 5.4$ (Figure 5.14b), the vortex core is axially symmetric and concentrated in the center. The symmetry is disrupted at $\tau = 6.2$ (Figure 5.14c) when the vortex core seems to be split in two due to bifurcation, as described in the prior cases.

Likewise, the deformation due to stretching, increases as the vortex reaches the left FOV boundary and leaves the measurement region ($\tau = 7.0$ (Figure 5.14d). During this series of events, two things are happening simultaneously. First, as expected, there is decay, which involves a decrease in swirl velocity and an increase in core diameter. Second, the vortex center remains at a constant height above the ground, approximately $y_c/b_0 \approx 0.4$, while it shifts laterally.

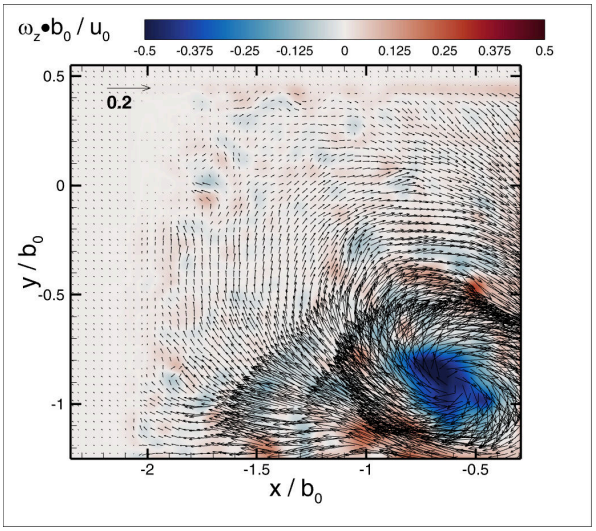

(a) Velocity field at $\tau = 4.5$.

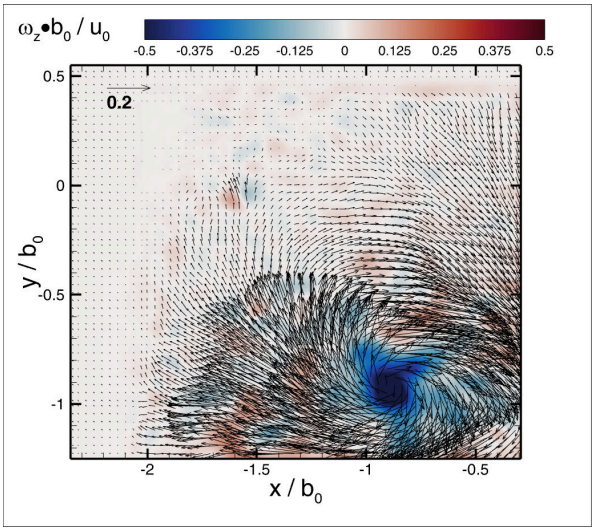

(b) Velocity field at $\tau = 5.4$.

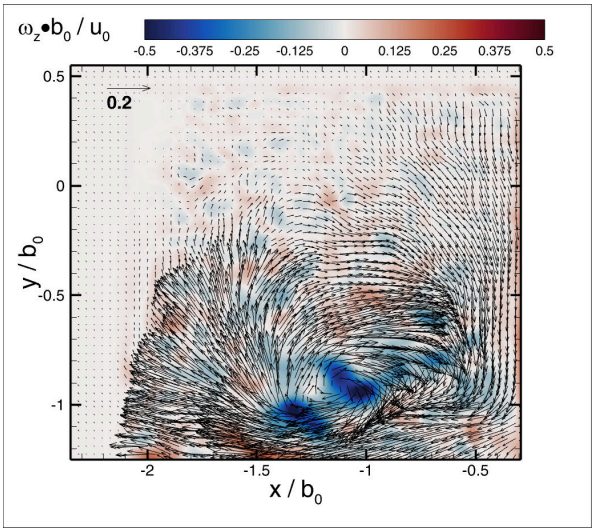

(c) Velocity field at $\tau = 6.2$.

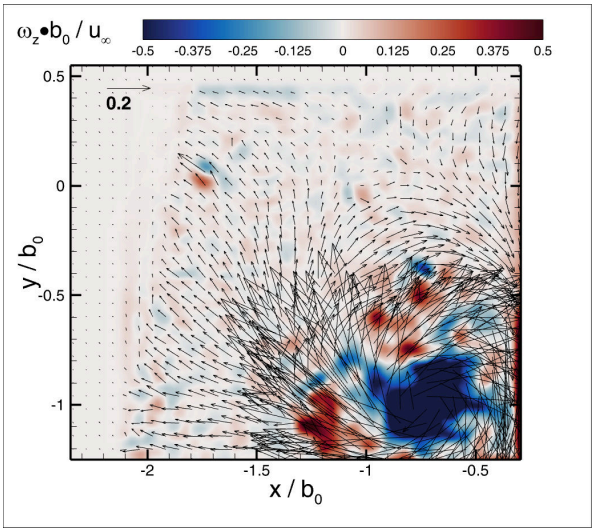

(d) Velocity field at $\tau = 7.0$.

Figure 5.14: FOV_{90° velocity field of wake vortex at $h_{AG} = 6 \cdot c$.

Secondary vortex detachment in the tilted plane $FOV_{45°}$ and $h_{AG} = 6 \cdot c$

In the tilted light sheet arrangement, the complete L-vortex is inside the FOV much later at $\tau = 6.3$, as displayed in Figure 5.15a and shows a different behavior for all vortex ages. The primary vortex with negative vorticity $\omega_x \cdot b_0/u_0 \approx -0.5$ is symmetrically concentrated at its center ($x/b_0 \approx -0.9$ and $y/b_0 \approx -0.8$) and induces a secondary vortex with vorticity of opposite sign ($\omega_x \cdot b_0/u_0 \approx 0.4$) located at $x/b_0 \approx -1.35$ and $y/b_0 \approx -0.8$.

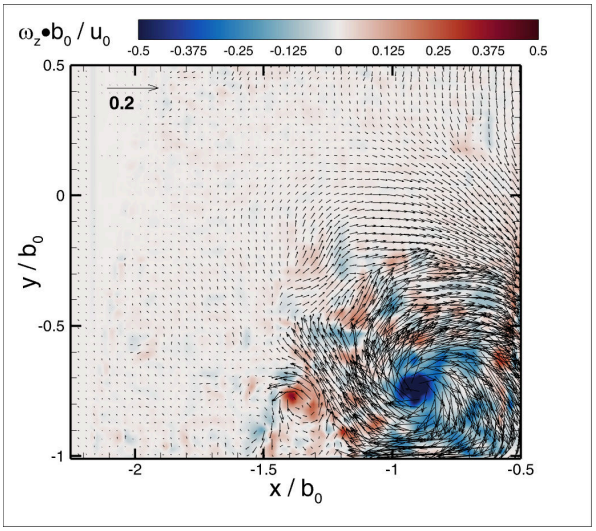

(a) Velocity field at $\tau = 6.3$.

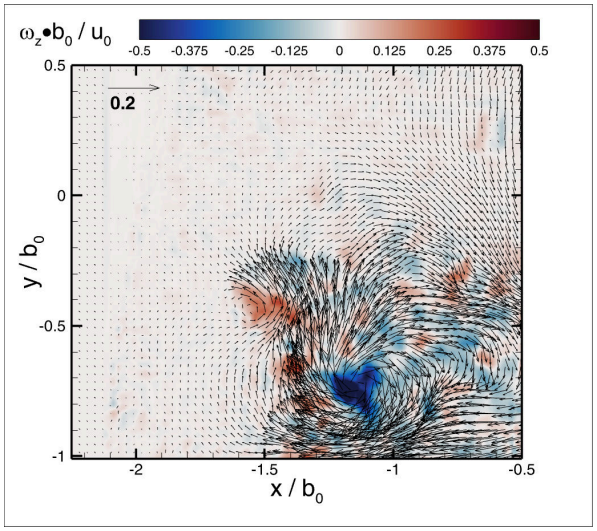

(b) Velocity field at $\tau = 7.4$.

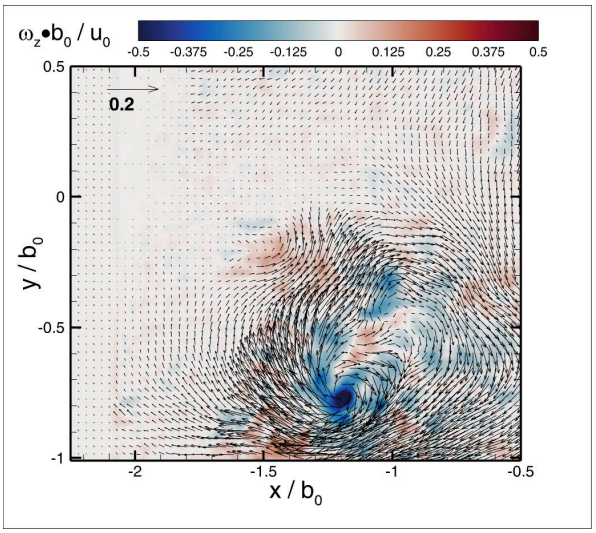

(c) Velocity field at $\tau = 7.9$.

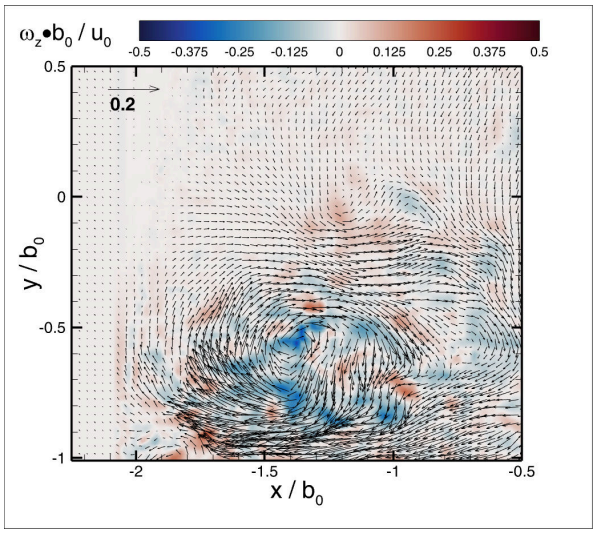

(d) Velocity field at $\tau = 8.8$.

Figure 5.15: $FOV_{45°}$ velocity field of wake vortex at $h_{AG} = 6 \cdot c$.

Because the main vortex sustains its position for a longer time (due to the formed horseshoe vortex as described later), the vorticity layer induced at the ground develops enough to detach in the form of a secondary vortex as a consequence of the positive pressure gradient, as explained in Section 1.2.1 and the references given there. Further experimental evidence of secondary vortices and the related instabilities are given by Williamson et al. [97] and Chen et al. [91] where they corroborate that after the secondary vortices detach, they orbit around the primary (main vortex) one. The orbiting of the secondary vortex around the primary aligns with the measurements from $\tau = 6.3$ to $\tau = 7.9$. At $\tau = 7.4$ (Figure 5.15b), the main vortex features stretching and meandering delocalized from the core ($x/b_0 \approx -0.75$ and $y/b_0 \approx -0.7$) related to the severe primary and secondary vortex interaction.

Beyond $\tau = 7.9$ Figure 5.15c, the secondary vortex merges with the primary, and the remaining exhibits an asymmetric deformation. This deformation is visible at $x/b_0 \approx -1$ and $y/b_0 \approx -0.6$ and suggests that it is the outcome of the vortices merging as the secondary vortex follows a spiral trajectory (with the primary vortex at the center). Lastly, at $\tau = 8.8$ Figure 5.15d, the remaining weak vortex cannot reorganize and suffers the onset of decay.

Horseshoe vortex linking in the ground reference plane ($FOV_{GP,ref}$ and $h_{AG} = 6 \cdot c$)

As the wing's terminal height above the ground increases, the vortices display minor variations in the sequence of events starting from ground linking. Finally, at a distance of one wingspan ($h_{AG} = 6 \cdot c$) the wingtip vortices no longer link to the ground and instead link with their counterparts. In this case, since the vortex forms a horseshoe (as shown in Fig. 5.5a), it is first prone to Crow deformations before it links to the ground. [95], [1]. The L- and R-vortex linking to a horseshoe vortex is the departing event discussed here and is shown in Figure 5.16a ($FOV_{GP,ref}$). The bound vortex that detaches from the wing is very close to the trailing edge at a horizontal line through $z/b_0 \approx -0.25$ between $x/b_0 \approx -0.6$ and $x/b_0 \approx 0.1$. A velocity front due to the proximity to the ground of the descending vortex emerges (from right to left). This velocity front has a margin of several interconnected curves. This arrangement is interpreted as the footprint of the deformed vortex with portions closer to the ground impinging the induced vorticity layer.

A similar flow field is found in the wake vortices created by a rotor blade when taking a 2D slice (cutting through the cross-section of the vortices) as found in Schwarz et al., [98]. This similarity supports the idea that approaching the ground is enough to impose a localized vortex field because of the deformation (vortex stretching, bending, among others) in some vortex parts. Furthermore, the upfront of the horseshoe

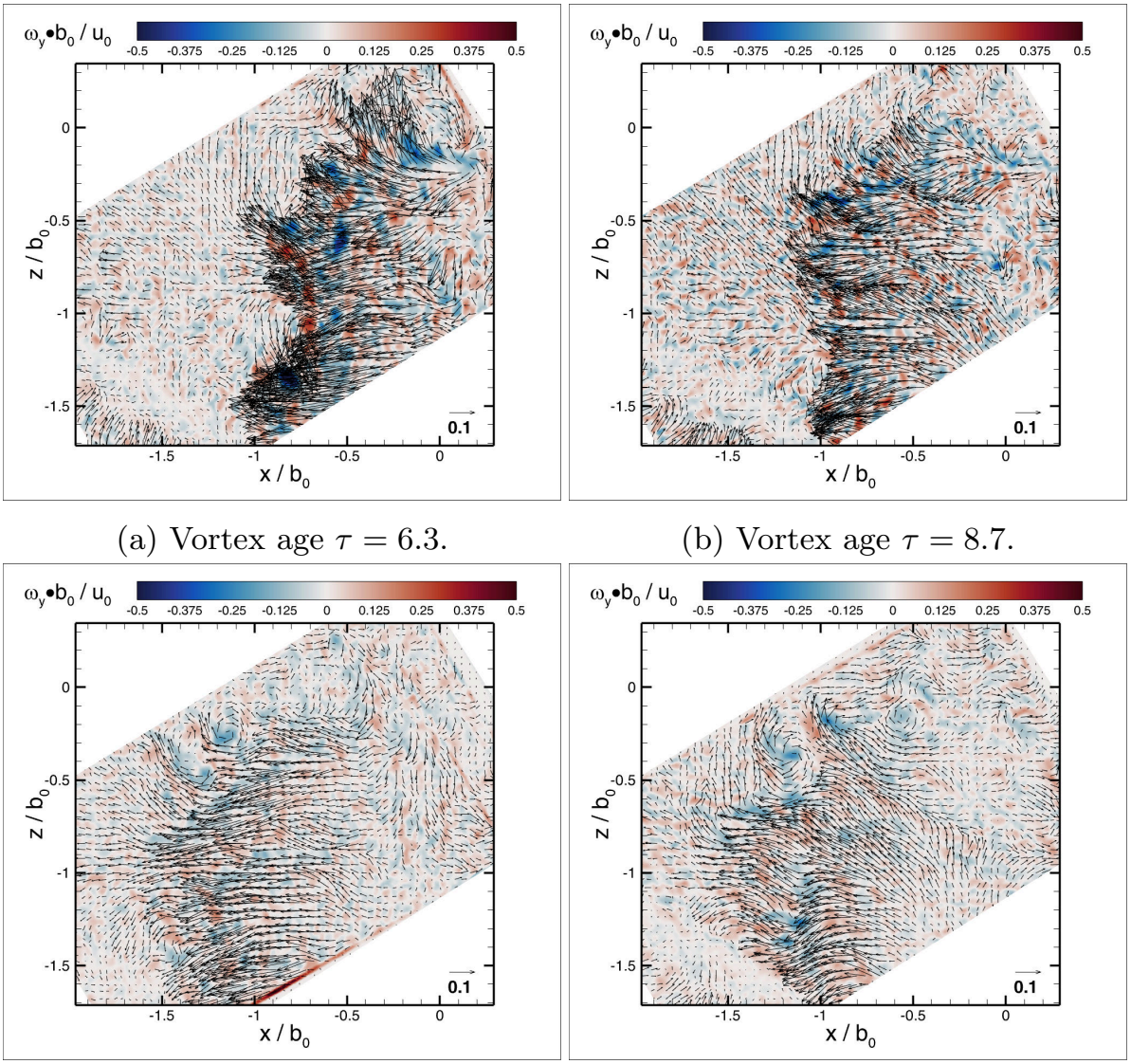

(a) Vortex age $\tau = 6.3$.

(b) Vortex age $\tau = 8.7$.

(c) Vortex age $\tau = 10.6$.

(d) Vortex age $\tau = 11.4$.

Figure 5.16: $FOV_{GP,ref}$ velocity field of wake vortex at $h_{AG} = 6 \cdot c$.

vortex indicates dissipation, as seen in Figure 5.16b in the induced velocity at the ground (reduced vector concentration and magnitude). At the position $x/b_0 \approx -0.9$ and $z/b_0 \approx -0.4$, the vortex seems to develop ground linking.

From this corner point in $-z/b_0$ direction, the velocity fronts aligns along the vertical line $x/b_0 \approx -1$. The trend evolves as the vortex ages while the velocity field decreases in magnitude, as depicted in Figure 5.16c, where the vortex links to the ground at $x/b_0 \approx -1$ and $z/b_0 \approx -0.3$. Figure 5.16d shows the first hint of multiple vortices linking, one at $x/b_0 \approx -1.1$, $z/b_0 \approx -0.4$ (the one described in Figure 5.16c) and a second one at $x/b_0 \approx -0.6$, $z/b_0 \approx -0.3$. Lastly, the linked vortices for both times impact their surroundings in addition to the complex deformation at the given position. This impact results in the arc embracing the linked vortex, for instance, shown in Figure 5.16c at $x/b_0 \approx -1.4$ to $x/b_0 \approx -1.6$ and $z/b_0 \approx -0.6$ to $z/b_0 \approx -1.6$. However, contrary to the cases in Figure 5.11, besides ground linking occurring much later, the vortex display mainly lateral drift with negligible axial drift.

Multiple vortex linking in the shifted ground plane ($FOV_{GP,shift}$ and $h_{AG} = 6 \cdot c$)

In this case, the current vortex system likely comprises two closed vortex loops and a standing vortex at the ground. Consequently, two locations of vorticity with opposite sing are evident: one negative at $x/b_0 \approx -1.6$, $z/b_0 \approx -1.1$ and one positive at $x/b_0 \approx -1.8$, $z/b_0 \approx -1.6$ in Figure 5.17a. Judging by the proximity of these two linked vortices and the velocity field between them, they likely form a closed loop standing up vertically from the ground, as shown by Stephan et al., [21]. Furthermore, the signature of this vortex pair, i.e., the equal magnitude of vorticity, the flow expelled along their symmetry line, among others, resembles a vortex ring that links to a free surface [99]. This signature strongly suggests that the structure forms a closed loop with legs attached to the ground (at the center of the negative and positive peak vorticity).

In addition, one additional linking location is noticed, at $x/b_0 \approx -1.4$, $z/b_0 \approx -2.1$. Finally, at $\tau = 13.1$ (Figure 5.17b), the vorticity of the ring vortex seems to collapse and to dissipate the vortex. The resulting substantial velocity gradients of this event enhance the viscous dissipation of the vortex [21]. Inspecting the subsiding vortex at the center of the FOV at $x/b_0 \approx -1.6$, $z/b_0 \approx -2.2$, an adjacent velocity front consolidates. As time passes, the velocity front next to the vortex consistently supplies it with vorticity, causing it to grow.

This process results in a coherent flow field that surrounds the remaining vortex, located at $x/b_0 \approx -2.1$, $z/b_0 \approx -2.3$ for time $\tau = 14.9$ in Figure 5.17c and $\tau = 15.9$ in Figure 5.17d. Based on the data so far, it is evident that although there are different vortex-developing mechanisms (such as the creation of a horseshoe vortex followed by multiple ground linkings), there is still one vortex that emerges later and lasts long. Furthermore, this particular vortex does not appear to move much in a lateral or axial direction, similar to the hazardous vortices that can occur during the landing of an aircraft, as explained in Section 1 and its accompanying references.

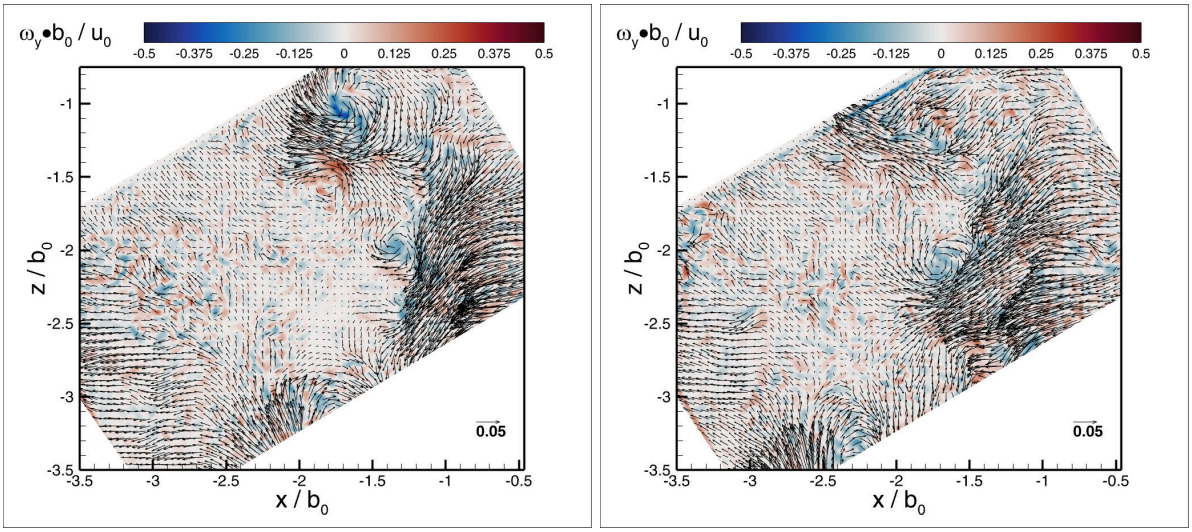

(a) Vortex age $\tau = 12.7$.

(b) Vortex age $\tau = 13.1$.

(c) Vortex age $\tau = 14.9$.

(d) Vortex age $\tau = 15.9$.

Figure 5.17: $FOV_{GP,shift}$ velocity field of wake vortex at $h_{AG} = 6 \cdot c$.

5.3.3 Development of vortex parameters with h_{AG} and a_{dec} variation

In the present section, the temporal evolution of the vortices is discussed. Each vortex is represented by two parameters: the position of the vortex center and its circulation. The extraction of these parameters is explained in detail in Section 2.4. The discussion is layout with the figures in the same order as before first, the cross-section plane (FOV_{90°), then the tilted plane (FOV_{45°), and lastly, the plane parallel to the ground ($FOV_{GP,ref}$) but aiming to characterize the whole vortex with the three perspectives simultaneously.

This analysis enables the reconstruction and description of the complex three-dimensional vortex development in an approximated sense since only 2D slices are available. Note that in the FOV_{45° (Figure 5.18d) due to the tilt of the light sheet and the vortices linking location drift towards the FOV, as the vortex age increases, the vortices observed are first old (further wake location) and then young (closer to the linking location). Nevertheless, for completeness, the plots are part of the discussion. The discussion begins with the vortex closest to ground $h_{AG} = 1 \cdot c$ (one chord length). As seen in Figure 5.18a, this vortex sustains its elevation above the ground for an extensive range of lateral drift; it exhibits an apparent lifting from the ground at a position of $x/b_0 \approx -1.8$.

This lifting is due to the vortex dominating axial drift that shifts the linked-standing vortex towards the FOV. The circulation time evolution on the ground conforms with the results of Stephan et al. [49], [100]. A trend is observed from $h_{AG} = 1 \cdot c$ and the successive heights $h_{AG} = 2 \cdot c$ and $h_{AG} = 3 \cdot c$. As the wing's final distance above the ground increases, the vortex lifts from the ground at a decreasing lateral position (closer to the wingtip). In contrast, the vortex height above the ground holds a nominal value from $h_{AG} = 4 \cdot c$ and $h_{AG} = 6 \cdot c$. These features suggest that vortex rebound and axial drifting decrease as the terminal height above the ground increases past $h_{AG} = 4 \cdot c$. Figure 5.18b displays the changes in vortex circulation over time for each terminal height above the ground.

These results align with the current literature [49], [100]. The exponential decay of vortex circulation is observed, with the coefficient value shown in the legend. It is worth noting that as the aircraft's terminal height above the ground increases (represented by h_{AG}), the exponential coefficient also increases in magnitude. For example, it starts at -0.871τ at $h_{AG} = 1 \cdot c$ and goes up to -0.1127τ at $h_{AG} = 3 \cdot c$, before gradually declining and reaching -0.1653τ at $h_{AG} = 6 \cdot c$.

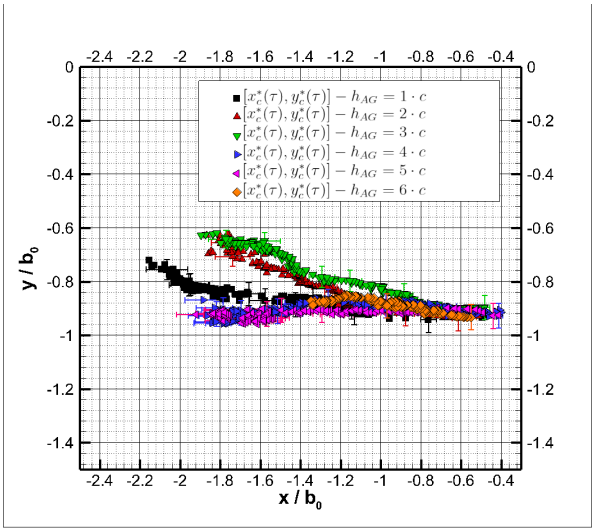

(a) Core trajectory $FOV_{90°}$

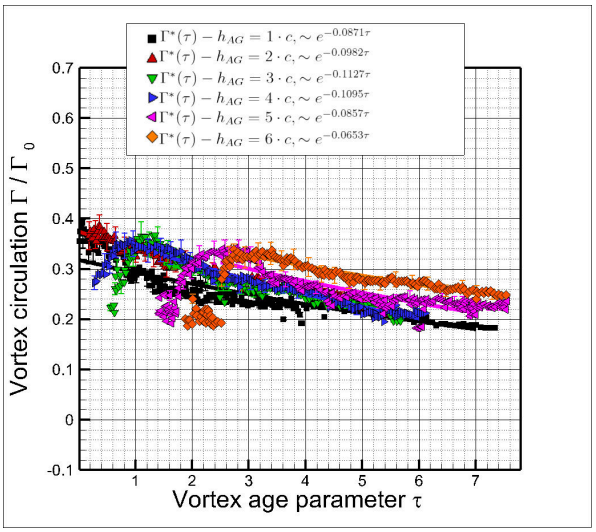

(b) Circulation for the $FOV_{90°}$

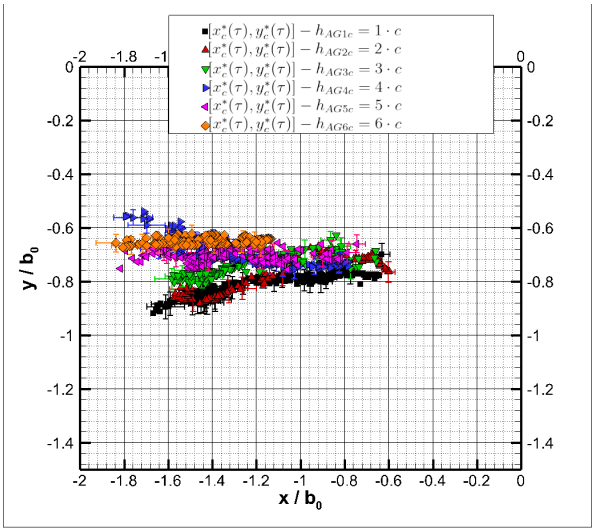

(c) Core trajectory $FOV_{45°}$

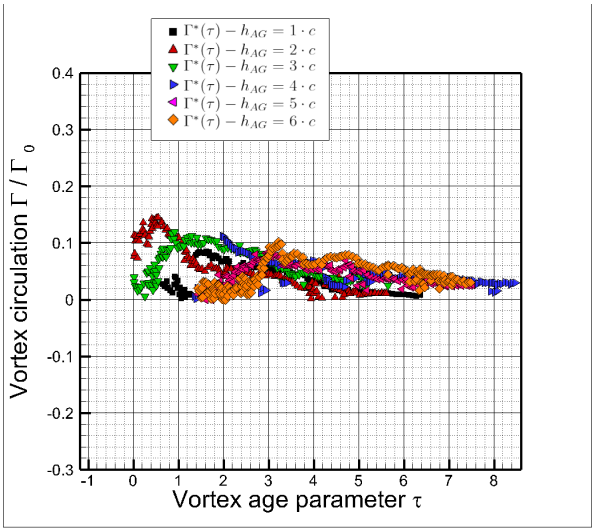

(d) Circulation for the $FOV_{45°}$

Figure 5.18: Vortex core trajectory for the planes $FOV_{90°}$, $FOV_{45°}$ and the time evolution of circulation.

In addition, an increase in h_{AG} results in a vortex consolidation age delay, i.e., the vortex reaches its maximum circulation (ending of roll-up) and begins to decay. Finally, at a mature age, the vortices converge for all cases. The wing's terminal height suggests having direct consequences in the vortex's early development and the ground linking type, as explained in the previous sections. In the next measurement, $FOV_{45°}$, the core trajectory for the cases $h_{AG} = 1 \cdot c$ to $h_{AG} = 3 \cdot c$ (Figure 5.18c) corroborates that the vortex linking location sweeps through the FOV, entering from the right until it exits to the left along a curved line.

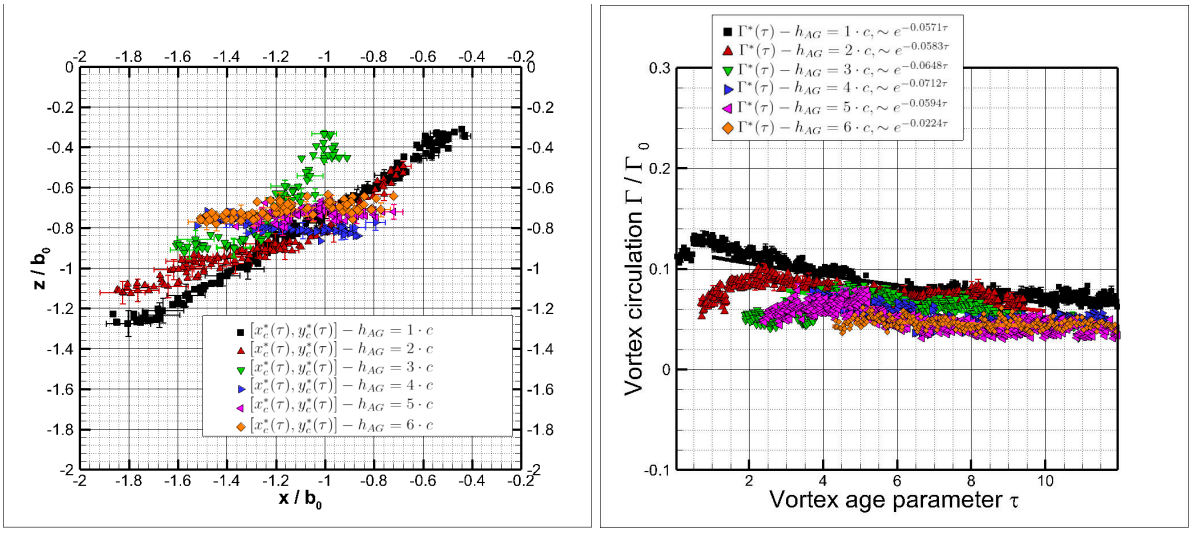

(a) Core trajectory $FOV_{GP,ref}$ (b) Circulation for the $FOV_{GP,ref}$

Figure 5.19: Vortex core trajectory for the plane of meassurments $FOV_{GP,ref}$ and the corresponding time evolution of vortex circulation.

At $h_{AG} = 4{\cdot}c$, the axial vortex drifts decreases, and the vortex rebound is evident in the concave-like shape of the core trajectory. After reaching $h_{AG} = 4{\cdot}c$, the vortices cease to instantly connect to the ground. Instead, the left and right vortices link together to create a horseshoe vortex. As a result, the vortices remain at a constant height for a longer duration while also experiencing lateral drift. In Figure 5.18d, there is a less smooth distribution observed for heights ranging from $h_{AG} = 1 \cdot c$ to $h_{AG} = 5 \cdot c$. At certain instances, there is a two-hill-like distribution, but the circulation decay follows an exponential trend. For example, in the circulation at $h_{AG} = 6 \cdot c$, one maximum (first hill) is located at vortex age $\tau \approx 3.0$ and the other at $\tau \approx 4.5$. This double hill distribution reflects, on the one hand, vortex meandering and bending, among others, and, on the other hand, bursting and simultaneous axial flows due to end-effects.

Figure 5.19a displays the significant axial drifting discussed previously, confirming the findings from the earlier subsections. Moreover, a similar pattern can be observed in the vortices between heights of $h_{AG} = 1 \cdot c$ to $h_{AG} = 6 \cdot c$, but with the difference that the axial drift of the vortices ceases while the lateral drift reduces. In addition, the vortex circulation in the ground plane shows a single peak value at the start of each time distribution (as shown in Figure 5.19b).

This characteristic suggests that the associated vortex grows stronger before eventually weakening. There is a noticeable pattern in the development of exponential coefficients, with their magnitude increasing from -0.0571τ at $h_{AG} = 1 \cdot c$ to -0.0712τ at $h_{AG} = 4 \cdot c$. However, after $h_{AG} = 5 \cdot c$, the coefficients start to decrease again and settle at a value of -0.0224τ at $h_{AG} = 6 \cdot c$. The presented findings show that the phenomenon of vortex rebound is consistent with the observations and data presented in the relevant literature [17], [49], [91]. In addition, the vortex circulation obtained, which decays over time, aligns with the LIDAR findings obtained by Holzäpfel et al. [101] and also by Sarpkaya [102].

5.4 Results: Changing the terminal deceleration

The current section presents the impact on vortex characteristics and ground interaction when changing the terminal deceleration. Two deceleration values are used, one representing a low-speed approach, which is half of the reference deceleration, and the other representing a fast-speed approach, which is twice the reference deceleration. Only the deceleration will be modified in this experiment series, so the terminal height above the ground will remain constant at $h_{AG} = 1 \cdot c$. In the last subsection, data for the $h_{AG} = 2 \cdot c$ case are additionally presented.

5.4.1 Low-speed approach $a_{dec} = 0.5 \cdot a_{ref}$

Low-speed approach $FOV_{90°}$

Figure 5.20 illustrates the progress of vortex cross-section development in the plane perpendicular to the ground. At $\tau = 2.9$, the vortex center is found at $x/b_0 \approx -0.75$ and $y/b_0 \approx -1$ (Figure 5.20a). This vortex state has some slight distortion, mainly around the center of the vortex and its surroundings. This deformation persists in Figure 5.20b, while the vortex maintains its distance from the ground by slowly drifting laterally. As time passes, at both $\tau = 5.5$ and $\tau = 5.5$ (as shown in Figures 5.20c and 5.20d), the vortex's velocity distribution becomes smoother, indicating a reduction in the ground interaction and an increase in vortex decay.

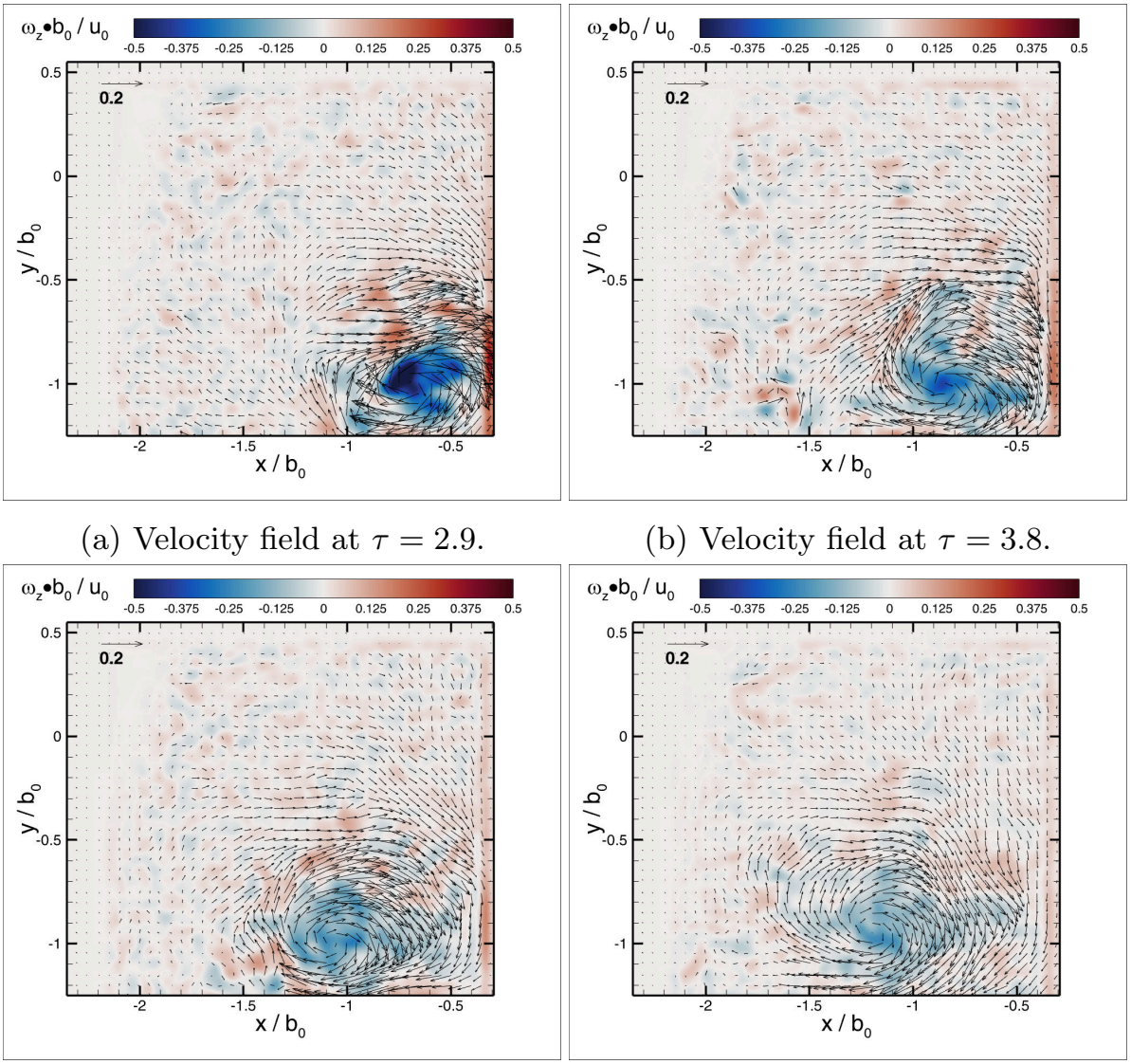

(a) Velocity field at $\tau = 2.9$.

(b) Velocity field at $\tau = 3.8$.

(c) Velocity field at $\tau = 5.5$.

(d) Velocity field at $\tau = 6.8$.

Figure 5.20: Low-speed approach $a_{dec} = 0.5 \cdot a_{ref}$ $FOV_{90°}$ velocity field of wake vortex at $h_{AG} = 1 \cdot c$.

Low-speed approach $FOV_{GP,ref}$

Figure 5.21 displays the velocity fields for $FOV_{GP,ref}$. In this case, there is a delay in the ground linking occurrence, and the vortex has a lower velocity magnitude. The linked vortex signature also shows unique characteristics. Observing the vortex connected to the ground at $\tau = 2.1$ in Figure 5.21a (midpoint of Fig.). The vortex's center lies at $x/b_0 \approx -0.6$ and $y/b_0 = -0.6$, and bears vorticity values of $\omega_x \cdot b_0/u_0 \approx -0.25$.

The right side of the vortex presents a wavy velocity front, which is attributed to two simultaneous events. The first is the vortex roll-up, which takes place over a longer period of time than the reference deceleration case. The second event is when the vortex tube gets very close to the ground, creating hills and valleys where the velocity vectors' agglomeration converges and diverges. Furthermore, for this case, it can be accentuated that the rate of vortex strength reduction is due to the lower wing deceleration rate in the terminal area. This condition is because the deceleration starts earlier, allowing the wing to come to a stop at the same position.

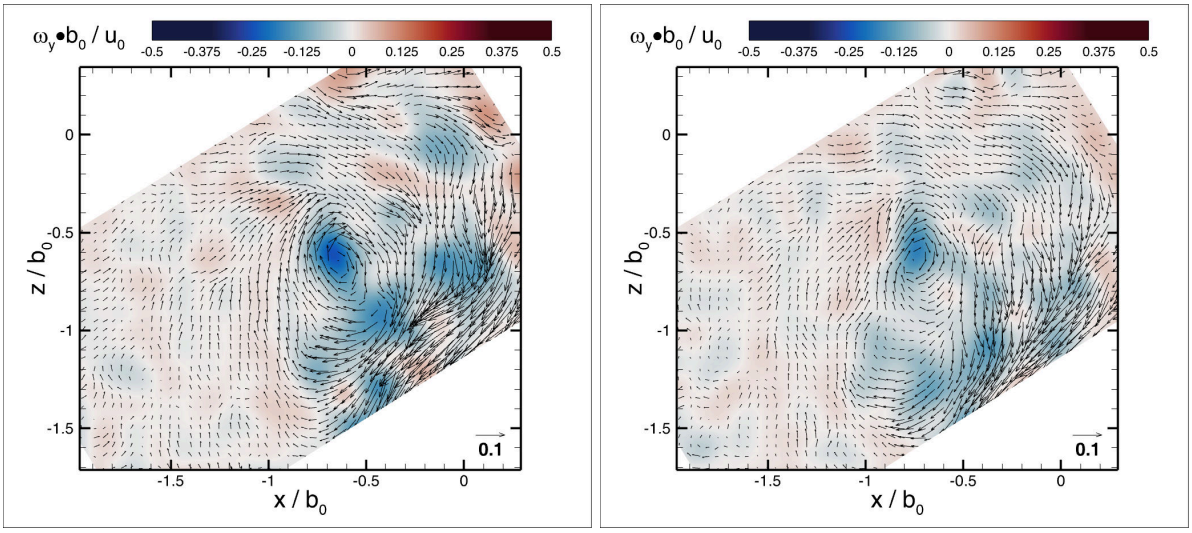

(a) Velocity field at $\tau = 2.1$.

(b) Velocity field at $\tau = 3.0$.

(c) Velocity field at $\tau = 5.4$.

(d) Velocity field at $\tau = 7.6$.

Figure 5.21: Low-speed approach $a_{dec} = 0.5 \cdot a_{ref}$ $FOV_{GP,ref}$ velocity field of wake vortex at $h_{AG} = 1 \cdot c$.

As a result, the wake vortex in the terminal area within a certain distance is not as strong as in the reference deceleration scenario. As the vortex ages, it moves slowly to the side while the connected vortex remains in the same spot. The velocity pattern of the older vortex remains the same, but the linked vortex weakens, causing the velocity front to alternate between smooth and wavy. This behavior indicates that the twisted vortex rotates towards and away from the ground. This situation is illustrated in Figures 5.21a to 5.21d.

5.4.2 High-speed approach $a_{dec} = 2 \cdot a_{ref}$

High-speed approach: $FOV_{90°}$

To achieve a high-speed approach, the terminal deceleration rate is increased to twice the reference level. Consequently, the deceleration starts later because the wing always ends its trajectory at the same height regardless of the scenario. The strength of the vortex is more substantial when it is closer to the ground than for the reference deceleration case. This condition is shown by the higher magnitude of velocity and vorticity in a given range, as shown in Figure 5.22. At $\tau = 1.8$, the vortex roll-up occurs quickly, resulting in a robust vortex with a vorticity magnitude of $\omega_x \cdot b_0/u_0 \approx -0.5$, as shown in Figure 5.22a.

It is important to note that there is severe lateral drifting due to the enhanced vortex strength while the vortex height above the ground remains constant. While the vortex drifts from $x/b_0 = -0.6$ to $x/b_0 = -0.9$ (Figure 5.22b), it stretches and propels the flow beneath it outwardly. The propelled flow moves from right to left, turns around the core, and merges with the vortex. This pattern continues for times $\tau = 2.7$ (as seen in Figure 5.22c) and $\tau = 3.1$ (as seen in Figure 5.22d), resulting in a three-polar deformation of the vortex core in the former (Figure 5.22c) and a splitting into two in the latter (Figure 5.22d).

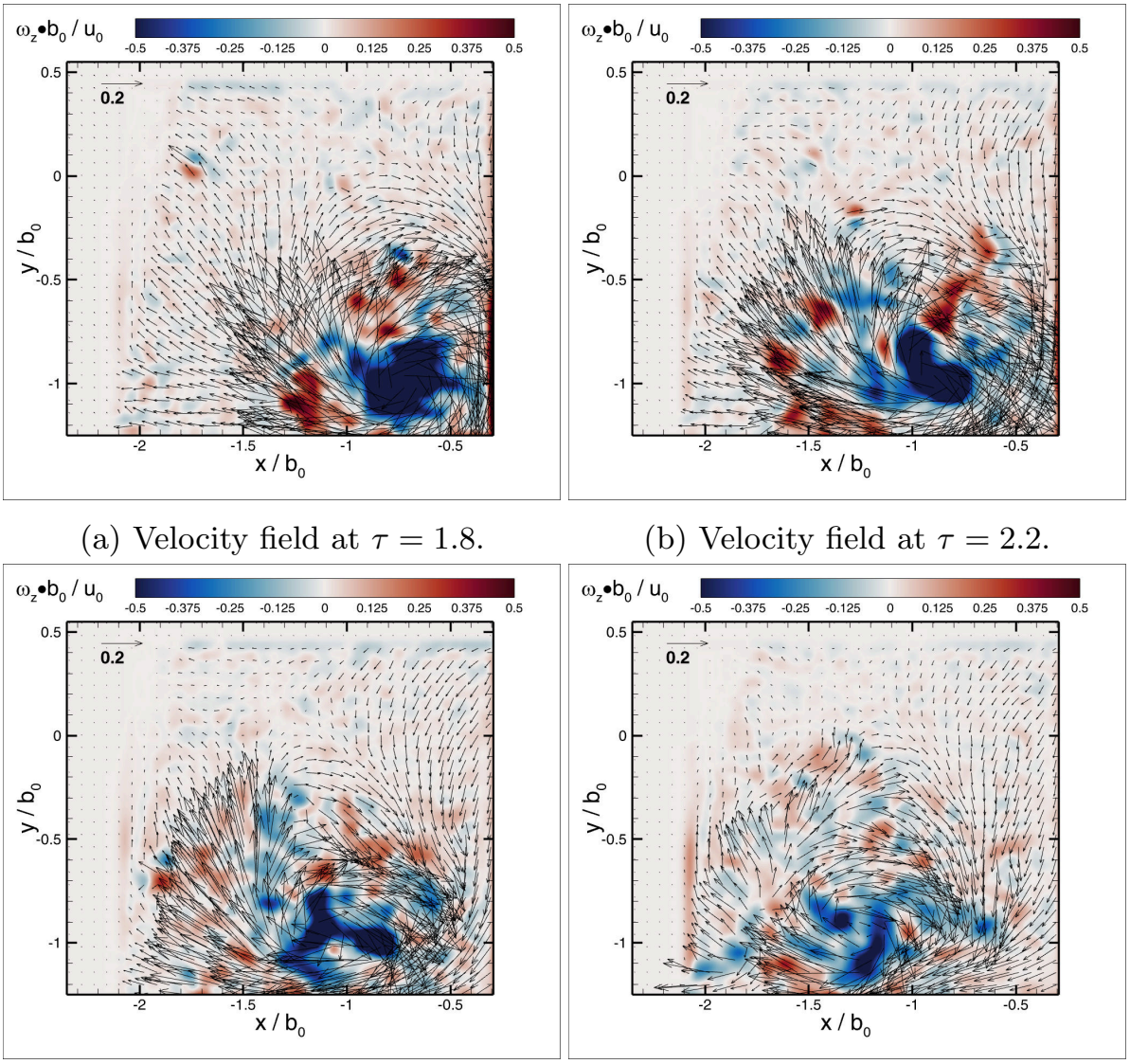

(a) Velocity field at $\tau = 1.8$.

(b) Velocity field at $\tau = 2.2$.

(c) Velocity field at $\tau = 2.7$.

(d) Velocity field at $\tau = 3.1$.

Figure 5.22: High-speed approach $a_{dec} = 2 \cdot a_{ref}$ $FOV_{90°}$ velocity field of wake vortex at $h_{AG} = 1 \cdot c$.

High-speed approach $FOV_{GP,ref}$

Figure 5.23 illustrates the age development of the linked vortex in $FOV_{GP,ref}$. The vortex has multiple linking points, with the two most prominent located at $x/b_0 \approx 0$, $y/b_0 \approx -0.4$ and $x/b_0 \approx -0.6$, $y/b_0 \approx -0.6$, respectively. These linking points cluster together, with each point having a similar vorticity magnitude ($\omega_x \cdot b_0/u_0 \approx -0.5$) as depicted in Figure 5.23b and $\tau = 1.7$. Additionally, a rotating velocity front persists around the linking points. At $\tau = 2.9$, the vortex linking points merge at $x/b_0 \approx -0.9$ and $y/b_0 \approx -0.7$, as shown in Figure 5.23c.

The concentrated vortex generates a velocity field that covers most of the FOV. Finally, only one vortex core maximum remains with a spiral-like deformation in Figure 5.23d. Throughout the vortex's evolution, there is little indication of vortex decay. This low decay suggests that the vortex is stable for longer times.

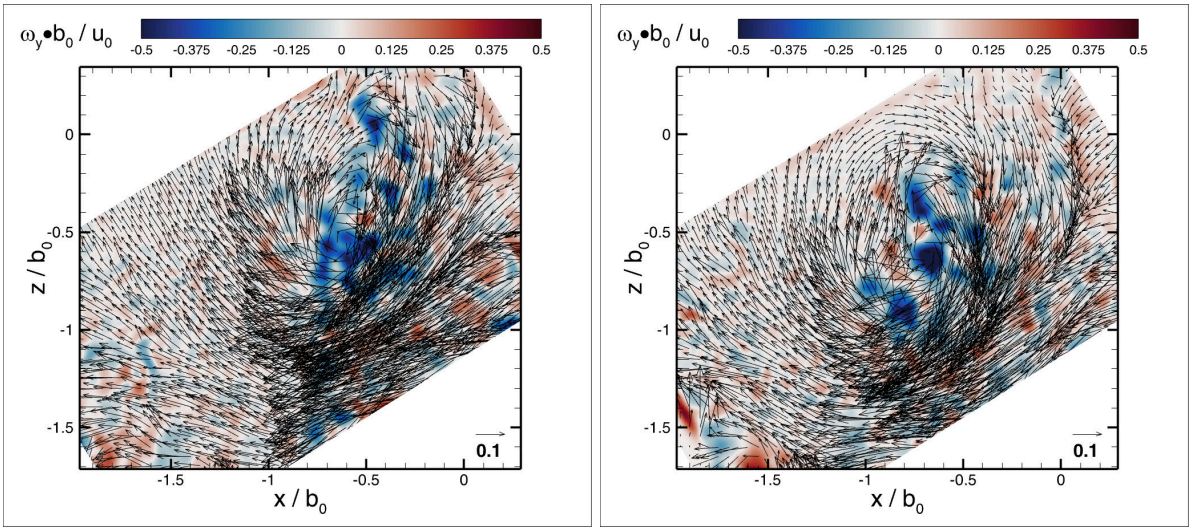

(a) Velocity field at $\tau = 1.1$.

(b) Velocity field at $\tau = 1.7$.

(c) Velocity field at $\tau = 2.9$.

(d) Velocity field at $\tau = 3.6$.

Figure 5.23: High-speed approach $a_{dec} = 2 \cdot a_{ref}$ $FOV_{GP,ref}$ velocity field of wake vortex at $h_{AG} = 1 \cdot c$.

5.4.3 Development of the vortex parameters with deceleration rate variation

In Figure 5.24a, the time development of vortex behavior and the dependence of characteristic parameters on the deceleration rate (vortex center trace and circulation) are presented for the $FOV_{90°}$. Figure 5.24c shows the same for the $FOV_{GP,ref}$. Here a set of two terminal heights above the ground for each of the deceleration rates are presented. The first measurement corresponds to $h_{AG} = 1 \cdot c$ and the second $h_{AG} = 2 \cdot c$. In all cases, the data belonging to the reference deceleration rate is additionally plotted. In Figure 5.24a, the path of the vortex center as it moves through the velocity field $FOV_{90°}$ is shown.

Considering first the low-speed approach case $a_{dec} = 0.5 \cdot a_{ref}$, the vortex remains at a constant height between $x/b_0 \approx 0.8$ and $x/b_0 \approx -1.4$, before exhibiting a significant rebound. This characteristic is common to the two heights above the ground, but the rebound point is shifted to earlier times with higher rebound magnitude in the $h_{AG} = 2 \cdot c$ case. When the terminal deceleration is doubled (high-speed approach), the vortex remains at a constant distance to the ground for a longer period of time at a height of $h_{AG} = 1 \cdot c$. Similarly, the rebound point occurs earlier for a height of $h_{AG} = 2 \cdot c$.

Figure 5.24b displays the vortex circulation and decay as it ages. In the low-speed scenario ($h_{AG} = 1 \cdot c$), the peak circulation occurs at an age of $\tau \approx 1.1$, reaching a value of $\Gamma/\Gamma_0 \approx 0.28$. The lowest coefficient of exponential decay is -0.0343. For the same deceleration at $h_{AG} = 2 \cdot c$, there is a minor delay in age and an increase in peak circulation. The reference deceleration case lies between the low and high-speed approaching cases, with a corresponding change in terminal height above the ground. The magnitude of the exponential coefficient increases to -0.08714. Finally, in the case of twice the deceleration, the trend continues with an even higher exponential decay coefficient of -0.1362 and a peak circulation at the age of $\tau < 1$ for $h_{AG} = 1 \cdot c$. In the FOV parallel to the ground (Figure 5.24c), the ground-linking trail moves along a diagonal that starts near the zero coordinate position. As previously discussed, the vortex links to the ground with low drift rates during a low-speed approach, resulting in the lowest distance covered by the vortex. The reference deceleration case falls between the low and high-speed approaches. At both heights ($h_{AG} = 1 \cdot c$ and $h_{AG} = 2 \cdot c$), it becomes noticeable that the lateral drift outweighs the axial drift. This behavior is more significant in the high-speed case than in the previous ones.

The decay of circulation in the $FOV_{GP,ref}$ (shown in Figure 5.24d) follows a similar trend as observed in the $FOV_{90°}$ case. In the low-speed approach, the exponential decay coefficient starts at -0.0504, then slightly increases in the reference deceleration case, and finally reaches -0.1472 for the high-speed case. However, there is a significant difference in the peak circulation. Despite this, the vortices converge towards the same value at a mature age, indicating that the terminal deceleration primarily impacts early vortex development.

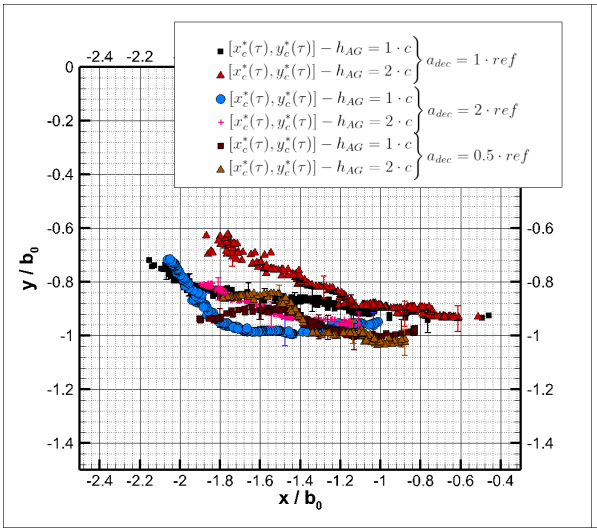

(a) Core trajectory $FOV_{90°}$

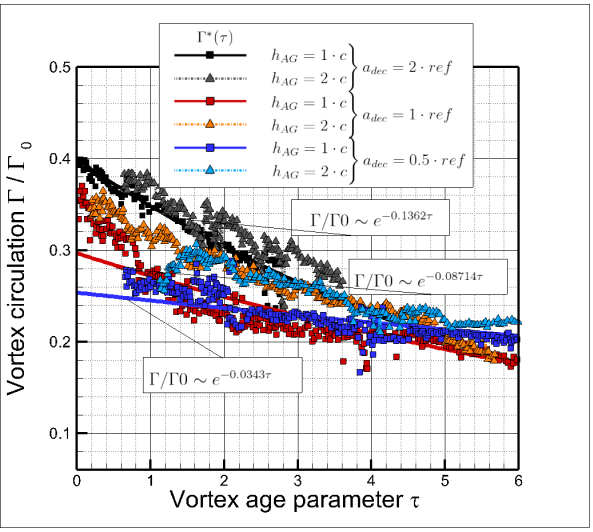

(b) Circulation for the $FOV_{90°}$

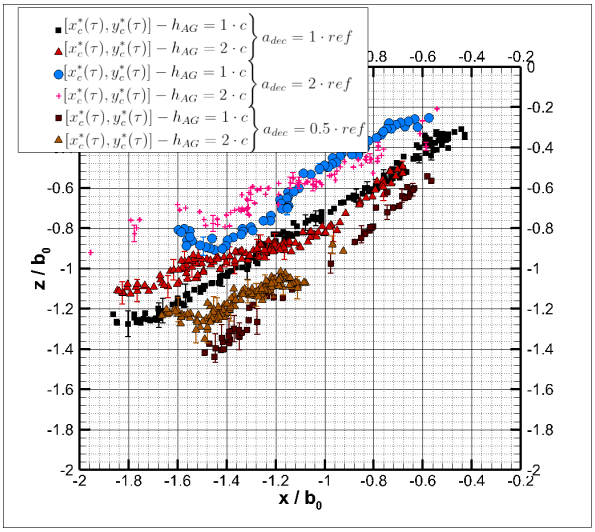

(c) Core trajectory $FOV_{GP,ref}$

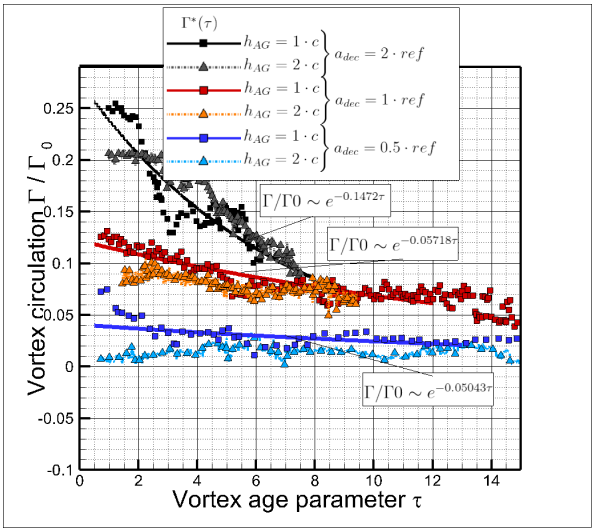

(d) Circulation for the $FOV_{GP,ref}$

Figure 5.24: Vortex core trajectory for the different planes of meassurments $FOV_{90°}$, $FOV_{GP,ref}$ and the corresponding time evolution of circulation. $a_{dec} = 0.5 \cdot a_{ref}$ to $a_{dec} = 2 \cdot a_{ref}$, $h_{AG} = 1 \cdot c$ and $h_{AG} = 2 \cdot c$

6 Conclusions

Studying deceleration without ground interaction is the first step in understanding how vortices behave when an airplane lands in the terminal area. By reducing the towing velocity to zero in horizontal flight, the focus is solely on the wake vortices generated by a decelerating wing. The implications of the deceleration process on the wake vortices are termed end-effects. Even though vortices interacting with the ground display complex phenomena, they also display end-effects. This circumstance is the primary motivation for the first investigation presented n Chapter 4. The focus is on two disturbances due to these end-effects and their impact on the tangential and axial velocities in the wake vortices through 2D and stereo PIV measurements.

The results revealed that the vortex core showcases wake-like axial flow in its initial stages before deceleration. However, as time progresses and the first disturbance occurs, it transitions to jet-like axial flow. The jet-like flow increases in magnitude until the second disturbance arrives, which has a helical-like topology. The first disturbance is attributed to a traveling pressure wave (vortex bursting), which correlates with the instant shortly after the deceleration since it takes some time to develop fully. The second disturbance is shown to occur shortly after the wing comes to rest.

Numerical investigations have identified these disturbances in the case of a single vortex without ground interaction and in the vortices created by a landing aircraft. The presented results show that the disturbances are dependent on velocity and to the Reynolds number and are mostly confined to the vortex-core region, affecting the axial velocity profiles and maxima in tangential velocity. The disturbances do not trigger vortex breakdown or have a severe immediate influence on vortex decay in this free-flight experiment. Nevertheless, these disturbances degrade the vortices and are suggested by other researchers as responsible for the relatively low number of vortex encounters at airports. Particularly in the ground environment, these disturbances behave differently. In addition, the instabilities created by the interaction of these disturbances with omega-shaped-like vortex structures need to be better understood and require further study.

It is crucial to consider the end-effects in future towing tank experiments on wake vortices for free-flight or ground interaction investigations. These effects can lead to unwanted artifacts, which can hinder the accuracy of the results. Therefore, it is advisable to use separation plates or position the start and end of the trajectory at a significant far distance from the measurement region. These countermeasures will help minimize the impact of the end-effects and ensure more precise and reliable data.

In the advanced experimental step, a simplified landing trajectory is reproduced. The experiments were carried out with a towed model capable of dynamically changing the angle of attack while the distance above ground is reduced. The analysis of the measurement data and visual evidence is presented in Chapter 5 of the present work. The 2D-PIV velocity fields provide evidence of ground linking. Whereas the derived vortex core trajectory and circulation the developing of the linked vortices. Several measurement planes are analyzed, and the three-dimensional vortex topology is discussed. Specifically, the height above ground where the wing comes to rest was systematically increased from one chord length to six chord lengths.

In conclusion, the analysis shows the time it takes for the vortices to link to the ground scales as the distance above the ground increases, and the vortices display different characteristics. Mainly showcased by the two cases selected for discussion. In the first case, the wing ends its trajectory at a height above the ground of one chord length and in the second at six times the chord length. In the former, a strong vortex unambiguously links to the ground forming a wedged angle that later assumes an upright position. In the latter, the wing tip vortex links to its counterpart, forming a horseshoe that later dissolves into multiple vortices linking to the ground as it approaches the ground.

In a final series of experiments, both slow- and high-speed approaches were investigated. In the low-speed approach, the vortex forms late, exhibits low circulation values and therefore connects later with the ground. In contrast, in the high-speed approach, the vortex links to the ground almost immediately, showing high circulation values. In addition, the vortex drifts only slightly in the low-speed approach and tends to remain in one position. However, the vortices tend to drift more significantly in the fast approach.

These findings indicate that the behavior of the vortex system dramatically depends on the approach speed and terminal height above ground, with distinctive patterns emerging in each situation. To effectively mitigate potential risks and enhance the operational efficiency of airports, it is imperative to gain a comprehensive understanding of the characteristics of vortices, including their topology patterns, trajectory, strength, and duration. A thorough understanding of these phenomena can be instrumental in designing effective strategies to reduce the spacing between departing and arriving planes while at the same time ensuring the safety of all airport operations.

Nomenclature

Abbreviations

OGE	Out-of-ground effect
NGE	Near-ground effect
IGE	In-ground effect
DNS	Direct numerical simulation
LES	Large eddy simulation
$RANS$	Reynolds-averaged Navier-Stokes
CFD	Computational fluid dynamics
CVM	Computational Vortex Method
LIF	Laser-induced fluorescence
$Lidar$	Light Detection and Ranging
PIV	Particle Image Velocimetry
FOV	Field of view
$FOV_{GP,ref}$	Field of view ground plane reference
$FOV_{GP,shift}$	Field of view ground plane shift
$FOV_{45°}$	Field of view perpendicular to the ground and tilted 45° to the wing's trajectory
$FOV_{90°}$	Field of view perpendicular to the ground and tilted 90° to the wing's trajectory
$2D2C$	2-dimensional, 2-component
$2D3C$	2-dimensional, 3-component
CNC	Computer numerical control

AOA	Angle of attack	
$Nd:YAG$	Neodym-dotierter Yttrium-Aluminium-Granat-Laser	
GHS	Glass hallow spheres	
AB	Air bubbles	
IA	Interrogation area	
M	Sensor pixel spacing over optical magnification	
VGT	Velocity Gradient Tensor	

Symbols

Re_c	Chord based Reynolds number	$[-]$
b	Wingspan	$[m]$
c	Chord length	$[m]$
h_{AG}	Height above ground	$[m]$
α	Angle of attack	$[^\circ]$
α_L	Light sheet tilt angle	$[^\circ]$
γ	Angle of approach	$[^\circ]$
τ	Vortex age parameter	$[-]$
M	Pixel spacing over optical magnification	$[pixel/mm]$
ϵ	Total relative uncertainty	$[-]$
δ	Displacement error	$[pixel]$
Δt	Time between pulses	$[s]$
Γ_{5-15}	Weighted average circulation	$[m^2/s]$
$v_\theta(r)$	Swirl/tangential velocity	$[m/s]$
$v_z(r)$	Axial velocity	$[m/s]$
v_x	Velocity in x-direction	$[m/s]$
v_y	Velocity in y-direction	$[m/s]$

v_z	Velocity in z-direction	$[m/s]$
C_L	Lift coefficient	$[-]$
$\Gamma(r)$	Circulation	$[m^2/s]$
Γ_0	Reference circulation	$[m^2/s]$
v_0	Reference velocity	$[m/s]$
AR	Aspect ratio	$[-]$
r_c	Vortex core	$[m]$
t_0	Vortex time constant	$[s]$
s	Wing load coefficient	$[-]$
s_0	Vortex spacing	$[m]$
N_{frame}	Frame counter	$[-]$
$\Delta z_{[tilt]}$	Offset from the start of deceleration to FOV	$[m]$
N_{frame}	Frame counter	$[-]$
a_{dec}	Deceleration	$[m/s^2]$
a_{ref}	Reference deceleration	$[m/s^2]$
D_{ij}	Velocity Gradient Tensor (VGT)	
S_{ij}	VGT strain rate component	
Ω_{ij}	VGT rotation rate component	
P	First invariant in characteristic equation	
Q	Second invariant in characteristic equation	
R	Third invariant in characteristic equation	
λ_r	Real eigenvalue	
$\lambda_{cr} \pm \lambda_{ci}$	Real and a complex conjugate pair eigenvalue	
λ_r	Real eigenvalue	
Γ_2	Pseudo-circulation	
S	Close circular disc area	

List of Figures

List of Tables

Bibliography

[1] T. Misaka, F. Holzäpfel, and T. Gerz, "Large-eddy simulation of aircraft wake evolution from roll-up until vortex decay," *AIAA journal*, vol. 53, no. 9, pp. 2646–2670, 2015.

[2] S. C. Crow, "Stability theory for a pair of trailing vortices," *AIAA journal*, vol. 8, no. 12, pp. 2172–2179, 1970.

[3] J. N. Hallock and F. Holzäpfel, "A review of recent wake vortex research for increasing airport capacity," *Progress in Aerospace Sciences*, vol. 98, pp. 27–36, 2018.

[4] R. Robins, D. Delisi, and G. Greene, "Development and validation of a wake vortex predictor algorithm," in *36th AIAA Aerospace Sciences Meeting and Exhibit*, p. 665, 1998.

[5] F. Proctor and J. Han, "Numerical study of wake vortex interaction with the ground using the terminal area simulation system," in *37th Aerospace Sciences Meeting and Exhibit*, p. 754, 1999.

[6] H. Lamb, *Hydrodynamics*. Cambridge University Press, 6th edition ed., 1932.

[7] J. Harvey and F. J. Perry, "Flowfield produced by trailing vortices in the vicinity of the ground," *AIAA journal*, vol. 9, no. 8, pp. 1659–1660, 1971.

[8] A. Stephan, *Wake vortices of landing aircraft*. PhD thesis, lmu, 2014.

[9] D. W. Hamilton and F. Proctor, "Wake vortex transport in proximity to the ground," in *19th DASC. 19th Digital Avionics Systems Conference. Proceedings (Cat. No. 00CH37126)*, vol. 1, pp. 3E5–1, IEEE, 2000.

[10] F. Proctor, D. Hamilton, and J. Han, "Wake vortex transport and decay in ground effect-vortex linking with the ground," in *38th aerospace sciences meeting and exhibit*, p. 757, 2000.

[11] F. Holzäpfel and M. Steen, "Aircraft wake-vortex evolution in ground proximity: analysis and parameterization," *AIAA journal*, vol. 45, no. 1, pp. 218–227, 2007.

[12] F. Puel and X. de Saint Victor, "Interaction of wake vortices with the ground," *Aerospace science and technology*, vol. 4, no. 4, pp. 239–247, 2000.

[13] M. Gadelhak, "Use of water towing tanks for aerodynamics and hydrodynamics," *In AGARD*, 1987.

[14] D. L. Ciffone and B. Pedley, "Measured wake-vortex characteristics of aircraft in ground effect," *Journal of Aircraft*, vol. 16, no. 2, pp. 102–109, 1979.

[15] R. Konrath and C. F. v. Carmer, "Towing tank piv measurements on 2-and 4-vortex systems ige," *Projektbericht. FAR-WAKE TR 3.1.2-2. 22 S*, 2008.

[16] C. Cottin, O. Desenfans, G. Daeninck, and G. Winckelmans, "Towing-tank visualizations of two-vortex systems in ground effect," *Munich, Germany, Report No. AST4-CT-2005-012238*, 2005.

[17] Z. Zheng and R. L. Ash, "Study of aircraft wake vortex behavior near the ground," *AIAA journal*, vol. 34, no. 3, pp. 580–589, 1996.

[18] C. Wieselsberger, "Wing resistance near the ground," 1922.

[19] L. Prandtl, "Der induzierte widerstand von mehrdeckern," *Technische Berichte der Flugzeugmeisterei*, vol. 3, no. 7, pp. 309–315, 1918.

[20] S. E. Widnall and T. M. Barrows, "An analytic solution for two- and three-dimensional wings in ground effect," *Journal of Fluid Mechanics*, vol. 41, no. 4, pp. 769–792, 1970.

[21] A. Stephan, F. Holzäpfel, and T. Misaka, "Hybrid simulation of wake-vortex evolution during landing on flat terrain and with plate line," *International Journal of Heat and Fluid Flow*, vol. 49, pp. 18–27, 2014.

[22] N. Kornev, "On unsteady effects in wig craft aerodynamics," *International Journal of Aerospace Engineering*, vol. 2019, pp. 1–14, 2019.

[23] C. Breitsamter, "Wake vortex characteristics of transport aircraft," *Progress in Aerospace Sciences*, vol. 47, no. 2, pp. 89–134, 2011.

[24] R. C. G. Daeninck and G. Winckelmans, "Les calculations of spatially evolving wakes in ground effect," 2006.

[25] D. Vechtel, A. Stephan, and F. Holzäpfel, "Simulation study of severity and mitigation of wake-vortex encounters in ground proximity," *Journal of Aircraft*, vol. 54, no. 5, pp. 1802–1813, 2017.

[26] R. L. Ash and M. R. Khorrami, "Vortex stability," in *Fluid vortices*, pp. 317–372, Springer, 1995.

[27] N. Kornev, V. Treshkov, and G. Reichert, "Dynamics of the trailing vortices near the ground," in *IUTAM Symposium on Dynamics of Slender Vortices: Proceedings of the IUTAM Symposium held in Aachen, Germany, 31 August–3 September 1997*, pp. 425–434, Springer, 1998.

[28] L. Rayleigh, "On the dynamics of revolving fluids," *Proceedings of the Royal Society of London. Series A, Containing Papers of a Mathematical and Physical Character*, vol. 93, no. 648, pp. 148–154, 1917.

[29] L. Rayleigh, "On the stability, or instability, of certain fluid motions," *Proceedings of the London Mathematical Society*, vol. 1, no. 1, pp. 57–72, 1879.

[30] S. Leibovich and K. Stewartson, "A sufficient condition for the instability of columnar vortices," *Journal of Fluid Mechanics*, vol. 126, pp. 335–356, 1983.

[31] G. Batchelor, "Axial flow in trailing line vortices," *Journal of Fluid Mechanics*, vol. 20, no. 4, pp. 645–658, 1964.

[32] M. Lessen, P. J. Singh, and F. Paillet, "The stability of a trailing line vortex. part 1. inviscid theory," *Journal of Fluid Mechanics*, vol. 63, no. 4, pp. 753–763, 1974.

[33] P. I. Singh and M. S. Uberoi, "Experiments on vortex stability," *The Physics of Fluids*, vol. 19, no. 12, pp. 1858–1863, 1976.

[34] H. Moet, F. Laporte, G. Chevalier, and T. Poinsot, "Wave propagation in vortices and vortex bursting," *Physics of Fluids*, vol. 17, no. 5, p. 054109, 2005.

[35] P. Saffman, "Vortex dynamics,(1992)," *Cambrige Monographs on Mechanics and Applied Mathematics Cambridge University Press, reprint*, 1993.

[36] P. R. Spalart, "Airplane trailing vortices," *Annual Review of Fluid Mechanics*, vol. 30, no. 1, pp. 107–138, 1998.

[37] T. Sarpkaya and J. J. Daly, "Effect of ambient turbulence on trailing vortices," *Journal of Aircraft*, vol. 24, no. 6, pp. 399–404, 1987.

[38] L. Nybelen and J. Boussuge, "Temporal dns on vortex bursting and assessment," *FAR-Wake Technical Report*, vol. 1, pp. 2–2, 2008.

[39] T. Lonfils, R. Cocle, G. Daeninck, C. Cottin, and G. Winckelmans, "Numerical investigations of end-effects associated with accelerated/decelerated wings: time-developing and space-developing simulations," *FAR-Wake Technical Report*, vol. 1, no. 2, 2007.

[40] N. Kornev and N. Abbas, "Numerical simulation of the tip vortex behind a wing oscillated with a small amplitude," *Journal of Aircraft*, vol. 54, no. 2, pp. 831–837, 2017.

[41] D. Birch and T. Lee, "Tip vortex behind a wing oscillated with small amplitude," *Journal of aircraft*, vol. 42, no. 5, pp. 1200–1208, 2005.

[42] D.-F. Feder, M. Dhone, N. Kornev, and M. Abdel-Maksoud, "Comparison of different approaches tracking a wing-tip vortex," *Ocean engineering*, vol. 147, pp. 659–675, 2018.

[43] W. J. Devenport, M. C. Rife, S. I. Liapis, and G. J. Follin, "The structure and development of a wing-tip vortex," *Journal of fluid mechanics*, vol. 312, pp. 67–106, 1996.

[44] G. Castaneda Fuentes, F. Hüttmann, and S. Grundmann, "Development of axial flows in wake vortices due to end effects," *AIAA Journal*, vol. 60, no. 4, pp. 2223–2240, 2022.

[45] H. J. Lugt, *Introduction to vortex theory*. Vortex Flow Press, 1996.

[46] A. Stephan, F. Holzäpfel, and S. Zholtovski, "The effect of gusts on aircraft wake vortices," *Aircraft Engineering and Aerospace Technology*, vol. 89, no. 5, pp. 692–702, 2017.

[47] M. S. Selig, J. F. Donovan, and D. B. Fraser, "Airfoils at low speeds," 1989.

[48] C. F. CARMER and R. KONRATH, "Influence of reynolds number on generation and decay of aircraft wakes: Experimental investigation using generic models," *F13 and F13X. DLR Göttingen, Germany*, 2006.

[49] A. Stephan, F. Holzäpfel, T. Misaka, R. Geisler, and R. Konrath, "Enhancement of aircraft wake vortex decay in ground proximity," *CEAS Aeronautical Journal*, vol. 5, no. 2, pp. 109–125, 2014.

[50] R. Konrath, K.-P. Mach, P. Anschau, *et al.*, "Validation experiment with 4-vortex wake in large tow tank," 2008.

[51] J. Tschepe, C. N. Nayeri, and C. O. Paschereit, "Analysis of moving model experiments in a towing tank for aerodynamic drag measurement of high-speed trains," *Experiments in Fluids*, vol. 60, no. 6, pp. 1–16, 2019.

[52] F. Bao, H. Vollmers, and H. Mattner, "Experimental study on controlling wake vortex in water towing tank," in *20th International Congress on Instrumentation in Aerospace Simulation Facilities, 2003. ICIASF'03.*, pp. 214–223, IEEE, 2003.

[53] R. Koenig and E. Schubert, "On the influences of an increased ils glide slope on noise impact, fuel consumption and landing approach operation," in *Proceedings AIAC14 Fourteenth Australian International Aerospace Congress*, Citeseer, 2011.

[54] S. Scharnowski and C. J. Kähler, "Particle image velocimetry-classical operating rules from today's perspective," *Optics and Lasers in Engineering*, p. 106185, 2020.

[55] J. Westerweel and F. Scarano, "Universal outlier detection for piv data," *Experiments in fluids*, vol. 39, no. 6, pp. 1096–1100, 2005.

[56] F. Scarano, C. van Wijk, and L. Veldhuis, "Traversing field of view and ar-piv for mid-field wake vortex investigation in a towing tank," *Experiments in Fluids*, vol. 33, no. 6, pp. 950–961, 2002.

[57] M. Raffel, C. E. Willert, F. Scarano, C. J. Kähler, S. T. Wereley, and J. Kompenhans, *Particle image velocimetry: a practical guide*. Springer, 2018.

[58] J. J. Charonko and P. P. Vlachos, "Estimation of uncertainty bounds for individual particle image velocimetry measurements from cross-correlation peak ratio," *Measurement Science and Technology*, vol. 24, no. 6, p. 065301, 2013.

[59] B. Wieneke, "Piv uncertainty quantification from correlation statistics," *Measurement Science and Technology*, vol. 26, no. 7, p. 074002, 2015.

[60] G. Lindner, Y. Devaux, and S. Miskovic, "Vortexfitting a post-processing fluid mechanics tool for vortex identification," *SoftwareX*, vol. 12, p. 100604, 2020.

[61] A. S. Aseyev and R. B. Cal, "Vortex identification in the wake of a model wind turbine array," *Journal of Turbulence*, vol. 17, no. 4, pp. 357–378, 2016.

[62] J. C. Hunt, A. A. Wray, and P. Moin, "Eddies, streams, and convergence zones in turbulent flows," *Studying turbulence using numerical simulation databases, 2. Proceedings of the 1988 summer program*, 1988.

[63] M. S. Chong, A. E. Perry, and B. J. Cantwell, "A general classification of three-dimensional flow fields," *Physics of Fluids A: Fluid Dynamics*, vol. 2, no. 5, pp. 765–777, 1990.

[64] J. Zhou, R. J. Adrian, S. Balachandar, and T. Kendall, "Mechanisms for generating coherent packets of hairpin vortices in channel flow," *Journal of fluid mechanics*, vol. 387, pp. 353–396, 1999.

[65] B. Epps, "Review of vortex identification methods," in *55th AIAA aerospace sciences meeting*, p. 0989, 2017.

[66] L. Graftieaux, M. Michard, and N. Grosjean, "Combining piv, pod and vortex identification algorithms for the study of unsteady turbulent swirling flows," *Measurement Science and technology*, vol. 12, no. 9, p. 1422, 2001.

[67] S. Endrikat, "Find vortices in velocity fields," 2021. `https://www.mathworks.com/matlabcentral/fileexchange/52343-find-vortices-in-velocity-fields`, MATLAB Central File Exchange. Retrieved May 12, 2021.

[68] F. Moisy, "Pivmat 4.20," 2021. `https://www.mathworks.com/matlabcentral/fileexchange/10902-pivmat-4-20`, MATLAB Central File Exchange. Retrieved May 12, 2021.

[69] A. de Bruin, "Framework definition, wake characterisation and synthesis planning for the far-wake project," *FAR-Wake, Deliverable D*, vol. 4, p. 1, 2005.

[70] T. Gerz, F. Holzäpfel, and D. Darracq, "Commercial aircraft wake vortices," *Progress in Aerospace Sciences*, vol. 38, no. 3, pp. 181–208, 2002.

[71] M. Drela, "Xfoil: An analysis and design system for low reynolds number airfoils," in *Low Reynolds Number Aerodynamics: Proceedings of the Conference Notre Dame, Indiana, USA, 5–7 June 1989*, pp. 1–12, Springer, 1989.

[72] N. Chigier and V. Corsiglia, "Tip vortices: velocity distributions," 1971.

[73] J. Hallock, D. Burnham, J. Hallock, and D. Burnham, "Decay characteristics of wake vortices from jet transport aircraft," in *35th Aerospace Sciences Meeting and Exhibit*, p. 60, 1997.

[74] D. Birch, T. Lee, F. Mokhtarian, and F. Kafyeke, "Structure and induced drag of a tip vortex," *Journal of Aircraft*, vol. 41, no. 5, pp. 1138–1145, 2004.

[75] M. Giuni and R. B. Green, "Vortex formation on squared and rounded tip," *Aerospace science and technology*, vol. 29, no. 1, pp. 191–199, 2013.

[76] D. J. Garmann and M. R. Visbal, "Analysis of tip vortex near-wake evolution for stationary and oscillating wings," *AIAA Journal*, vol. 55, no. 8, pp. 2686–2702, 2017.

[77] T. Lee and J. Pereira, "Nature of wakelike and jetlike axial tip vortex flows," *Journal of Aircraft*, vol. 47, no. 6, pp. 1946–1954, 2010.

[78] T. Misaka, F. Holzäpfel, I. Hennemann, T. Gerz, M. Manhart, and F. Schwertfirm, "Vortex bursting and tracer transport of a counter-rotating vortex pair," *Physics of Fluids*, vol. 24, no. 2, p. 025104, 2012.

[79] F. Bao and H. Vollmers, "Alleviation of end-effect in facilities for far wake investigations," in *43rd AIAA Aerospace Sciences Meeting and Exhibit*, p. 907, 2005.

[80] D. Fabre, D. Sipp, and L. Jacquin, "Kelvin waves and the singular modes of the lamb–oseen vortex," *Journal of Fluid Mechanics*, vol. 551, pp. 235–274, 2006.

[81] F. De Gregorio and A. Ragni, "Wake vortex characterization in towing tank facilities using piv technique," in *41st Aerospace Sciences Meeting and Exhibit*, p. 93, 2003.

[82] Y. Aboelkassem, "Trailing vortex filament: A novel similarity analysis," *Journal of aircraft*, vol. 44, no. 2, pp. 683–687, 2007.

[83] M. J. Bhagwat and J. G. Leishman, "Generalized viscous vortex model for application to free-vortex wake and aeroacoustic calculations," in *Annual forum proceedings-American helicopter society*, vol. 58, pp. 2042–2057, American Helicopter Society, Inc, 2002.

[84] J. Schröttle, A. Dörnbrack, and U. Schumann, "Excitation of vortex meandering in shear flow," *Fluid Dynamics Research*, vol. 47, no. 3, p. 035508, 2015.

[85] S. Unterstrasser and A. Stephan, "Far field wake vortex evolution of two aircraft formation flight and implications on young contrails," *The Aeronautical Journal*, vol. 124, no. 1275, pp. 667–702, 2020.

[86] F. Holzäpfel, T. Gerz, and R. Baumann, "The turbulent decay of trailing vortex pairs in stably stratified environments," *Aerospace Science and Technology*, vol. 5, no. 2, pp. 95–108, 2001.

[87] F. Schlegel, D. Wee, Y. M. Marzouk, and A. F. Ghoniem, "Contributions of the wall boundary layer to the formation of the counter-rotating vortex pair in transverse jets," *Journal of fluid mechanics*, vol. 676, pp. 461–490, 2011.

[88] P. Meunier, S. Le Dizes, and T. Leweke, "Physics of vortex merging," *Comptes Rendus Physique*, vol. 6, no. 4-5, pp. 431–450, 2005.

[89] J.-D. Zhang, Q.-H. Zuo, M.-D. Lin, W.-X. Huang, W.-J. Pan, and G.-X. Cui, "Evolution of vortices in the wake of an arj21 airplane: Application of the lift-drag model," *Theoretical and Applied Mechanics Letters*, vol. 10, no. 6, pp. 419–428, 2020.

[90] L. Jacquin, D. Fabre, P. Geffroy, and E. Coustols, "The properties of a transport aircraft wake in the extended near field-an experimental study," in *39th Aerospace Sciences Meeting and Exhibit*, p. 1038, 2001.

[91] Q. Chen, T. Hu, P. Liu, Y. Liu, Q. Qu, H. Guo, and R. A. Akkermans, "Experiments on asymmetric vortex pair interaction with the ground," *Experiments in Fluids*, vol. 61, pp. 1–22, 2020.

[92] H. Liang and T. Maxworthy, "An experimental investigation of swirling jets," *Journal of fluid mechanics*, vol. 525, pp. 115–159, 2005.

[93] T. Leweke, "Far-wake: Fundamental research on aircraft wake phenomena," in *1st WakeNet3-Europe Workshop on" Wake Turbulence Safety in Future Aircraft Operations"*, 2009.

[94] F. Holzäpfel, T. Hofbauer, D. Darracq, H. Moet, F. Garnier, and C. F. Gago, "Analysis of wake vortex decay mechanisms in the atmosphere," *Aerospace Science and Technology*, vol. 7, no. 4, pp. 263–275, 2003.

[95] A. Stephan, D. Rohlmann, F. Holzäpfel, and R. Rudnik, "Effects of detailed aircraft geometry on wake vortex dynamics during landing," *Journal of Aircraft*, vol. 56, no. 3, pp. 974–989, 2019.

[96] T. Sarpkaya, "Effect of core size on the rise and demise of trailing vortices," tech. rep., NAVAL POSTGRADUATE SCHOOL MONTEREY CA, 1982.

[97] C. H. Williamson, T. Leweke, D. J. Asselin, and D. M. Harris, "Phenomena, dynamics and instabilities of vortex pairs," *Fluid dynamics research*, vol. 46, no. 6, p. 061425, 2014.

[98] C. Schwarz, A. Bodling, C. C. Wolf, R. Brinkema, M. Potsdam, and A. D. Gardner, "Development of secondary vortex structures in rotor wakes," *Experiments in Fluids*, vol. 63, pp. 1–21, 2022.

[99] S. Terrington, K. Hourigan, and M. Thompson, "Vortex ring connection to a free surface," *Journal of Fluid Mechanics*, vol. 944, p. A56, 2022.

[100] A. Stephan, F. Holzäpfel, and T. Misaka, "Aircraft wake-vortex decay in ground proximity—physical mechanisms and artificial enhancement," *Journal of Aircraft*, vol. 50, no. 4, pp. 1250–1260, 2013.

[101] F. Holzäpfel, T. Gerz, F. Köpp, E. Stumpf, M. Harris, R. I. Young, and A. Dolfi-Bouteyre, "Strategies for circulation evaluation of aircraft wake vortices measured by lidar," *Journal of Atmospheric and Oceanic Technology*, vol. 20, no. 8, pp. 1183–1195, 2003.

[102] T. Sarpkaya, "Decay of wake vortices of large aircraft," *AIAA journal*, vol. 36, no. 9, pp. 1671–1679, 1998.

Acknowledgements

I am deeply grateful to Prof. Grundmann for his valuable support and guidance throughout my term at the institute. His constant encouragement and insightful perspectives have been instrumental in refining my abilities as a researcher and engineer, which has undoubtedly contributed to the results presented in this work. Additionally, I thank Prof. Kornev for his thorough examination of my thesis. I also thank Dr. Brede for his invaluable assistance in conducting my experiments and for his thorough review of my work. Lastly, I would like to sincerely thank my colleagues for their encouragement and support throughout my experiments. Their positive energy and comradery made the experience all the more enjoyable and have undoubtedly contributed to the success of my research.